# INVESTIGATION OF THERMAL EMISSION FROM LOWER ATMOSPHERE OF MARS

**A THESIS**

**Submitted for the Award of Ph.D. Degree of**

**PACIFIC ACADEMY OF HIGHER EDUCATION AND RESEARCH UNIVERSITY**


By

**JETHWA MASOOM PANKAJ**

Under the Supervision of

**Prof. S. A. HAIDER** **Dr. ABHISHEK SAXENA**

**DEPARTMENT OF PHYSICS**
**FACULTY OF SCIENCE**

**PACIFIC ACADEMY OF HIGHER EDUCATION AND RESEARCH UNIVERSITY**
**UDAIPUR**

*Dedicated to*
*my Family*

# DEPARTMENT OF PHYSICS

## PAHER UNIVERSITY, UDAIPUR

**Prof. S. A. HAIDER**

# CERTIFICATE

It gives me immense pleasure in certifying that the thesis entitled **"INVESTIGATION OF THERMAL EMISSION FROM LOWER ATMOSPHERE OF MARS"** submitted by **JETHWA MASOOM PANKAJ** is based on the research work carried out under my guidance. He has completed the following requirements as per Ph.D. regulations of the University.

(i) Course work as per University rules.

(ii) Residential requirements of the University.

(iii) Regularly submitted Half Yearly Progress Report.

(iv) Published/accepted minimum of two research paper in a refereed research journal.

I recommend the submission of thesis.

Date:

**(Prof. S. A. HAIDER)**

Ph.D Supervisor
Faculty of Science,
PAHER University
Udaipur

Senior Professor
Physical Research Laboratory
Ahmedabad

# DEPARTMENT OF PHYSICS

## PAHER UNIVERSITY, UDAIPUR

**DR. ABHISHEK SAXENA**

# CERTIFICATE

It gives me immense pleasure in certifying that the thesis entitled **"INVESTIGATION OF THERMAL EMISSION FROM LOWER ATMOSPHERE OF MARS"** submitted by **JETHWA MASOOM PANKAJ** is based on the research work carried out under my guidance. He has completed the following requirements as per Ph.D. regulations of the University.

(v) Course work as per University rules.

(vi) Residential requirements of the University.

(vii) Regularly submitted Half Yearly Progress Report.

(viii) Published/accepted minimum of two research paper in a refereed research journal.

I recommend the submission of thesis.

Date:

**(Dr. Abhishek Saxena)**

Ph.D Co-Supervisor
Faculty of Science,
PAHER University
Udaipur

# DECLARATION

I, **JETHWA MASOOM PANKAJ** S/o **Late Shri PANKAJ JETHWA** resident of Ahmedabad, Gujarat (India) hereby declare that the research work incorporated in the present thesis entitled **"INVESTIGATION OF THERMAL EMISSION FROM LOWER ATMOSPHERE OF MARS"** is my own work and is original. This work (in part or in full) has not been submitted to any University for the award of a Degree or a Diploma. I have properly acknowledged the material collected from secondary sources, wherever required. I solely own the responsibility for the originality of the entire content.

Date:

Place: Udaipur

**(JETHWA MASOOM PANKAJ)**

Research Scholar

# COPYRIGHT

# ACKNOWLEDGEMENTS

I would like to thank my family for their tremendous patience. I have been fortunate to be surrounded by extraordinary people who have been there in every walk of my life. I am grateful to all of them. I wish to express my gratitude and respect to my supervisor, **Prof. S. A. HAIDER** for his guidance, continuous encouragement and support all through the pursuance of the research work. He has spent voluminous amount of time with me and helped me in understanding the research issues and improving my presentation skills. I express my sincere gratitude to my co-supervisor **Dr. ABHISHEK SAXENA**, for fruitful discussions, constant encouragement and constructive suggestions throughout the pursuance of the research work. I take this opportunity to express my gratitude and respect to **Prof. VARUN SHEEL**, chairman, Planetary Sciences Division, for his constant support. I would also like to thank **Prof. ANIL BHARADWAJ**, Director, Physical Research Laboratory (PRL), and **Prof. P. JANARDHAN**, Dean, PRL, to allow me to avail the facilities of PRL to complete my thesis work. I further place on record my admiration to all scientific faculty members and technical staff of planetary sciences division for their valuable discussions and support. I acknowledge the support of all the faculty members, staff, and Dean, PAHER university for their support during my research work. I acknowledge help of Mr. Jigar Raval, Mr. Hitendra Mishra and Computer Center staff for their prompt help in computational and HPC facilities required during my research work. I am also thankful to library staff for their continuous support. The inspiration, support and cooperation that I have received from my friends and seniors are beyond the scope of any acknowledgement. Yet, I would express my heartfelt gratitude to them. I must accolade the company of Dr. Pothuraju Thirupathaiah, Dr. Disha Sawant, Dr. Tikemani

Baug, Dr. Deepak Singh, Dr. Sharad Sheth, Dr. Bhavin Pandya, Dr. Ashimanand Modak, Shefali, and Siddhi for providing me with various tools, which made my research work simple and effective. Their constructive criticism and critical inputs at various stages of my research helped me improved significantly. I also express my thanks to all research scholars in the planetary sciences division for their support and encouragement.

I am lifelong grateful to my beloved parents, Smt. Nalini Jethwa and Late Shri Pankaj Jethwa, who worked hard to educate me. Their work inspired me to do the best in my studies. I thank the Almighty God for given me such a wonderful and lovable parent. I thank my sister, Virali and brother-in-law, Sagar Rathi and their family, for their constant affection and encouragement. I am deeply touched by their support even though they missed my presence a lot. I gratefully acknowledge the support of J.C. Bose grant to carry out my thesis work.

**(JETHWA MASOOM PANKAJ)**

# PREFACE

The present thesis is an attempt to study lower atmosphere by means of thermal emission data and modelling of the physical processes governed by the interaction of solar radiation and particles. Absorption of solar radiation by any planet results in excitation, dissociation, ionization, and heating of the atmosphere constituents. A schematic diagram presenting various solar radiation reaching Mars is drawn. In recent times, with the advent of space-based measurements, there has been various attempt to unravel the mysteries of planetary bodies such as Mars. The interpretation of observation provides an insight about underlying physical process. During dust storm, dust from the surface lifts, engulfs whole atmosphere, and significantly affect the circulation. We attempt to address this issue by studying the vertical profiles of dust during Martian Year (MY) 28, when a global dust storm occurred on Mars. The dust density profiles of different size of aerosol particles and their influences in the lower atmosphere of Mars are carried out. We used the dust optical depth data derived from the thermal emission measurements and semi-empirical formulation. We suggest that the dust particle of the smallest radius lifts up to higher altitude compared to the larger radius. We have considered three distinct dust cases viz., low, medium and high, during dusty season at Mars during MY 28. The comparison with dust profiles from other instruments are also shown. Further, we have processed the Planetary Fourier Spectrometer (PFS) dataset to study and investigate the dust storm of MY 28. We have found the presence of dust in the PFS measured spectra. With the help of thermal emissions data measured by PFS, we have found that the MY 28 dust storm affected the PFS measured spectra ~ 30° S latitudes. Further, Spectroscopy for the Investigation of the Characteristics of the Atmosphere of Mars (SPICAM) helped us understanding the ozone variability in Martian atmosphere and enhanced our understanding significantly over 10 years. We have compared the SPICAM observations and Mars Climate Database (MCD) derived ozone abundances, and studied the heating of atmosphere due to ozone. This study have helped us understand the effect of dust storms on ozone and its heating rates, its seasonal variations, and altitude dependence. Our study suggests that ozone heating rate affects the Martian lower atmosphere significantly (altitude $< 10$ km). Model vertical profiles of heating rates shows co-relation with seasonal variability of ozone abundance. The Martian atmosphere also interacts with the energetic particles precipitating in the atmosphere during a solar event. When such energetic particles enter into Mars atmosphere, they collide with atmospheric gases and deposit their energy into the lower atmosphere. This leads to excitation, ionization and emission in the lower atmosphere. The SPICAM has also observed ultraviolet emissions of $N_2$, CO Cameron band, and $CO_2^+$ ultraviolet doublet emissions on Mars. We have analyzed the Imaging Ultraviolet Spectrograph (IUVS) instrument on board Mars Atmosphere and Volatile Evolution (MAVEN) to study Martain aurora. Unlike Earth, Mars has no magnetic field and possess $CO_2$ predominantly in its atmosphere. Thus, interaction with solar energetic particles are different. The energetic electron during the SEP event and $H^+$-H are considered as a source for producing diffuse aurora on Mars. We have studied the auroral intensities using a Monte Carlo based Analytical Yield Spectrum (AYS) method and hybrid model. One of major sources of $CO_2^+$ Ultraviolet Doublet (UVD) emissions at the nightside is precipitating electrons and $H^+$-H. In the present work, we have used Monte Carlo technique has been utilised to calculate the production rates. We have also calculated the limb intensities and compared with the MAVEN observations. The effect of various model input parameters are discussed in detail.

A brief introduction and motivation of the work carried out in this thesis is presented in Chapter 1. The mathematics used for calculating dust density; ozone heating rates, radiative transfer, and auroral emissions is discussed in Chapter 2. In Chapter 3, the seasonal variability of dust, dust vertical profiles and its implications during the dust storm of MY 28 is discussed. Chapter 4 describes the analysis of the dust activity during the dust storm of MY 28 from PFS observations. In Chapters 5, results from the general circulation model and variability of ozone heating rates in the atmospheres of Mars are discussed. In chapter 6, we present the results of modelling of diffuse aurora on Mars for December 2014 Solar Energetic Particle (SEP) event. The solar energetic particle and $H^+$-H have considered as source to compare with available MAVEN observations. In the seventh chapter, we summarize the present work and present the future work in chapter 8.

❑❑❑

# Contents

# List of Figures

# CHAPTER - 1

# INTRODUCTION

# CONTENTS

*This chapter describes in brief electromagnetic and particle radiations incoming from the Sun and their contributions to the lower atmosphere of Mars. The outgoing radians from Mars in terms near infrared (0.7-5 μm), mid infrared (5-50 μm) and far infrared (50-100 μm) radiations are also described. We have also reported compositions of Mars' lower atmosphere viz. $CO_2$, $N_2$, Ar, $O_2$, CO, $H_2$, $H_2O$, O, $O_3$, NO, $NO_2$, and $HNO_3$ and their variations with season, latitude and longitude. The global dust storm is also discussed on Mars. Each chapter of the present thesis are described in brief in section 1.2.2.*

# 1.1 INTRODUCTION

In our solar system the Sun is the primary source of energy, which changes the atmosphere and ionosphere of Mars. The Sun emits electromagnetic and particle radiations. The electromagnetic radiation consists of different wavelengths viz., gamma rays ($\lambda < 10^{-4}$ μm), X-rays ($10^{-4}$ μm $< \lambda < 10^{-2}$ μm), ultraviolet ($10^{-2}$ μm $< \lambda <$ 0.4 μm), Visible (0.4 μm $< \lambda <$ 0.7 μm), infrared (0.7 μm $< \lambda < 10^2$ μm), microwave ($10^2$ μm $< \lambda < 10^3$ μm), and radio waves ($\lambda > 10^4$ μm) (Hartman, 1989; Lissauer and Pater, 2013). The particle radiations contain 95% protons, 2 ~ 3% electrons and heavily charged ions. The figure 1.1 shows a schematic diagram of incoming and outgoing solar radiation from the Mars. The Electromagnetic Radiation (EM), solar wind, Coronal Mass Ejection (CME) and Solar Energetic Particle (SEP) are considered as the incoming radiation, which interacts with the atmospheric gases of Mars. These interactions are controlled by the wavelength and flux of the radiation. The small black dots represent the Martian atmosphere in figure 1.1. The important sources of ionizations of atmospheric gases are EUV, X-rays, Galactic Cosmic Rays (GCR), X-ray flares and SEP. The photoionization and photoelectrons are produced due to impact of solar EUV and X-ray radiations with the atmosphere of Mars (Haider et al., 2011; Haider and Mahajan, 2014). The GCR and SEP penetrate deep into the lower atmosphere and produced D region ionosphere and auroral emissions respectively (Haider et al., 2009; Haider and Masoom, 2019). The X-ray flares and SEP are emitting from the sun during the disturbed condition. The solar X-ray flares are measured by Geostationary Operational Environmental Satellite (GOES) (Bornmann et al., 1996). The SEP spectra is observed by Mars Atmosphere and Volatile Evolution (MAVEN) between energy range from 25 keV to 200 keV (https://pds-ppi.igpp.ucla.edu).

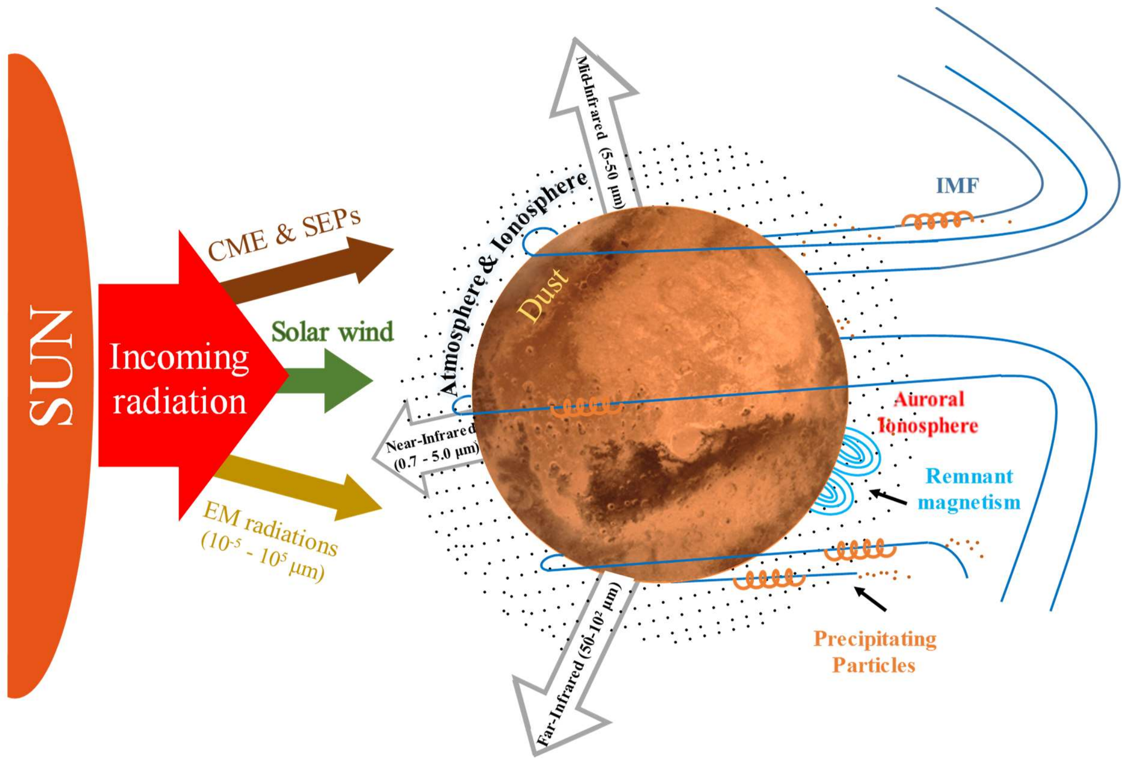


**Figure 1.1 Schematic representations of incoming radiations from the sun and outgoing radiations from the Mars. The Electromagnetic (EM) and particle radiations (solar wind, CME and SEP) are emitting from the sun and contributing to the atmosphere/ionosphere of Mars. The near, mid and far infrared radiations are outgoing from the Mars. The Mars is covered by the dust as observed by Mangalyaan.**

### 1.1.1 Thermal emission

In figure 1.1 the image of Mars is taken from Mars Colour Camera (MCC) onboard Indian Mars Orbiter Mission (Mangalyaan) (Arya et al., 2015). This image clearly represents that a global dust storm occurred on Mars and covered the entire planet. The dust storm occurs after 3-4 Mars years at low latitudes of southern hemisphere while regional dust storms occur every year during the summer (Sheel and Haider, 2016). During dust storm period atmospheric optical depths were enhanced from 2 to 5) (Guzewich et al., 2018; Haider et al., 2019). The thermal structure is determined by the balance of radiative heating by the sun and cooling by thermal infrared radiation to space from the atmosphere and surface. The atmosphere of Mars plays an important role as it interacts with radiation in visible, infrared and ultraviolet radiation coming from the sun and the thermal radiation (mid and far infrared) emitted by the surface and the atmosphere. The Martian atmosphere allows complete visible radiation and some fraction of ultraviolet radiation to reach on the surface, while carbon dioxide absorbs small fraction in near-infrared at 1 μm and 2 μm. However, $CO_2$ has a strong vibration-rotation band at ~ 2.7 μm, 4.3 μm, and 15 μm. The $H_2O$ present in Martian atmosphere exhibits rotational bands between 6.3 μm and 20-40 μm in the thermal infrared radiation (Haus and Titov, 2002). Read et al. (2015) suggested that the Martian atmosphere absorbs around 70-85% of the thermal radiation emitted from the surface. The remaining fraction of radiation (15-30%) is sent out to space and is shown by grey arrows in figure 1.1. This outgoing emission is measured by Planetary Fourier Spectrometer (PFS) onboard Mars Express (MEX) (Formisano et al., 2004). The PFS observed thermal emission spectra in the mid infrared wavelength band (5 - 50 μm) and near infrared wavelength band (1.5-5 μm).

## 1.1.2 Atmosphere of Mars

The upper atmosphere of Mars exists above 100 km. The first measurement of neutral species was made by neutral mass spectrometer onboard Viking Landers 1 and 2 in the upper atmosphere (Nier and McElroy, 1977). They obtained mass spectra from 1 to 49 amu. Later an accelerometer and radio occultation experiment onboard Mars Global Surveyor (MGS) provided a large datasets of atmospheric density at various locations in the upper and lower atmosphere of Mars respectively. These observations confirmed that the atmosphere of Mars contains $CO_2$, $N_2$, Ar, CO, $O_2$, and NO with contribution to the total air density of about 95.5%, 2.7%, 1.5%, 0.4-1.4%, 0.17%, 0.008% respectively. The Viking Landers also carried a Retarding Potential Analyzer (RPA) (Hanson et al., 1977), which provided information on the major ion densities and plasma temperatures in the ionosphere up to an altitude of about 300 km. The atmospheric pressure and temperature of Mars on the surface is around 6 mbar and 200 K. The atmosphere of Mars is quite dusty. Data from Mars Exploration Rovers indicated that suspended dust particles within the atmosphere are roughly 1.5 μm (Lemmon et al., 2015).

Recently MAVEN observed neutral density profiles from Neutral Gas Ion Mass Spectrometer (NGMIS) during the daytime and nighttime atmosphere of Mars above 150 km (Mahaffy et al., 2015). In figure 1.2 we have plotted sample profiles of neutral model atmosphere of $CO_2$, Ar, $N_2$, CO, O, and He observed by MAVEN on 10, 14, and 17 September, 2017, when the spacecraft was crossing from inbound to outbound orbits. The inbound and outbound orbits were crossings from the daytime and nighttime atmosphere of Mars respectively.

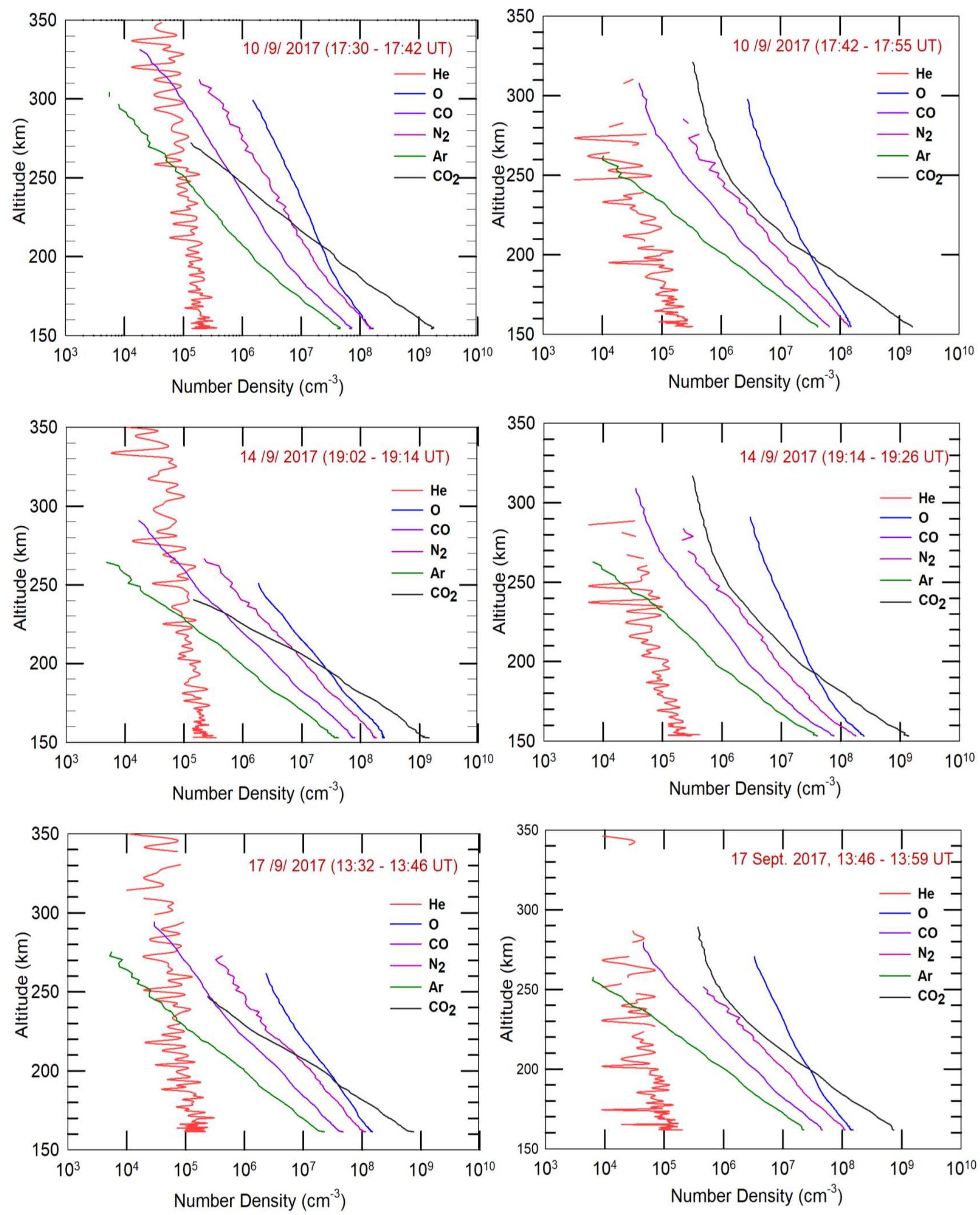


**Figure 1.2: MAVEN observations of neutral densities in the upper atmosphere of Mars corresponding to inbound and outbound orbits on 10, 14, and 17 September, 2017.**

The lower atmosphere of Mars exists below 100 km where gases are mixed and eddy diffusion is dominant. The lower atmosphere of Mars is characterized by strong coupling between pressure, temperature, neutral density and winds. MGS and MEX have observed temperature, pressure, and total density in the lower atmosphere of Mars with radio occultation experiment (Bougher et al., 2001; Hinson et al., 1999; Pätzold et al., 2005). The photochemical models have predicted concentrations of $O_2$, $O_3$, $CO_2$, CO and other neutral species in the lower atmosphere of Mars (Belton and Hunten, 1966; Parkinson and Hunten, 1972; Rodrigo et al., 1990; Krasnopolsky, 2003). Molina-Cuberos et al. (2002) and Haider et al. (2011) have reported neutral model atmosphere of 12 gases ($CO_2$, $N_2$, Ar, $O_2$, CO, $H_2$, $H_2O$, O, $O_3$, NO, $NO_2$, and $HNO_3$) in the lower atmosphere of Mars. The density profiles of these gases are plotted in figure 1.3.

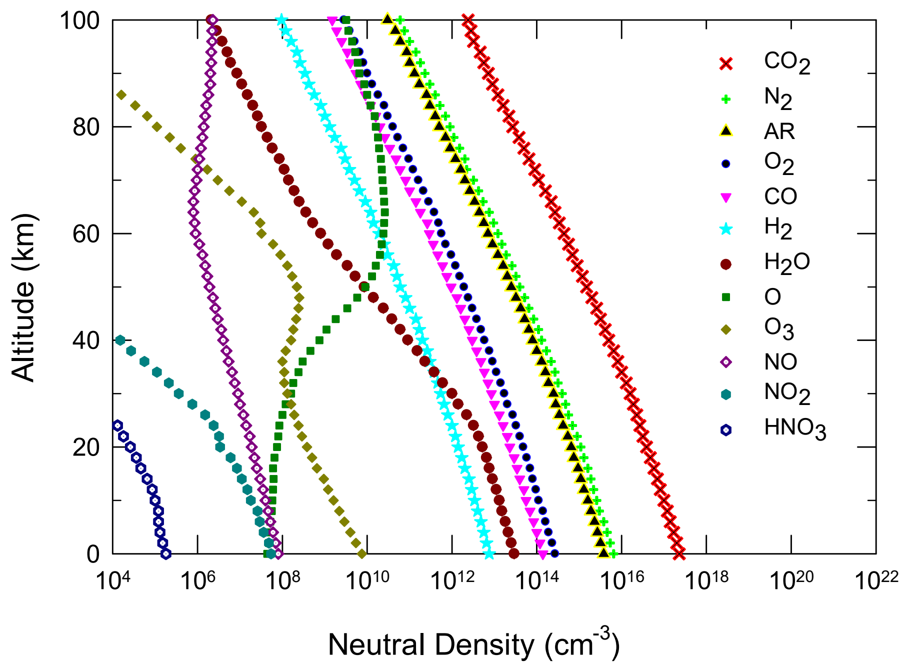


**Figure 1.3 Neutral model atmosphere in the lower atmosphere of Mars (taken from Molina-cuberos et al., 2002; Haider et al., 2011)**

## 1.2 HEATING RATE

Only Viking 1 and 2 Landers in situ have observed temperature profiles in the lower atmosphere of Mars (Nier and McElroy, 1977; Seiff and Kirk, 1977). These profiles represent a strong variability in thermal structure, which was attributed to wave motion in the lower atmosphere of Mars.

Prabhakara and Hogan (1965) first calculated the ozone and carbon dioxide heating rates due top absorption of solar ultraviolet radiation in lower atmosphere of Mars during daytime. They estimated ozone production from the Chapman photochemical reactions. They reported that the ozone heating rate does not produces any temperature maximum in Martain atmosphere. Later, Kuhn et al. (1979) predicted radiative equilibrium temperatures as high as ~ 10 K, incorporating ozone heating rates in their model. Linder (1991) calculated total atmospheric heating rate due to ozone in Ls = 343$^{o}$ and at northern mid-latitude (57$^{o}$ N) where the ozone maxima was observed then. It was suggested that Ozone heating rates can vary between 0.01-0.1 K/day between altitudes 0 - 40 km. Later, Gonzalez et al. (2005) proposed UV heating rate calculations using a fast scheme for the extension of Martian general circulation models. They estimated the vertical profile of the ozone heating rate for solar medium conditions. The maxima of the ozone heating rates calculated are ~ 0.06 K/day. They have considered the reference atmosphere from Nair et al. (1994). Recently, Von Paris et al. (2015) studied the effect of ozone on the atmospheric temperature on early Mars. They have suggested ozone may cause increase in temperatures of middle and upper atmosphere of Mars due to absorption of solar radiation causing heating in the middle atmosphere of Mars. We have reported the heating rates based on updated spectroscopic parameters, providing benchmark value of heating rates during global dust storm of Martian Year (MY) 28. Haider et al. (2019) reported significant enhancement in $O_3^+$ production rates during the dust storm season. Apart from ozone, dust absorbs solar radiation and leadings to warming of the lower atmosphere by diabatic heating. During perihelion seasons dust can affect the Hadley circulation and modify thermal tides (Zurek et al., 1992, Bougher et al., 2006, Wolkenberg et al., 2018). Bougher et al. (2015) suggested that dust storms change the atmosphere's opacity, and as a result the entire atmosphere expands due to aerosol heating. Evidences from the ground based measurements of Mars Science Laboratory suggest the recent dust storm of MY 34, the air temperatures rise due to heating by dust (Guzewich et al., 2018). Kass et al. (2019) studied the Mars Climate Sounder (MCS) observations of MY 34 presented that the dust and temperatures increased simultaneously. They suggested that the variations in this resulted due to dynamical heating/cooling and the non-uniform dust distribution in lower atmosphere of Mars. Smith (2019) analyzed Thermal Emission Imaging System (THEMIS) derived atmospheric temperatures datasets of MY 33 and MY 34 suggesting variations in the latter due to direct heating by the absorption of sunlight by dust and to general circulation patterns. They also suggested that the peak dust opacity ($\tau$) were >1 at southern latitudes during MY 34 at Ls = 185$^o$. Since Mars does not have intrinsic magnetic field, the solar wind particles, penetrates and interacts with the Mars atmosphere. The energetic particles undergo elastic and inelastic ionization collisions, causing ionization and dissociation of gases. This also causes heating of neutral atmosphere (Lillis et al., 2014; Bougher et al., 2015; Gerard et al., 2017). Solar events such as SEP are believed to form diffuse aurora on Mars (Schneider et al., 2015, 2018).

### 1.2.1 Motivation of the Present Thesis

The lower atmosphere of Mars is not studied in detail due to lack of measurements. Therefore, it is necessary to study the atmosphere of Mars in this region. It also contains the ionosphere which is the result of ionization of neutral atmosphere by EUV, X-rays, GCR, SEP and CME radiations. These radiations are emitted from the sun and contributing to the atmosphere in the form of different layers at different altitudes (Haider and Mahajan, 2014; Haider et al., 2011). The thin atmosphere of Mars has little effect on the radiation passing through it. This means most of the incoming radiation reaches on the planets' surface and then it escapes to space. This is due to the fact that Martian atmosphere has ~ 96% $CO_2$ and hardly any other green-house gases. This scenario changes dramatically after 3-4 years when a major dust storm occurs on Mars and dust clouds reflect or absorb up to 78% of the sun's radiation. In presence of dust storms the atmosphere warms and the surface cools. When surface cools, the surface winds fall and low level convection switches off removing the source of dust and triggering the storm's decay.

We have studied the effects of dust storm on the Mars atmosphere. The dust density and optical depths are calculated for different size of aerosol particles. The thermal emissions and atmospheric heating rates are also estimated. The causative mechanism of diffuse aurora in the nighttime atmosphere of Mars is modelled and compared with the MAVEN observations. These studies are very important and have a great interest to understand the atmospheric heating and meteorology in the lower atmosphere of Mars.

### 1.2.2 Chapterization

The present thesis contains eight chapters in which we have described methodology, neutral model atmosphere, thermal emissions, dust optical depth, seasonal variability of ozone heating rates, and diffuse aurora in the lower atmosphere of Mars.

In the first chapter we have introduced incoming and outgoing solar radiations from Mars. The EM and particle radiations describe the incoming radiation. The near, mid and far infrared radiations describe the outgoing radiation from Mars. In brief the physical processes occurring in the Martian atmosphere due to incoming and outgoing solar radiations are discussed. The lower and upper atmosphere of Mars are also studied in chapter 1.

In the second chapter we have described methodology for the calculations of dust density profiles, brightness temperature, ozone heating rates and auroral emissions using hybrid model and Analytical Yield Spectrum (AYS) approach. The dust density profiles are calculated in the Martian atmosphere by using the semi-empirical formula. The brightness temperature is calculated from radiative transfer method. The heating rates of $O_3$ are estimated due to absorption of UV radiation at Hartley band 200-300 nm.

In the third chapter the dust density profiles are calculated. The objective of this chapter is to study the dust layers of different size of aerosols particles and their impact in the lower atmosphere of Mars. The Martian atmosphere has a global circulation with zonal, meridional and vertical winds, which are considered to play an important role for the dust lifting in the form of global dust storm. The characteristics and properties of stratospheric aerosols are not understood. There is now the beginning for understanding the properties of different types of aerosols in the Marian atmosphere. The seasonal variability of dust aerosols is not known. This chapter will focus some of these important issues related to dust aerosols in the atmosphere of Mars.

In the fourth chapter we have calculated thermal emission spectra for Martian Year 28 when a major dust storm occurred on Mars at southern low latitude. We have compared our calculated results with thermal emission measurements made by PFS onboard MEX between wave numbers 250-1400 $cm^{-1}$. In presence of dust storm thermal emission spectra and brightness temperatures are reduced by factors of 3.0 and 1.3 respectively between wave numbers 900-1200 $cm^{-1}$ in comparison to that observed in absence of dust storm.

In the fifth chapter we have analysed data of column ozone obtained from Spectroscopy for the Investigation of the Characteristics of the Atmosphere of Mars (SPICAM) in MY 28 and MY 29 in presence and absence of dust storm respectively. The altitude profiles of ozone heating rates are calculated. It is found that ozone heating rates are severely affected by the global dust storm at latitude ~ $25^oS$.

In the sixth chapter we have used hybrid model and AYS approach to develop a model of diffuse aurora in the nighttime atmosphere of Mars. The emission intensity of $CO_2^+$ ($B^2\Sigma_u^+$ - $X^2\pi_g$) Ultraviolet Doublet (UVD) is calculated in the nighttime atmosphere of Mars.  This emission band has been observed in northern hemisphere of Mars during 17-21 December, 2014 from Imaging Ultraviolet Spectrograph (IUVS) instrument onboard MAVEN. We have found a good correlation between calculated and observed auroral emission intensity. The diffuse aurora is produced due to precipitation of Solar Energetic Particle (SEP) and proton-hydrogen ($H^+$-H) fluxes in the nighttime lower ionosphere of Mars.

In the seventh chapter we conclude and summarize the results obtained in the present thesis.

Finally, in the eighth chapter we have discussed future work to be carried out in the present thesis.

❒❒❒

# REFERENCES

Arya, A. S., Sarkar, S. S., Srinivas, A. R., Moorthi, S. M., Patel, V. D., Singh, R. B., et al. (2015). Mars Colour Camera: the payload characterization/calibration and data analysis from Earth imaging phase. Current Science, **109**. 1076-1086.

Belton, M. J., and Hunten, D. M. (1966). The Abundance and Temperature of CO2 in the Martian Atmosphere. The Astrophysical Journal, **145**, 454.

Bornmann, P. L., Speich, D., Hirman, J., Pizzo, V. J., Grubb, R., Balch, C., and Heckman, G. (1996). GOES solar x-ray imager: overview and operational goals. In GOES-8 and Beyond, International Society for Optics and Photonics, **2812**, 309-319.

Bougher, S. W., Bell, J. M., Murphy, J. R., Lopez-Valverde, M. A., and Withers, P. G. (2006). Polar warming in the Mars thermosphere: Seasonal variations owing to changing insolation and dust distributions. Geophysical Research Letters, **33**(2).

Bougher, S. W., Cravens, T. E., Grebowsky, J., and Luhmann, J. (2015). The aeronomy of Mars: Characterization by MAVEN of the upper atmosphere reservoir that regulates volatile escape. Space Science Reviews, **195**(1-4), 423-456.

Bougher, S. W., Engel, S., Hinson, D. P., and Forbes, J. M. (2001). Mars Global Surveyor radio science electron density profiles: Neutral atmosphere implications. Geophysical Research Letters, **28**(16), 3091-3094.

Gérard, J. C., Soret, L., Shematovich, V. I., Bisikalo, D. V., and Bougher, S. W. (2017). The Mars diffuse aurora: A model of ultraviolet and visible emissions. Icarus, **288**, 284-294.

González-Galindo, F., López-Valverde, M. A., Angelats i Coll, M., and Forget, F. (2005). Extension of a Martian general circulation model to thermospheric altitudes: UV heating and photochemical models. Journal of Geophysical Research: Planets, **110**(E9).

Guzewich, S. D., Lemmon, M., Smith, C. L., Martínez, G., de Vicente-Retortillo, Á., and Newman, C. E. et al. (2019). Mars science laboratory observations of the 2018/mars year 34 global dust storm. Geophysical Research Letters, **46**(1), 71-79.

Haider, S. A., Abdu, M. A., Batista, I. S., Sobral, J. H., Luan, X., Kallio, E., et al. (2009). D, E, and F layers in the daytime at high-latitude terminator ionosphere of Mars: Comparison with Earth's ionosphere using COSMIC data. Journal of Geophysical Research: Space Physics, **114**(A3).

Haider, S. A., and Mahajan, K. K. (2014). Lower and upper ionosphere of Mars. Space Science Reviews, **182**(1-4), 19-84.

Haider, S. A., and Masoom, J. (2019). Modeling of diffuse aurora due to precipitation of $H^+$-H and SEP electrons in the nighttime atmosphere of Mars: Monte Carlo simulation and MAVEN observation. Journal of Geophysical Research: Space Physics, **124**, 9566-9576.

Haider, S. A., Mahajan, K. K., and Kallio, E. (2011). Mars ionosphere: A review of experimental results and modeling studies. Reviews of Geophysics, **49**(4).

Haider, S. A., Siddhi, Y. S., Masoom, J., and Bougher, S. (2019). Effect of Dust Storm and GCR Impact on the Production Rate of $O_3^+$ in MY 28 and MY 29: Modeling and SPICAM Observation. Journal of Geophysical Research: Space Physics, **124**(3), 2271-2282.

Hanson, W. B., Sanatani, S., and Zuccaro, D. R. (1977). The Martian ionosphere as observed by the Viking retarding potential analyzers. Journal of Geophysical Research, **82**(28), 4351-4363.

Hartmann, W.K. (1989) Astronomy: The Cosmic Journey, Wadsworth Publication, Belmont, CA. pp 698.

Haus, R., and Titov, D. V. (2000). PFS on Mars Express: preparing the analysis of infrared spectra to be measured by the Planetary Fourier Spectrometer. Planetary and Space Science, **48**(12-14), 1357-1376.

Hinson, D. P., Simpson, R. A., Twicken, J. D., Tyler, G. L., and Flasar, F. M. (1999). Initial results from radio occultation measurements with Mars Global Surveyor. Journal of Geophysical Research: Planets, **104**(E11), 26997-27012.

Kass, D. M., Schofield, J. T., Kleinböhl, A., McCleese, D. J., Heavens, N. G., Shirley, J. H., and Steele, L. J. (2019). Mars Climate Sounder observation of Mars' 2018 global dust storm. Geophysical Research Letters, **46**.

Krasnopolsky, V. A. (2003). Spectroscopic mapping of Mars CO mixing ratio: Detection of north-south asymmetry. Journal of Geophysical Research: Planets, **108**(E2).

Kuhn, W. R., Atreya, S. K., and Postawko, S. E. (1979). The influence of ozone on Martian atmospheric temperature. Journal of Geophysical Research, **84**, 8341.

Lemmon, M. T., Wolff, M. J., Bell III, J. F., Smith, M. D., Cantor, B. A., and Smith, P. H. (2015). Dust aerosol, clouds, and the atmospheric optical depth record over 5 Mars years of the Mars Exploration Rover mission. Icarus, **251**, 96-111.

Lillis, R. J., Fox, J., Deighan, J., Bougher, S. W., Lee, Y., Cravens, T., and Rahmati, A. (2014, July). Photochemical escape of the Martian atmosphere: looking forward to MAVEN. In 6th Alfven Conference, Abstract, 7-11 July.

Lindner, B. L. (1991). Ozone heating in the Martian atmosphere. Icarus, **93**(2), 354-361.

Lissauer, J. J., and De Pater, I. (2013). Fundamental planetary science: physics, chemistry and habitability. Cambridge University Press.

Mahaffy, P. R., Benna, M., Elrod, M., Yelle, R. V., Bougher, S. W., Stone, S. W., and Jakosky, B. M. (2015). Structure and composition of the neutral upper atmosphere of Mars from the MAVEN NGIMS investigation. Geophysical Research Letters, **42**(21), 8951-8957.

Molina-Cuberos, G. J., Lichtenegger, H., Schwingenschuh, K., López-Moreno, J. J., and Rodrigo, R. (2002). Ion-neutral chemistry model of the lower ionosphere of Mars. Journal of Geophysical Research: Planets, **107**(E5), 3-1.

Nier, A. O., and McElroy, M. B. (1977). Composition and structure of Mars' upper atmosphere: Results from the neutral mass spectrometers on Viking 1 and 2. Journal of Geophysical Research, **82**(28), 4341-4349.

Parkinson, T. D., and Hunten, D. M. (1972). Spectroscopy and aeronomy of O2 on Mars. Journal of the Atmospheric Sciences, **29**(7), 1380-1390.

Pätzold, M., Tellmann, S., Häusler, B., Hinson, D., Schaa, R., and Tyler, G. L. (2005). A sporadic third layer in the ionosphere of Mars. Science, **310**(5749), 837-839.

Prabhakara, C., and Hogan Jr, J. S. (1965). Ozone and carbon dioxide heating in the Martian atmosphere. Journal of the Atmospheric Sciences, **22**(2), 97-109.

Read, P. L., Lewis, S. R., and Mulholland, D. P. (2015). The physics of Martian weather and climate: a review. Reports on Progress in Physics, **78**(12), 125901.

Rodrigo, R., Garcia-Alvarez, E., Lopez-Gonzalez, M. J., and Lopez-Moreno, J. J. (1990). A nonsteady one-dimensional theoretical model of Mars' neutral atmospheric composition between 30 and 200 km. Journal of Geophysical Research: Solid Earth, **95**(B9), 14795-14810.

Schneider, N. M., Deighan, J. I., Jain, S. K., Stiepen, A., Stewart, A. I. F., Larson, D., et al. (2015). Discovery of diffuse aurora on Mars. Science, **350**(6261), aad0313.

Schneider, N. M., Jain, S. K., Deighan, J., Nasr, C. R., Brain, D. A., Larson, D., et al. (2018). Global aurora on Mars during the September 2017 space weather event. Geophysical Research Letters, **45**(15), 7391-7398.

Seiff, A., and Kirk, D. B. (1977). Structure of the atmosphere of Mars in summer at mid-latitudes. Journal of Geophysical Research, **82**(28), 4364-4378.

Sheel, V., and Haider, S. A. (2016). Long-term variability of dust optical depths on Mars during MY24-MY32 and their impact on subtropical lower ionosphere: Climatology, modeling, and observations. Journal of Geophysical Research: Space Physics, **121**(8), 8038-8054.

Smith, M. D. (2019). THEMIS observations of the 2018 Mars global dust storm. Journal of Geophysical Research: Planets, **124**.

Von Paris, P., Selsis, F., Godolt, M., Grenfell, J. L., Rauer, H., and Stracke, B. (2015). Effect of $O_3$ on the atmospheric temperature structure of early Mars. Icarus, **257**, 406-416.

Wolkenberg, P., Giuranna, M., Grassi, D., Aronica, A., Aoki, S., Scaccabarozzi, D., and Saggin, B. (2018). Characterization of dust activity on Mars from MY27 to MY32 by PFS-MEX observations. Icarus, **310**, 32-47.

Zurek, R. W., Barnes, J. R., Haberle, R. M., Pollack, J. B., Tillman, J. E., and Leovy, C. B. (1992). Dynamics of the atmosphere of Mars. Mars, 835-933.

# CHAPTER - 2

# METHODOLOGY

# CONTENTS

*This chapter describes the methods used in the present thesis. There are four sections in this chapter. In the first section we have described observations of the dust opacity and a model calculation of the dust density that were carried out during the dust storm period. The second section describes Planck function, radiative transfer method and ozone heating rates. In third section hybrid model and AYS approach are described for the study of diffuse aurora.*

# 2.1 INTRODUCTION

There have been observed mainly two types of dust storms: (1) local dust storm and (2) global dust storm on Mars. The local dust storm occurs every year while global dust storm occurs after 3-4 MY (Sheel and Haider, 2016). In section 2.1.1 we have calculated altitude profiles of dust density. In section 2.2.2 the measurements of dust optical depths carried out by Thermal Emission Spectrometer (TES) and Thermal Emission Imaging System (THEMIS) onboard MGS and Mars Odyssey respectively are described at wavelength 9.3 μm from MY 24 to MY 32. In sections 2.2, 2.2.1 and 2.2.2 we have described Planck function and radiative transfer method for the calculation of temperature brightness in the lower atmosphere. The theory of ozone heating rates and wind speed are given in section 2.3, 2.3.1 and 2.3.2. In the final sections 2.4, 2.4.1 and 2.4.2 the AYS approach and hybrid model are described for the calculation of auroral emissions due to precipitation of monoenergetic and $H^+$-H electrons in the nighttime atmosphere of Mars.

## 2.1.1 Calculation of Dust Density Profile

The dust density profiles are calculated using the profile shape parameters obtained from recent observations carried out by Mars Climate Sounder (MCS) onboard Mars Reconnaissance Orbiter (MRO) (Heavens et al., 2014; Guzewich et al., 2014). We have estimated surface density of dust from the equation $n_s \sim n_o (\tau/\tau_o)$ where $\mathbf{n_s}$ is the surface density of dust particles, $\tau$ is taken from measured optical depth, which is plotted in figure 2.1 (Sheel and Haider, 2016), $\tau_o$ and $n_o$ are the optical depth and dust density equal to 0.1 and 2.0 $cm^{-3}$ in the clean atmosphere of Mars respectively (cf. Montabone et al., 2015). Using the surface density of the dust ($n_s$), we have calculated altitude profiles of the dust density from the following equations as given below:

$$N_{dust}(r,z) = k\, n_s\, n(r) A(z) \tag{2.1}$$

where n(r) is the density distribution of aerosol particles of radius r, k is a constant, and A (z) is a parameterized scheme at altitude z as given below:

$$A(z) = \left[1 - \exp\left[-\frac{(z-FH)^2}{FL^2}\right] + B\ \exp\left[-\frac{(z-PH)^2}{PT^2}\right]\right] \tag{2.2}$$

The parameters in the above equation are described as Fall off Height (FH), Fall off Length (FL), Pulse Height (PH), Pulse Thickness (PT), and finally ratio of peak to surface dust (B). These parameters are estimated from MCS observations (Heavens et al., 2014). The FH, PH, PT, and FL are represented in km. The B is a dimension less parameter. In Table (2.1) the values of these parameters are given. We have used the dust optical depth of THEMIS observations in the calculation of dust density at Ls = 240°, 280°, 300°, and 320° in absence of dust storm, presence of global dust storm, local dust storm, and disappearance of dust storm corresponding to $\tau$ = 0.1, 1.27, 0.5 and 0.1 respectively in MY28. The result of this model calculation is reproduced in chapter 3. Using a modified Gamma distribution function (Wolff et al., 2006) we can represent dust density profiles as shown below:

$$n(r) = r^a \exp(-br) \tag{2.3}$$

where $a = \frac{(1 - 3v_{eff})}{v_{eff}}$ and $b = \frac{1}{(v_{eff} \cdot r_{eff})}$, a and b are adjustable parameters, which control the size and width distribution of the Gamma distribution. The terms $\mathbf{r}_{eff}$ and $\mathbf{v}_{eff}$ are the effective radius and effective variance (width), respectively. Hansen and

Travis (1974) defined the effective radius and effective variance as given below:

$$r_{eff} = \frac{\int_{r_1}^{r_2} r^2\, n\,(r) r\, dr}{\int_{r_1}^{r_2} r^2\, n(r)\, dr} \tag{2.4}$$

$$v_{eff} = \frac{\int_{r_1}^{r_2} (r - r_{eff})^2\, r^2\, n(r) dr}{r_{eff}^2 \int_{r_1}^{r_2} r^2\, n(r) dr} \tag{2.5}$$

where $r_{eff}^2$ in the denominator of equation (2.5) makes $v_{eff}$ dimension less, $r_1 = 0$ and $r_2 = \infty$. The values of of $r_{eff}$ and $v_{eff}$ are varying for different aerosols. Thus the dust density will be different for different size of aerosols. In the present calculation we have used values of $r_{eff}$ and $v_{eff}$ to be 1.8 μm and 0.3, respectively. These values are representative for conditions sampled by the Compact Reconnaissance Imaging Spectrometer (CRISM) on board MRO (Wolff et al., 2009).

The minimum sizes of dust and water ice aerosols on Mars were measured to be ~ 0.2 and 0.1 μm respectively from CRISM observations (cf. Smith et al., 2013; Guzewich et al., 2014). The densities of dust aerosols are found to be very low at all altitudes for the radius values beyond 3 μm. Therefore, we have calculated size distribution of dust aerosols between 0.2 and 3 μm. The constant $k = \frac{1}{\int_0^\infty n(r) dr}$ is obtained by integrating n(r) from r to r + dr. Guzewich et al. (2014) have reported that the size of the dust particle is constant with respect to height in almost all seasons of southern hemisphere. Therefore, we assume the same value of $r_{eff}$ at all altitudes. Using above equations (2.1) - (2.5) we have calculated altitude profiles of dust densities at low latitudes for different size of aerosol particles of radius between 0.2 - 3.0 μm.

**Table 2.1: The parameters for the calculation of the dust density profile**

| Ls | Latitude | T | B | FH (km) | PH (km) | FL (km) | PT (km) |
|---|---|---|---|---|---|---|---|
| 240 | 0-10ºS | 0.1 | 0.75 | 42.0 | 25.0 | 12.0 | 6.0 |
| | 10-20ºS | | | | | | |
| | 20-30ºS | | | | | | |
| 280 | 0-10ºS | 1.27 | 0.86 | 76.0 | 48.0 | 12.0 | 18.0 |
| | 10-20ºS | | | | | | |
| | 20-30ºS | | | | | | |
| 300 | 0-10ºS | 0.5 | 0.33 | 45.0 | 32.0 | 9.0 | 4.0 |
| | 10-20ºS | | | | | | |
| | 20-30ºS | | | | | | |
| 320 | 0-10ºS | 0.1 | 0.75 | 42.0 | 25.0 | 12.0 | 6.0 |
| | 10-20ºS | | | | | | |
| | 20-30ºS | | | | | | |

## 2.1.2 Observations of dust optical depth

The Mariner 9 and Viking orbiter have observed two major dust storms in MY10 and MY13 from infrared spectrometers respectively (Martin, 1984, 1995). After two decades MGS and Mars Odyssey carried out continuous observations of infrared dust optical depths from TES (14 July 1998 to 31 August 2004) and THEMIS (1 September 2004 to 31 October 2014) instruments between MY 24 and MY 32 (Montabone et al., 2015). In figure 2.1 we have plotted these optical depths in the southern tropical region (25°-35° S) (Smith, 2002, 2008). In this region the optical depths increased to about 1.7 at Ls = 210° in MY 25 and to about 1.2 at Ls = 280° in MY 28. The TES measured optical depths daily at 2:00 P.M. and 2:00 A.M. The local time of THEMIS observation varies between 2:00 P.M. and 6:00 P.M. The morning observations are not used in our study. These datasets are averaged over longitudes. The uncertainty in the optical depth was estimated to be ± 0.3.

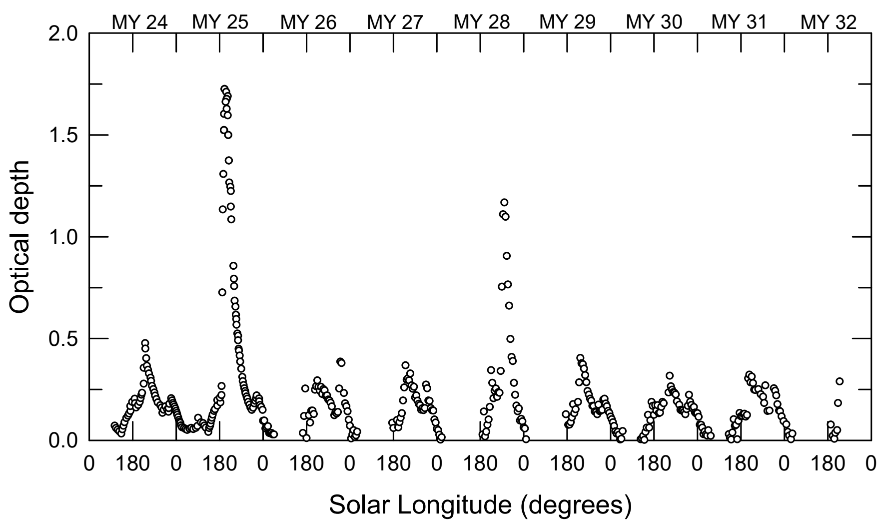


**Figure 2.1 The dust optical depth measured by TES and THEMIS instruments**

We have found that the dust density profiles represent a strong dust layer at about 50 km during the global dust storm period. The altitude profiles of these dust layers are shown in chapter 3 for different size of the aerosol particles. We report that the regional dust storm occurs every year during the summer at $\tau = 0.5$. The dust storm disappeared at $\tau = 0.1$. The major dust storms occurred at $\tau = 1.7$ and 1.2 in MY 25 and MY 28 at Ls = 210° and Ls = 280° respectively. We have not plotted optical depth of recent global dust storm that has been observed by the Opportunity Mars Exploration Rover (MER) and the MRO in June 2018 (MY34; https://mars.nasa.gov/resources/21917/atmospheric-opacity-from-opportunitys-point-of-view). The previous dust storms in MY 10, MY 13, MY 25, and MY 28 were slower to build in comparison to the new dust storm of MY 34. The new dust storm observed maximum UV dust opacity $\tau = 10.8$ on June 2018 at about Ls = 190° and spread quickly all over the globe. In chapter 3 our model result is dedicated to the previous dust storm ($\tau = 1.2$) that occurred in MY 28 in southern tropical region (25°-35° S).

## 2.2 BRIGHTNESS TEMPERATURE

In this section we have described Planck function, radiative transfer method and ozone heating rates in the lower atmosphere of Mars. The radiance spectra (or brightness temperatures) were observed by PFS onboard MEX between wave numbers 250-1400 $cm^{-1}$. The calculated results are compared with this observation in chapter 4. The propagation of radiation in the planetary atmospheres is influenced by absorption, emission and scattering by molecular species. Planck function cannot produce spectral features of thermal emission spectra. The spectral features of the thermal emission spectra can be reproduced by radiative transfer equation including scattering by atmospheric molecules. In brief theory of these three methods are given below:

## 2.2.1 Planck function

The observed thermal emission spectra are characterized by Planck function at the corresponding surface temperature under Local Thermodynamic Equilibrium condition (LTE) (Haus and Titov, 2000). The Planck function is expressed as given below:

$$B_T = \frac{2hc^2 v^3}{\left( e^{\frac{hcv}{kT}} - 1 \right)} \tag{2.6}$$

where $\mathbf{B_T}$ is the observed thermal emission spectra at brightness temperature **T**, **v** is the wave number, ***h*** is Planck constant, ***k*** is Boltzmann constant, and ***c*** is speed of light. Sometimes the equation (2.6) is expressed into two constants, $c_1$ and $c_2$. These constants are called as radiation constants. The first radiation constant $c_1$ = $2\pi hc^2$=3.74×10$^{16}$ W.m$^2$. The second radiation constant $c_2$ = $hc/k$=1.44×10$^2$ m.K.

The Planck function is varying with altitudes because the temperature T is altitude dependent. The altitude-dependent of brightness temperature (Haus and Titov, 2002) can be calculated by inverting equation (2.6) as follows:

$$T_B = \frac{hcv}{k \ln\left( \frac{2hc^2 v^3}{B_T + 1} \right)} \tag{2.7}$$

In the above equations (2.6) and (2.7) we have not considered molecular scattering under LTE condition. Therefore, these equations cannot calculate the spectral features of thermal emission spectrum. The molecular scattering is considered in the radiative transfer method.

### 2.2.2 Radiative transfer method

The radiative transfer equation describes that the radiation is affected through the emission, absorption and scattering processes (Ignatiev et al., 2005). These three processes are coupled and can be represented as:

$$\frac{dI_\lambda}{ds} = -\left(a_\lambda(s) + d_\lambda(s)\right) I_\lambda(s) + a_\lambda(s) B_\lambda(T) + \frac{d\lambda}{4\pi}\int P(\Omega,\Omega') I_\lambda(\Omega')\, d\Omega' \quad (2.8)$$

The sum $a_\lambda + d_\lambda$ explain the extinction coefficient and can be expressed in terms of atmospheric optical depth in vertical direction ***s***:

$$d\tau_\lambda = \left(a_\lambda(s) + d_\lambda(s)\right) ds \quad (2.9)$$

Thus

$$\frac{dI_\lambda(\tau)}{d\tau} = -\ I_\lambda(\tau) + w_a\ B_\lambda(T) + \frac{w_d}{4\pi}\int P(\Omega,\Omega') I_\lambda(\Omega')\, d\Omega' \quad (2.10)$$

where $w_a = {a_\lambda}/{(a_\lambda + d_\lambda)}$ and $w_d = {d_\lambda}/{(a_\lambda + d_\lambda)}$ are absorption and scattering albedo respectively. By using above equations we get

$$I_\lambda(\tau) = I_\lambda(0) e^{-\tau} + \int_0^\tau B_\lambda(T) e^{-(\tau'-\tau)}\, d\tau' \quad (2.11)$$

In equation (2.11) first term is a pure extinction term while second term describes the emission from the atmosphere. Rayleigh scattering due to molecules is significantly low in the Martian atmosphere because of its $\lambda^{-4}$ dependence (Haus and Titov, 2000). Therefore, Rayleigh scattering is not included in equation (2.11). $I_\lambda(0)$ is the emitted radiation from the surface of Mars at wavelength λ. The atmospheric contributions have been incorporated at every height. The contributions emitted from the elements of distance dτ at different τ' along the path are themselves attenuated by the exponential factor over (τ-τ'). The optical depth τ is defined as:

$$\tau(s)=\int_0^s N_{co_2}\ \sigma_{co_2}(\lambda)ds+\int_0^s N_{H_2O}\ \sigma_{H_2O}(\lambda)\,ds+\int_0^s N_{dust}\ \sigma_{dust}(\lambda)\,ds \qquad (2.12)$$

where **σ** represents the absorption cross sections of $CO_2$, $H_2O$ and dust in the infrared wavelength range 250-1400 $cm^{-1}$. The cross sections for $CO_2$ and $H_2O$ are taken from *Exomol Spectroscopic Database* (Tennyson and Yurchenko, 2012). The cross section of dust is taken from Conrath et al. (1973). **N** represents the number density of $CO_2$, $H_2O$ and dust. The number densities of $CO_2$ and $H_2O$ are taken from MCD v5.2 for Ls=240°, 280°, 300° and 320° at low latitude region averaged over 0°-10° S, 10°-20° S and 20°-30°S. The dust density profiles are calculated using the profile shape parameters obtained from recent observations carried out by Mars Climate Sounder (MCS) onboard Mars Reconnaissance Orbiter (MRO) (Heavens et al., 2014; Guzewich et al., 2014).

### 2.2.3 Ozone heating rates

The ozone heating rate is calculated in the Martian atmosphere due to absorption of solar radiation of wavelength band 200-300 nm as given below:

$$\rho_a\, c_p \frac{\partial T}{\partial t}=\int_0^\lambda F(\infty,\lambda)\ \sigma_a(\lambda)\,\mathrm{n}(\mathrm{z})\exp\{-\tau(\mathrm{z})\}\,d\lambda \qquad (2.13)$$

$$\tau=\int_0^\infty \sigma_a(\lambda)\,n(z)\sec\theta\,dz \qquad (2.14)$$

where ***F(∞,λ)*** is the solar flux at the top of the atmosphere, $\sigma_a(\lambda)$ is the absorption cross section at wavelength range 200-300 nm, **n**(z) is the neutral density of ozone at altitude **z**, **τ** is the optical depth, $\rho_a$ is the air density, and $\mathbf{c_p}$ is the specific heat. The ***sec θ*** is a zenith angle. The optical depth, specific heat, neutral and air density are taken from Millour et al. (2014). The solar flux and absorption cross sections are taken from Tobiska et al. (2000) and Serdyuchenko et al. (2014) respectively. In chapter 5 ozone heating rates are calculated at high solar zenith angle. The ozone heating rates are also estimated in different seasons at various latitudes.

## 2.3 MODELING OF AURORAL EMISSIONS

There have been observed three types of aurora on Mars viz. (1) discrete aurora, (2) proton aurora, and (3) diffuse aurora from the Imaging Ultraviolet Spectrograph (IUVS) instrument (Schneider et al., 2015). The discrete aurora has been observed near the mini-magnetosphere in the southern hemisphere of Mars during the nighttime (Bertaux et al., 2005). The proton aurora is observed due to energetic proton precipitation into the dayside Martian atmosphere (Deighan et al., 2018). The diffuse aurora is observed in the nighttime due to precipitation of SEP electrons down up to 1 microbar altitude (Schneider et al., 2015). In this chapter we have described theory of auroral emissions. Modelling studies of aurora along with observations serves as an essential tool to understand the chemical and physical processes occurring during the aurora emissions. To model these emissions and estimate its intensity, different approaches can be applied. We have used four dimensional AYS approach and hybrid model as given below:

### 2.3.1 AYS method

In AYS model the monoenergetic electrons of energy range from 25 eV to 10 keV were introduced in a gas medium. Using this method, the energy of secondary or tertiary electrons and their positions were calculated at that time when primary electrons ionize/excite the atmospheric gases. In this way two, three, four and five dimensional yield spectrum functions U $(E, E_o)$, U $(E, z, E_o)$, U $(E, r, z, E_o)$ and U $(E, r, z, E_o, \theta)$ were generated respectively for the calculation of the yield of any state in the mixture of gases (Green et al., 1977; Singhal et al., 1980; Singhal and Green, 1981; Haider et al., 2011; Haider and Mahajan, 2014). These functions depend on incident energy $\mathbf{E_o}$, secondary energy **E**, radial distance **r**, height **z** and polar angle **θ**. The yield spectrum function represents the energy spectrum of all the electrons in the medium. The function for Z < 0 and Z > 0 represents the backscattered and forward electrons respectively.

Recently MAVEN has observed SEP electron in the upper atmosphere of Mars. These electrons are precipitating down into the nighttime atmosphere along the Interplanetary Magnetic Field (IMF) field lines at some pitch angle and ionizing the gases. We have used four dimensional AYS model. The backscattered SEP electrons escaping upward are not considered in our model. The four dimensional yield spectrum is represented as given below:

$$U(E, r, Z, E_0) = U_i(E, r, Z, E_0)H(E_0 - E - E_m) + \delta(E_0 - E)D(r, Z, E_0) \qquad (2.15)$$

where **H** is the Heaviside function, $\mathbf{E_m}$ is the minimum threshold energy of the ionization state and $\delta(E_o\text{-}E)$ is the Dirac delta function which allows the contribution of the source term $D(r, Z, E_o)$. The expression for $U_i(E, r, Z, E_o)$ is given below:

$$U_i(E,r,Z,E_o) = \sum_{i=0}^{2} \frac{A_i}{R^3} \chi^i G_i\ (r,z) \qquad (2.16)$$

$$G_i(r,Z) = \exp\left[-\frac{\alpha_i\, r}{1+\delta_i\, Z} + \beta_i^2\, Z^2 - \gamma_i Z\right] \qquad (2.17)$$

$$R = R_o\left(\frac{E_o}{1000}\right)^q + \tau \qquad (2.18)$$

$$\chi = \frac{\left(\frac{E_o}{1000}\right)^{0.585}}{(E+1)} \qquad (2.19)$$

where **R** is a scale factor. $\mathbf{R_o}$, $\boldsymbol{\tau}$, and **q** in equation (2.17) are given by Singhal and Green (1981). The source term D(r, Z, $E_o$) in equation (2.15) is represented as follows:

$$D(r,Z,E_0)=\frac{A_S}{R^3}G_S \tag{2.20}$$

$$G_s(r,z) = \exp\left[-\frac{\alpha_s r}{1+\delta_s Z} - \gamma_s Z\right] \tag{2.21}$$

where $\alpha_o$, $\beta_o$, $\gamma_o$, $\delta_o$, $\alpha_1$, $\beta_1$, $\gamma_1$, $\delta_1$, $\delta_2$, $\delta_s$ and $\gamma_s$ are dimension less parameters which decide shape of the yield spectra (Singhal and Green, 1981). The parameters $\alpha_2$, $\beta_2$, $\gamma_2$ and $\alpha_s$ are dependent on incident electron energy $E_o$. $A_o$, $A_1$, $A_2$ and $A_s$ are amplitude parameters which are also dependent on energy $\mathbf{E_o}$. For mixture of gases in the atmosphere of Mars the composite yield spectra (Seth et al., 2002) is obtained by weighting the component of the yield spectra as given below:

$$U^c(E,r,Z,E_0) = \sum f_i \, U_i(E,r,Z,E_0) \tag{2.22}$$

$$f_i = \frac{S_i \, n_i}{\sum S_j \, n_j} \tag{2.23}$$

where $\mathbf{n_i}$ is the number density of $i^{th}$ gas, $S_i/S_j$ is the average value of $\sigma_{Ti}(E) / \sigma_{Tj}(E)$ between $\mathbf{E_m}$ and $\mathbf{E_o}$. The $\boldsymbol{\sigma_{Ti}}$ is the total electron impact ionization cross section of $CO_2^+$. The variable Z in equation (2.15) to (2.21) is connected with h as given by:

$$Z(h) = \frac{1}{R}\int_h^\infty \frac{\rho(h)}{\cos\theta}\, dh \tag{2.24}$$

The altitude profiles of ion production rates of $CO_2^+$, $N_2^+$ and $O^+$ are calculated due to SEP electron impact of energy $E_o$ and flux $\varphi(E_o)$ from the following expression:

$$J_{ki}(h) = 2\pi \int_0^\infty r\,dr \int_{E_m}^{E_0} U^c(E,r,Z,E_o)\, \varphi(E_o)\rho(Z)\, \rho_{ki}\, dE \tag{2.25}$$

where $\mathbf{p_{ki}}$ is the ionization probability (Haider et al., 2013) of $\mathbf{k}^{th}$ state for $\mathbf{i}^{th}$ gas, $\boldsymbol{\rho}(Z)$ is the gas density (in $gm/cm^3$) and $\boldsymbol{\varphi}(E_o)$ is the incident SEP electron flux of energy $\mathbf{E_o}$ (in $cm^{-2}\ s^{-1}\ sr^{-1}$). Since incident flux $\varphi(E_o)$ is assumed to be distributed isotropically over the downward hemisphere of Mars, the equation (2.25) is integrated over pitch angle ($0 < \theta < \pi/2$) with weighting factor of $2\pi \cos\theta$ (Haider et al., 2013).

## 2.3.2 Hybrid model

The hybrid model is used by several investigators (Kallio and Janhunen, 2001; Haider et al., 2002, 2009, 2011). In this model $H^+$ ions are accelerated up to energies 10 keV in presence of electric and magnetic fields as given below:

$$\frac{dV_i}{dt} = \frac{q_i}{m_i}\left(E + V_i \times B\right) + \frac{F_i}{m_i} \tag{2.26}$$

where $\mathbf{V_i}$, $\mathbf{m_i}$, and $\mathbf{q_i}$ are velocity, mass, and charge of an $\mathbf{i}^{th}$ ion respectively. $\mathbf{F}$ is a Lorentz force. In this model magnetic field $\mathbf{B}$ is calculated by Faraday's law. The electric field $\mathbf{E}$ is calculated from electron momentum equation as follows:

$$E = -u_e \times B - \frac{\nabla p_e}{e n_e} \tag{2.27}$$

where $\mathbf{u_e}$ is the bulk velocity with pressure gradient $\nabla p_e = K_B T_e \nabla n_e$, $\mathbf{T_e}$ is the electron temperature, $\mathbf{K_B}$ is a Boltzmann constant, and $\mathbf{n_e}$ is the electron density. The $\mathbf{u_e}$ is calculated from the current density '**s**' as follows:

$$u_e = \frac{\sum_i q_i n_i u_i}{e n_e} \tag{2.28}$$

Neutrality condition the electron density $\mathbf{n_e}$ is equal to the total density of positive ions

$$n_e = \frac{\sum_i q_i n_i}{e} \tag{2.29}$$

Mars has no dipole magnetic field (Acuna et al., 1998). The interplanetary shock compresses the Magnetosheath of Mars during the diffuse aurora. In the Magnetosheath, the planetary neutral are mainly H atoms of hydrogen corona. In this region, Energetic Neutral Atom (ENA) is produced by charge exchange reaction between solar wind protons and hydrogen corona. An ENA is the product of $H^+$ and H (Galli et al., 2008) and can be represented as $H^+$-H. ENA are observed in the nighttime of Mars (Milillo et al., 2009). The atmospheric effects of $H^+$-H precipitation in the nightside ionosphere were included in the hybrid model by Kallio and Barabash (2001) and Haider et al. (2002) using Monte Carlo simulation. In this model incident flux ~ 1.0 x $10^6$ $cm^{-2}$ $s^{-1}$ is estimated at the top of the Mars' atmosphere. The ion production rates of $CO_2^+$, $N_2^+$, and $O^+$ are calculated due to precipitation of this flux in the nighttime atmosphere of Mars at solar zenith angle (SZA) 105° and 127°. The results of this model calculation are described in chapter 5.

❒❒❒

# REFERENCES

Acuna, M. H., Connerney, J. E. P., Wasilewski, P. A., Lin, R. P., Anderson, K. A., Carlson, C. W., et al. (1998). Magnetic field and plasma observations at Mars: Initial results of the Mars Global Surveyor mission. Science, **279**(5357), 1676-1680.

Bertaux, J. L., Leblanc, F., Witasse, O., Quemerais, E., Lilensten, J., Stern, S. A., et al. (2005). Discovery of an aurora on Mars. Nature, **435**(7043), 790.

Conrath, B., Curran, R., Hanel, R., Kunde, V., Maguire, W., Pearl, J., et al. (1973). Atmospheric and surface properties of Mars obtained by infrared spectroscopy on Mariner 9. Journal of Geophysical Research, **78**(20), 4267-4278.

Deighan, J., Jain, S. K., Chaffin, M. S., Fang, X., Halekas, J. S., Clarke, J. T., et al. (2018). Discovery of a proton aurora at Mars. Nature Astronomy, **2**(10), 802.

Galli, A., Wurz, P., Kallio, E., Ekenbäck, A., Holmström, M., Barabash, S., et al. (2008). Tailward flow of energetic neutral atoms observed at Mars. Journal of Geophysical Research: Planets, **113**(E12).

González-Galindo, F., López-Valverde, M. A., Angelats i Coll, M., and Forget, F. (2005). Extension of a Martian general circulation model to thermospheric altitudes: UV heating and photochemical models. Journal of Geophysical Research: Planets, **110**(E9).

Green, A. E. S., Jackman, C. H., and Garvey, R. H. (1977). Electron impact on atmospheric gases, 2. Yield spectra. Journal of Geophysical Research, **82**(32), 5104-5111.

Guzewich, S. D., Smith, M. D., and Wolff, M. J. (2014). The vertical distribution of Martian aerosol particle size. Journal of Geophysical Research: Planets, **119**(12), 2694-2708.

Haider, S. A., and Mahajan, K. K. (2014). Lower and upper ionosphere of Mars. Space Science Reviews, **182**(1-4), 19-84.

Haider, S. A., Pandya, B. M., and Molina-Cuberos, G. J. (2013). Nighttime ionosphere caused by meteoroid ablation and solar wind electron-proton-hydrogen impact on Mars: MEX observation and modeling. Journal of Geophysical Research: Space Physics, **118**(10), 6786-6794.

Haider, S. A., Mahajan, K. K., and Kallio, E. (2011). Mars ionosphere: A review of experimental results and modeling studies. Reviews of Geophysics, **49**(4).

Haider, S. A., Abdu, M. A., Batista, I. S., Sobral, J. H., Kallio, E., Maguire, W. C., and Verigin, M. I. (2009). On the responses to solar X-ray flare and coronal mass ejection in the ionospheres of Mars and Earth. Geophysical Research Letters, **36**(13).

Haider, S. A., Seth, S. P., Kallio, E., and Oyama, K. I. (2002). Solar EUV and electron-proton-hydrogen atom-produced ionosphere on Mars: Comparative studies of particle fluxes and ion production rates due to different processes. Icarus, **159**(1), 18-30.

Hansen, J. E., and Travis, L. D. (1974). Light scattering in planetary atmospheres. Space science reviews, **16**(4), 527-610.

Haus, R., and Titov, D. V. (2000). PFS on Mars Express: preparing the analysis of infrared spectra to be measured by the Planetary Fourier Spectrometer. Planetary and Space Science, **48**(12-14), 1357-1376.

Heavens, N. G., Johnson, M. S., Abdou, W. A., Kass, D. M., Kleinböhl, A., McCleese, D. J., et al. (2014). Seasonal and diurnal variability of detached dust layers in the tropical Martian atmosphere. Journal of Geophysical Research: Planets, **119**(8), 1748-1774.

Ignatiev, N. I., Grassi, D., and Zasova, L. V. (2005). Planetary Fourier spectrometer data analysis: Fast radiative transfer models. Planetary and Space Science, **53**(10), 1035-1042.

Kallio, E., and Barabash, S. (2001). Atmospheric effects of precipitating energetic hydrogen atoms on the Martian atmosphere. Journal of Geophysical Research: Space Physics, **106**(A1), 165-177.

Kallio, E., and Janhunen, P. (2002). Ion escape from Mars in a quasi-neutral hybrid model. Journal of Geophysical Research: Space Physics, **107**(A3), SIA-1.

Martin, L. J. (1984). Clearing the Martian air: The troubled history of dust storms. Icarus, **57**(3), 317-321.

Martin, T. Z. (1995). Mass of dust in the Martian atmosphere. Journal of Geophysical Research: Planets, **100**(E4), 7509-7512.

Milillo, A., Mura, A., Orsini, S., Massetti, S., son Brandt, P. C., Sotirelis, T., et al. (2009). Statistical analysis of the observations of the MEX/ASPERA-3 NPI in the shadow. Planetary and space science, **57**(8-9), 1000-1007.

Millour, E., et al. (2014), A new Mars Climate Database v5.1, The Fifth International Workshop on Mars Atmosphere: Modeling and Observations, Oxford, U. K.

Montabone, L., Forget, F., Millour, E., Wilson, R. J., Lewis, S. R., Cantor, B., et al. (2015). Eight-year climatology of dust optical depth on Mars. Icarus, **251**, 65-95.

Schneider, N. M., Deighan, J. I., Jain, S. K., Stiepen, A., Stewart, A. I. F., Larson, D., et al. (2015). Discovery of diffuse aurora on Mars. Science, **350**(6261), aad0313.

Serdyuchenko, A., Gorshelev, V., Weber, M., Chehade, W., and Burrows, J. P. (2014). High spectral resolution ozone absorption cross-sections-Part 2: Temperature dependence. Atmospheric Measurement Techniques, **7**(2), 625-636.

Seth, S. P., Haider, S. A., and Oyama, K. I. (2002). Photoelectron flux and nightglow emissions of 5577 and 6300 Å due to solar wind electron precipitation in Martian atmosphere. Journal of Geophysical Research: Space Physics, **107**(A10), SIA-19.

Sheel, V., and Haider, S. A. (2016). Long-term variability of dust optical depths on Mars during MY24-MY32 and their impact on subtropical lower ionosphere: Climatology, modeling, and observations. Journal of Geophysical Research: Space Physics, **121**(8), 8038-8054.

Singhal, R. P., Jackman, C. H., and Green, A. E. S. (1980). Spatial aspects of low-and medium-energy electron degradation in N2. Journal of Geophysical Research: Space Physics, **85**(A3), 1246-1254.

Singhal, R. P., and Green, A. E. S. (1981). Spatial aspects of electron energy degradation in atomic oxygen. Journal of Geophysical Research: Space Physics, **86**(A6), 4776-4780.

Smith, M. D. (2008). Spacecraft observations of the Martian atmosphere. Annual Review of Earth and Planetary Sciences, **36**, 191-219.

Smith, M. D., Wolff, M. J., Clancy, R. T., Kleinböhl, A., and Murchie, S. L. (2013). Vertical distribution of dust and water ice aerosols from CRISM limb-geometry observations. Journal of Geophysical Research: Planets, **118**(2), 321-334.

Tennyson, J., and Yurchenko, S. N. (2012). ExoMol: molecular line lists for exoplanet and other atmospheres. Monthly Notices of the Royal Astronomical Society, **425**(1), 21-33.

Tobiska, W. K., Woods, T., Eparvier, F., Viereck, R., Flyoyd, L., Bouwer, D., et al. (2000) The SOLAR2000 empirical solar irradiance model and forecast tool. Journal of Atmospheric and Solar-Terrestrial Physics, **62**(14), 1233-1250.

Wolff, M. J., Smith, M. D., Clancy, R. T., Spanovich, N., Whitney, B. A., Lemmon, M. T., et al. (2006). Constraints on dust aerosols from the Mars Exploration Rovers using MGS overflights and Mini-TES. Journal of Geophysical Research: Planets, **111**(E12).

Wolff, M. J., Smith, M. D., Clancy, R. T., Arvidson, R., Kahre, M., Seelos, F., et al. (2009). Wavelength dependence of dust aerosol single scattering albedo as observed by the Compact Reconnaissance Imaging Spectrometer. Journal of Geophysical Research: Planets, **114**(E2).

❐❐❐

# CHAPTER - 3

# EFFECT OF DUST ON THE LOWER ATMOSPHERE OF MARS

# CONTENTS

*The properties of the dust-aerosol have been studied in the Martian atmosphere with the recent infrared thermal emission datasets obtained from THEMIS onboard Mars Odyssey. These datasets confirmed that the dust-aerosol represents spatial and temporal variability. There has been attempt to understand the size distribution and structure of the dust profile in the Martian atmosphere. In this chapter we have analyzed these data. A global dust storm occurred in MY 28 when THEMIS observed high dust opacity in the tropics between Ls = 270° and 300° during a couple of weeks. We have calculated the dust densities in MY 28 between altitude 0 and 70 km at tropical latitude 0-30°S for Ls = 240°, 270°, 300° and 320° corresponding to low, medium, high and absence of dust storm period. The dust opacities during these dust storm periods were observed to be $\tau = 0.1$, 0.5, 1.27, and 0.1 respectively. The objective of this chapter is to study the dust density profiles of different size of aerosol particles and their influences in the lower atmosphere of Mars.*

# 3.1 INTRODUCTION

The Martian atmosphere has a global circulation with zonal, meridional, and vertical winds. These winds are considered to play an important role for the dust lifting during the storm period. The dust optical depth increases in the Martian atmosphere. Various studies have been reported that the size of dust particles varies between 0.01-10 μm (Montabone and Forget, 2017). The concentration of the dust also varies with season and location and forms a layer in the Martian atmosphere (Bougher et al., 2015). This layer acts as a perturbation in the lower atmosphere (Liu et al., 2018). This disturbance involves dust aerosol radiative heating and cooling which modifies thermal structure of the Mars' atmosphere. Guzewich et al. (2014) suggested that the dust particles may be carried by vertical transport to altitudes as high as 80 km. Heavens et al. (2014) have reported a dust layer at about 50 km in the lower atmosphere of Mars. They studied seasonal and diurnal variability of the dust layers. Sheel and Haider (2016) emphasized that the dust acts as major source of heating and lead to generate vertical and horizontal winds. In this chapter we have calculated the dust density profiles in MY 28 between altitude 0 and 70 km at latitude 10°S and Ls = 240°, 280°, 300°, and 320° during low, high, medium, and the absence of dust storms corresponding to $\tau = 0.1$, 1.27, 0.5, and 0.1, respectively.

### 3.1.1 Thermal emission measurements

In chapter 2 we have discussed dust optical depth measurements of TES and THEMIS instruments carried by MGS and Mars Odyssey respectively at a very short latitude range $25^{o}$-$35^{o}$S. In this chapter the global dust optical depths between northern and southern hemispheres at Ls from 0 to $360^{o}$ are plotted in figure 3.1 for nine Martian years during MY 24 to MY 32. In this figure the dust optical depths are plotted at $5^{o}$x$5^{o}$ grids of latitudes and Ls. In MY 25 and MY 28 two major dust storms were observed on Mars at southern low latitudes. The MGS data are plotted between MY 24 (from Ls=$0^{o}$) and MY27 (till Ls=$81^{o}$) followed by Mars Odyssey data till MY 32. We have used dust optical depths of second major dust storm of MY 28 in the calculation of dust density. During dust storm period of MY 28 the optical depths increased to about 1.27 at Ls = $280^{o}$. After a couple of days, the intensity of this dust storm reduces and the optical depth decreases to 0.5 at Ls = $300^{o}$, which we consider medium dust storm. This observation shows that the dust storm took about 3 months for the dust to settle down to its normal condition. Very low optical depth 0.1 is observed before and after the major dust storms at about Ls = $240^{o}$ and $320^{o}$. We have considered it a background aerosol loading in the clean atmosphere when the dust storm was absent.

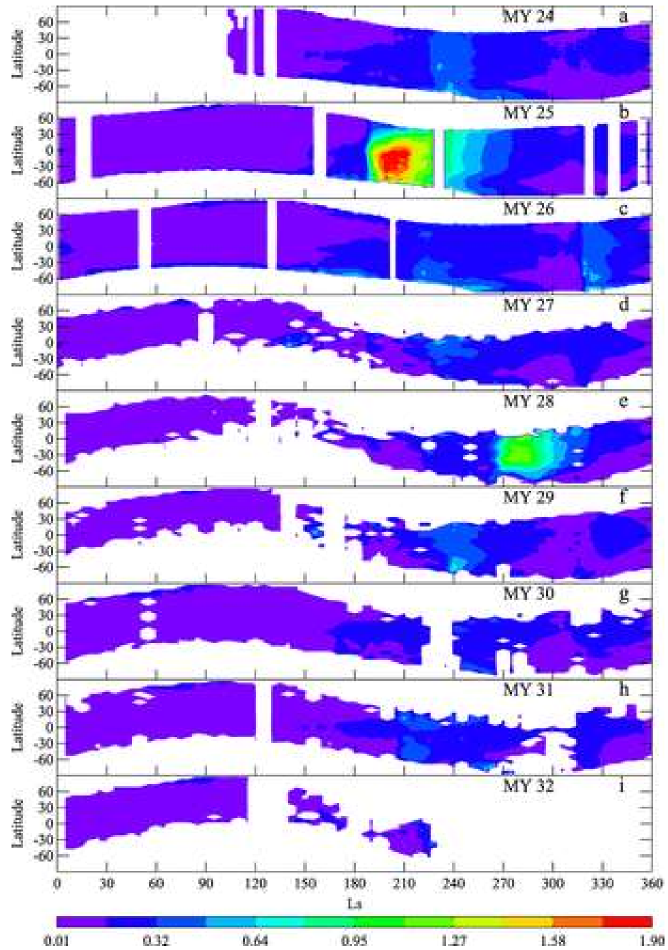


**Figure 3.1: The dust optical depths obtained from MGS and Mars Odyssey observations for (a) MY24, (b) MY25, (c) MY26, (d) MY27, (e) MY28, (f) MY29, (g) MY30, (h) MY31, and (i) MY32.**

The above optical depths observed by THEMIS instrument in MY28 are used in the calculation of density profiles of dusts of different particle sizes in presence and absence of dust storm. There is a little variation in the opacity as the storm decays (Ls=300°). During decay period of dust storm the optical depths do not change significantly with latitude. The southern polar region is always clear during dust storm period. Hellas basin (30°S, 250°W) appears as a dusty region. We do not find dust activity in Argre basin (50°S, 240°W). The low opacities occur in the afternoon, suggesting that Argyre basin was indeed clear of dust at the peak of the storm. Perhaps there was a wind in Argyre basin that keeps dust out during the storm. It is due to Hellas' unique topography which allows it to behave independently from Argyre basin during major dust storms (Fenton et al., 1997).

### 3.1.2 Altitude profiles of Dust Density

In figures 3.2, 3.3, 3.4, and 3.5 we have shown fifteen altitude profiles of dust densities in MY28 for aerosol particles of sizes 0.2 to 3.0 μm at latitude range $10^o$-$20^o$S for Ls = $240^o$, $280^o$, $300^o$ and $320^o$ respectively. Dust densities between 0 km and 70 km at latitude range $0^o$-$10^o$S, $10^o$-$20^o$S and $20^o$-$30^o$S have been calculated. The optical depth is not changing significantly with latitude at fix Ls. Thus, the dust concentrations at latitude range $0^o$-$10^o$S and $20^o$-$30^o$S are nearly same as estimated for latitude range $10^o$-$20^o$S. Our calculations show that the particles can lift up to 70 km from the surface of Mars during high dust storm period at Ls = $280^o$ and $\tau = 1.2$. The concentrations of dust aerosols of size > 3 μm are nearly zero in the lower atmosphere of Mars. We have assumed that atmosphere is clean when optical depth is equal to 0.1. Haider et al. (2015) found that the dust density is high for smaller sized particles. This is due to the fact that gravitation velocity is directly proportional to the mass of aerosol particles. The concentrations of larger particles are lower than the small particles because they settle down quickly. It is found that the small dust particle of size 0.2 micron produces peak densities ~ 0.21 $cm^{-3}$, 3.0 $cm^{-3}$, 0.77 $cm^{-3}$ and 0.21 $cm^{-3}$ at 25 km, 50 km, 35 km and 25 km respectively. The dust densities are very low at Ls = $240^o$ and $320^o$ during pre and post storm seasons respectively. The maximum dust density is estimated during peak dust storm at Ls = $280^o$ and $\tau = 1.2$. The dust density is reduced during the decline period of the dust storm at Ls = $300^o$ and $\tau = 0.5$ by factor of four from the peak dust storm period. Recently vertical distribution of dust aerosol is estimated by Guzewich et al. (2014) and Heavens et al. (2014), who found two distinct layers, one at altitude ~ 20-30 km and other at altitude ~ 45-65 km from the observations made by CRISM and MCS experiments respectively. Our calculated profiles of dust concentrations are consistent with the dust layers observed by CRISM and MCS experiments respectively. These profiles produce an elevated maximum in the lower atmosphere of Mars.

The figure 3.2 shows the dust density profiles during the pre-storm condition. These condition prevails on Mars at given point of time. This indicates that the dust is always suspended in the lower atmosphere of Mars. The concentration of the 0.2 micron is abundant and the 3.0 is the least. The 0.2 micron particle creates a layer at ~25 km with peak density at 0.21 $cm^{-3}$. It is also to be noted that the distinct peak in the sizes can be clearly seen up to particles sizes of 2.0 micron. The dust particles sizes higher than 2.0 micron are less comparatively at Ls = 240$^{o}$. This is a clear indication that larger dust particles are not lifted at higher heights during clear conditions. The geophysical parameter such as wind is also nominal, unable to lift such larger particles in the atmosphere. During Ls = 240$^{o}$, the optical depth was the least (0.1) and thus estimated dust profiles are least compared to the other seasons.

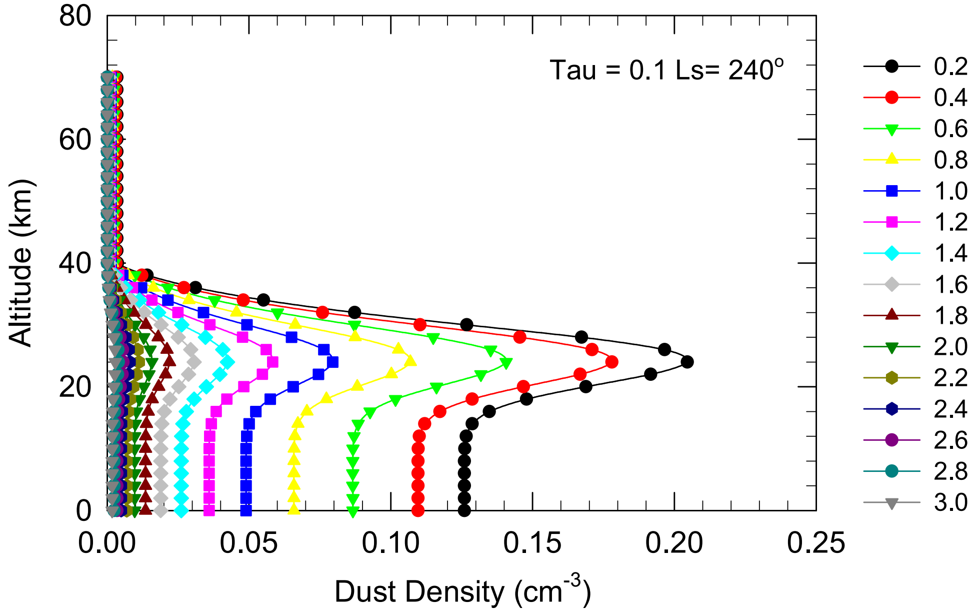


**Figure 3.2 Estimated dust profiles for MY 28 during pre-storm/clear condition at Ls = 240°. Different colour shows different particle sizes.**

The figure 3.3 shows the dust density profiles during the peak-storm condition. This condition prevails on Mars at global dust storm. This indicates that the dust is lifted to high altitudes creating a layer in the lower atmosphere of Mars. The concentration of the 0.2 micron is maximum and the 3.0 is the least. The 0.2 micron particle creates a layer at ~ 45 km with peak density at 3.0 cm$^{-3}$. It is also to be noted that the distinct peak can be clearly seen up to particles of size of 3.0 micron. The dusts of particles of higher sizes than 2.4 micron are less comparatively. This is a clear indication that few larger dust particles are lifted during high dust conditions. The geophysical parameter such as wind is also strong, lifting particles of every size in the atmosphere. During Ls = 280°, the optical depth was the maximum (1.27) and thus the estimated dust profiles are the highest compared to the any other seasons. It is evident that the dust particles rise from surface to high altitude ~ 45 km and above that their concentration decreases rapidly. The winds are stronger at higher altitudes but the gravitational setting is dominating force leading to fall of the particles. The significant peak densities of different particles are as follows: 0.4 micron peak density is 2.5 $cm^{-3}$, 0.6 micron peak density is 2.0 $cm^{-3}$, 1.0 micron peak density is 1.0 $cm^{-3}$, 1.4 micron peak density is 0.65 $cm^{-3}$, and 2.0 micron peak density is 0.02 $cm^{-3}$.

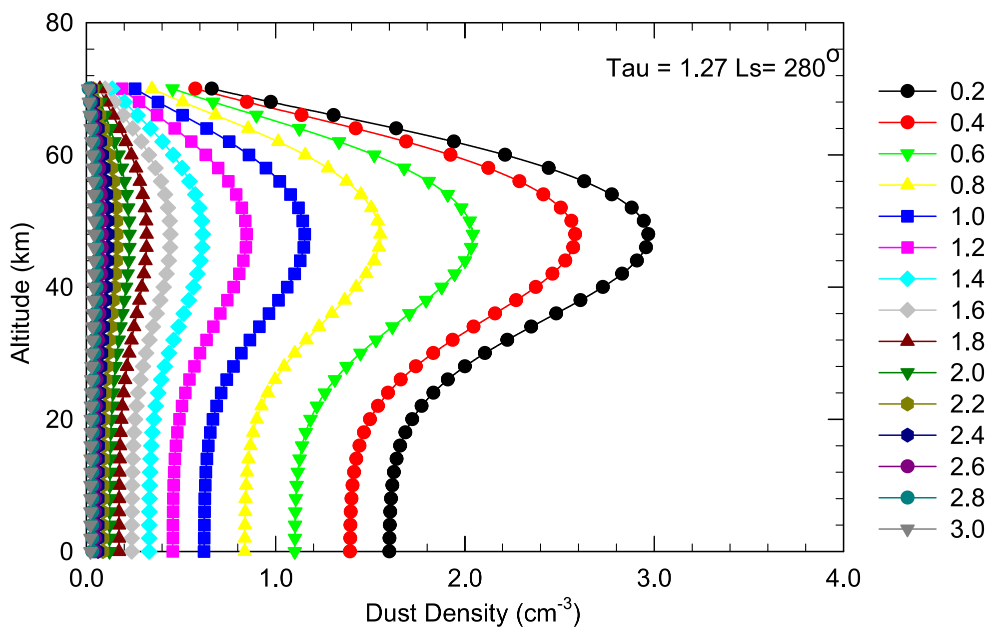


**Figure 3.3 Estimated dust profiles for MY 28 during peak dust storm condition at Ls =280°. Different colour shows different particle sizes.**

Figure 3.4 shows the dust density profiles during the medium dust storm. These conditions prevail on Mars at global dust storm when the peak storm starts declining. This indicates that the dust is lifted to high altitudes starts to settle down. The concentration of the 0.2 micron is maximum and the 3.0 is the least. The 0.2 micron particle creates a layer at ~35 km with peak density at 0.8 $cm^{-3}$. It is to be noted that the distinct peak height of all particles were reduced. The dust particles of higher than 2.2 micron are less comparatively at Ls = 270°. The geophysical parameter such as wind is also medium, thus lifting of particles also reduces. During

Ls = 300$^o$, the optical depth was ~ 0.5 and thus estimated dust profiles are higher than the normal condition while lesser than compared to the any peak dust storm seasons. It is evident that peak altitude of dust particles of all sizes reduces ~ 30 km and above that their concentration decreases rapidly. The significant peak densities of different particles are as follows: 0.4 micron peak density is 0.68 $cm^{-3}$, 0.6 micron peak density is 0.51 $cm^{-3}$, 1.0 micron peak density is 0.3 $cm^{-3}$, The 1.4 micron peak density is 0.18 $cm^{-3}$, and 2.0 micron peak density is 0.02 $cm^{-3}$.

Figure 3.5 shows nearly same dust density profiles as they were obtained during the pre-storm condition. This indicates that the dust is settled down after few days or weeks after the global dust storm, yet some dust stay suspended in the lower atmosphere of Mars. The concentration of the 0.2 micron reduces to 0.21 $cm^{-3}$. The distinct peak can be clearly seen up to particles 1.6 micron. The dust particles of size higher than 2.0 micron were settled very fast and hence their density reduces considerably. The winds are found unable to lift such large particles in the atmosphere after the dust storm season. At Ls = 320$^o$ the optical depth was the least (0.1) and thus estimated dust profiles are least compared to the other seasons.

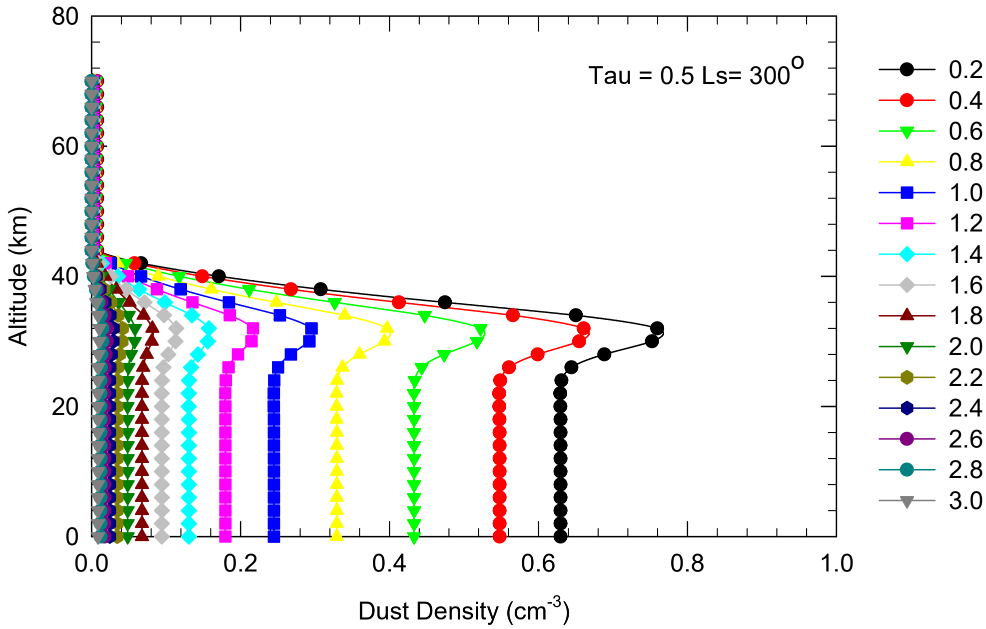


**Figure 3.4 Estimated dust profiles for MY 28 during post-storm/medium condition at Ls =300º. Different colour shows different particle sizes.**

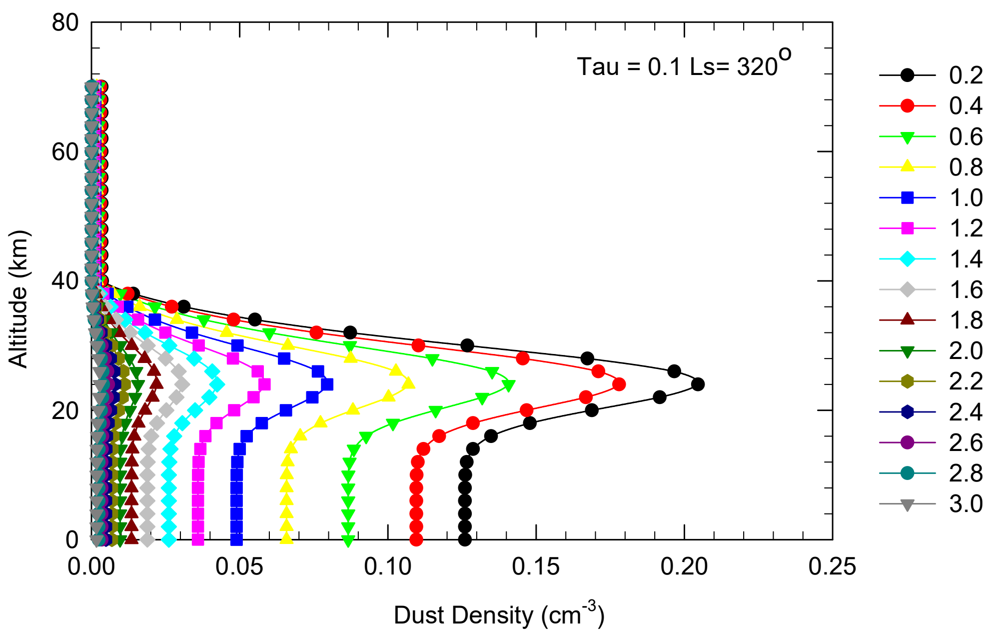


**Figure 3.5 Estimated dust profiles for MY 28 during normal/clear condition at Ls =320º. Different colour shows different particle sizes.**

## 3.2 OBSERVATIONS OF DUST OPACITY PROFILES

The global dust storm is also observed in MY 28 by PFS instrument onboard MEX. In this section we compare our model results of dust density profiles with the observations carried out from MCS, CRISM and PFS instruments in the lower atmosphere of Mars. Recently, Heavens et al. (2011), Guzewich et al. (2014), and Wolkenberg et al. (2017) retrieved vertical profiles of dust mixing ratios from MCS, CRISM and PFS observations respectively. They have observed two broad peaks at about ~ 40 km and ~ 25 km in the dust mixing ratio profiles in southern summer at low latitudes (0-30°S). Mostly single peak is observed in MCS, CRISM and PFS observations. Sometimes two peaks are observed simultaneously. Guzewich et al. (2014) noted that the highest peak in the dust opacity is formed mainly due to small particles of size of ~ 1.0 micron while the lower peak is formed due to large particles of size ~ 3.0 micron. We can compare peak dust opacities of these measurements with our model calculations. There has been found reasonably good agreement between calculations and measurements as far as the position of the peaks are concerned. We have estimated dust opacity profiles at different sizes of the particles from 0.2 to 3.0 micron.

The figure 3.6 shows variations of dust optical depths with Ls in MY 28 at latitude range 0-10°S, 10°-20°S and 20°-30°S. These optical depths are taken in the calculations of corresponding dust opacity profiles. In figures 3.2-3.5 the dust opacity profiles are plotted at 10°-20°S only because the dust opacities at latitudes 0°-10°S and 20°-30°S are nearly same as estimated for latitude range 10°-20°S. As can be seen in figure 3.6 the dust opacity increases up to 1.2 from 0.3 (i.e. by a factor of four) during the peak dust storm time at Ls = 280°. Before and after the dust storm peak, opacities are lowest equal to ~ 0.1. In figures 3.1 and 3.6 the dust density is plotted over the surface of Mars. It should be noted that the dust storm is changing with time and location. In presence of dust storm, Mars becomes cool and surface temperature decreases by ~ 25°K because the solar radiation cannot reach on the surface (Sheel and Haider, 2016).

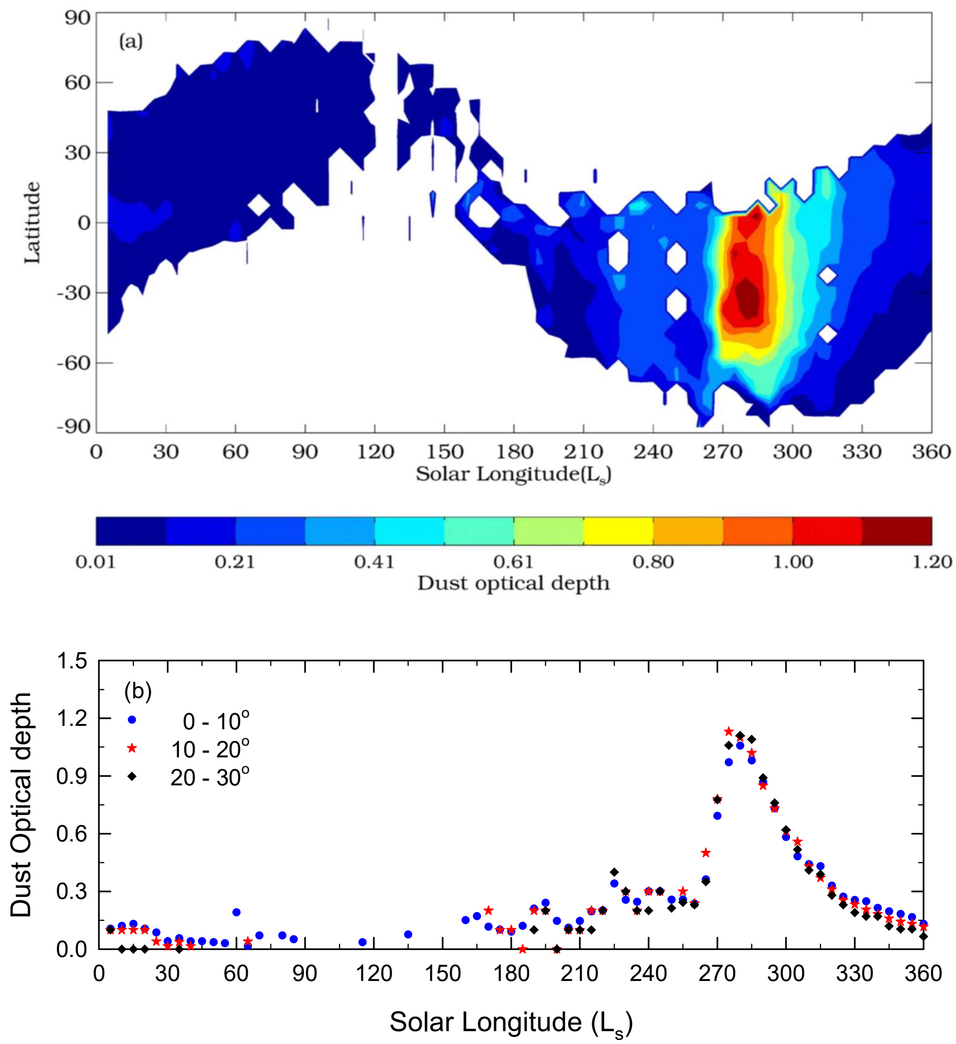


**Figure 3.6 Dust optical depths varying with season in MY28 at latitude range 0°-10°S, 10°-20°S and 20°-30°S**

### 3.2.1 Dust Mixing Ratio Profiles from MCS Observations

The vertical distribution of dust mixing ratios in the Martian atmosphere is poorly understood. Heavens et al. (2011) investigated vertical profiles of dust mixing ratios retrieved from limb observations of MCS onboard MRO during summer of 2006-2007 (Ls=111°-177° in MY28) and spring of 2007-2008 (Ls=0°-180° in MY29). In most of the northern spring and southern summer the dust mixing ratios in the tropics are maximum at ~ 25 km above the surface. Later Guzewich et al. (2014) observed several profiles of dust mixing ratios in the troposphere of Mars. They have observed two strong dust layers in most of the profiles at about ~ 40 km and ~ 25 km due to heating of different particle sizes in the Martian atmosphere. The high and low altitude layers are formed by different particle sizes of effective radius ~ 1.0 µm and > 3 micron respectively (Guzewich et al., 2014). It should be noted that water ice clouds have been observed with a near-uniform particle size with an effective radius of approximately 1.5 micron throughout the atmospheric column (Wolff et al., 2009). The dust mass mixing ratio profile with two distinct peaks as a function of altitude observed by MCS is shown in figure 3.7 (Heavens et al., 2014).

Recently Montabone et al. (2019) studied column dust optical depth for MY34 (May5, 2017-March 23, 2019) using observations by MCS onboard MRO. They have reported diurnal, seasonal and day night variability of dust in atmospheric column, which is very intense during the MY 34 equinoctial global dust event. They have also simulated these measurements by Mars climate model, which showed that this variability may be partly explained by the large scale circulation.

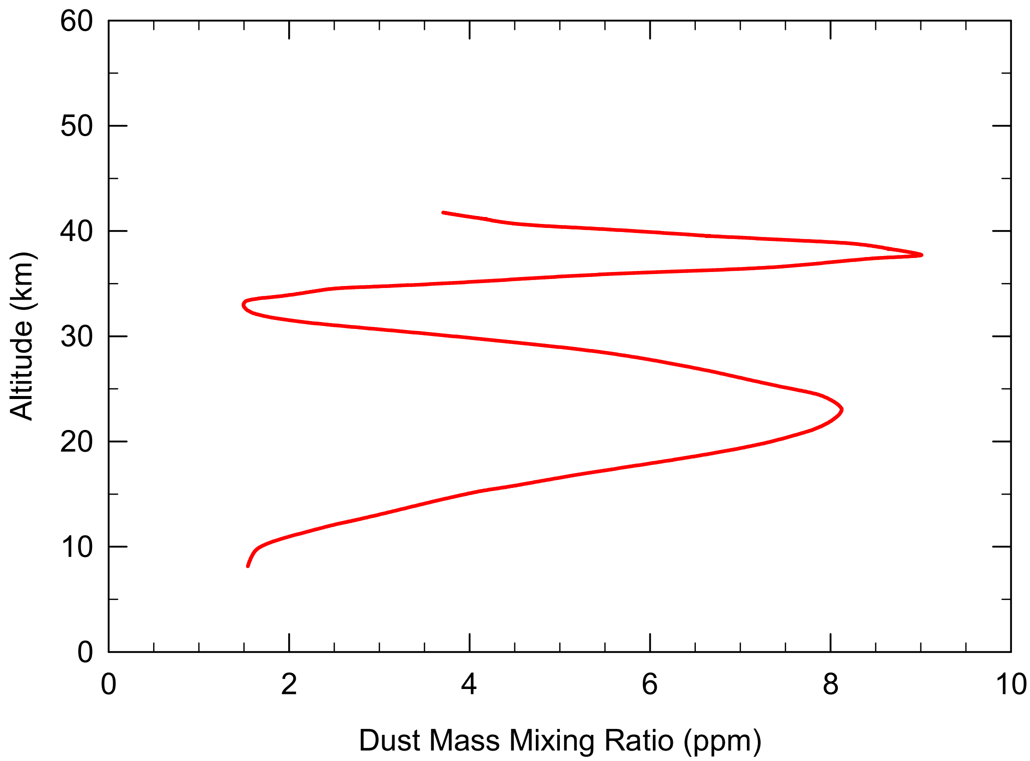


**Figure 3.7 the altitude profiles of dust mass mixing ratio as observed by MCS (Heavens et al., 2014)**

### 3.2.2 Dust Mixing Ratio Profiles from CRISM Observations

The figure 3.8 represents the altitude profile of dust mixing ratio as observed by CRISM onboard MRO (Guzewich et al., 2014). The CRISM has also observed two distinct peaks in the altitude profiles of dust mixing ratios as observed by MCS (Heavens et al., 2014; Sheel and Haider, 2016). As noted above the two peaks are not formed always in the dust mixing ratio profiles. The positions of these peaks are changing with seasons and locations. The peak values depend on the dust optical depth. During the dust storm period the peak dust opacity and peak dust mixing ratios are larger than that observed in absence of dust storm. The particles of smaller size can form a dust cloud at high altitude in comparison to that produced by the particles of the larger size. We have plotted estimated dust density profiles in figures 3.2 to 3.5 at optical depths 0.1, 1.27, 0.5, and 0.1 respectively for different particle sizes from 0.2 to 3.0 micron (Haider et al., 2015; Sheel and Haider, 2016). In these figures the dust density is increasing with increasing the optical depths. The density of dust is large for small size particles as observed by MCS and CRISM instruments onboard MRO. Sheel and Haider (2016) have also calculated the dust density profiles in MY 28 when a major dust storm occurred at southern low latitude (0-30°S) during late spring to summer. The density of dusts and their optical depths are changing with season. Thus, the density of dust is changing with season, location and optical depths in presence and absence of dust storm. We report that the dust density profiles represent a single or double dust layers always in the lower atmosphere of Mars.

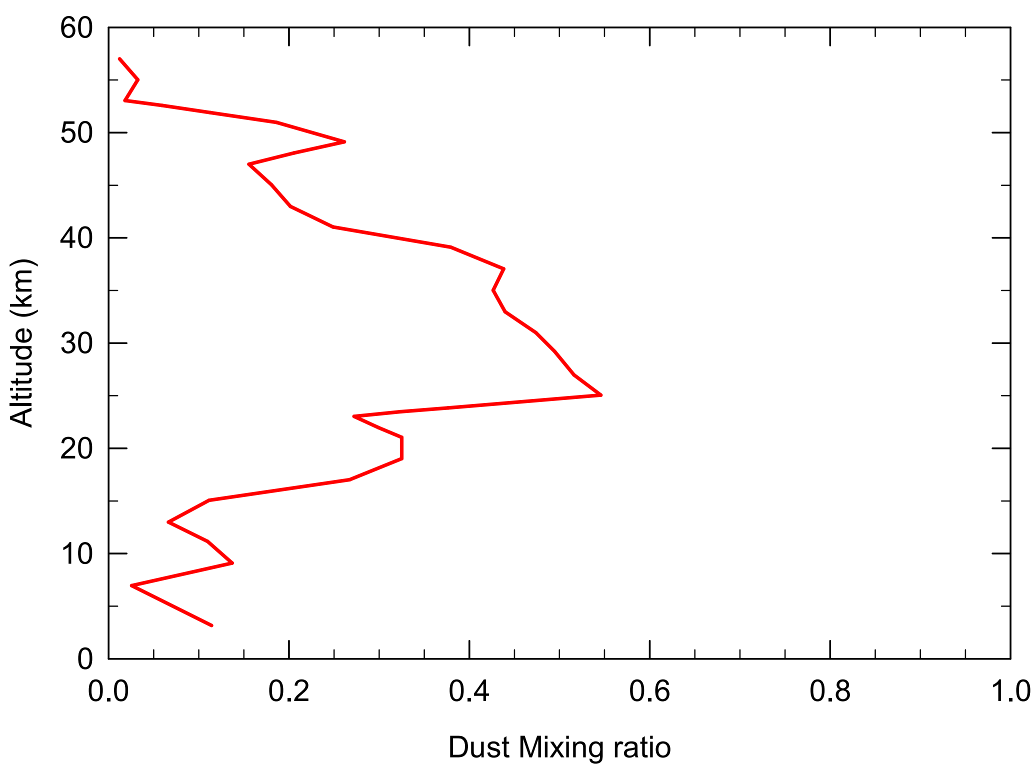


**Figure 3.8 The altitude profiles of dust mass mixing ratio as observed by CRISM onboard MRO (Guzewich et al., 2014)**

### 3.2.3 Dust Opacity Profiles from PFS Observations

Wolkenberg et al. (2017) have described the spatial and temporal distributions of dust on Mars from L=331$^{o}$ in MY 26 until Ls = 80$^{o}$ in MY 33 retrieved from the measurements taken by the PFS instrument in agreement with the previous observations carried out by MCS and CRISM instruments. They found large dust opacity mostly in southern region of higher terrain during the summer. The dust opacities obtained from PFS and TES are compared by them. They found good consistency between observations of these two instruments during overlapping interval (Ls=331$^{o}$ in MY26 until Ls=77$^{o}$ in MY27). They have also obtained two dust layers from PFS observations as observed by MCS and CRISM instruments. The first and second layers of the dust were observed due to heating in the atmosphere of Mars during the dust storm corresponding to two different particle sizes (Wolkenberg et al., 2018). In figure 3.8 the altitude profiles of dust opacity obtained from PFS instrument is plotted for four orbits (# 4328, 4428, 4471 and 4510) of MEX in MY28 and MY29. In this figure top peak occurred at about 50 km in MY28 while the lower peak is observed at about 25 km in MY29. The PFS orbit # 4328, 4428, 4471 and 4510 carried out measurements at Ls = 241$^{o}$, 259$^{o}$, 266$^{o}$ and 273$^{o}$ respectively. MCS dust profiles are used to normalize PFS dust opacity. The PFS dust opacity are averaged between latitude range 30$^{o}$S to 30$^{o}$N at Ls = 280$^{o}$ in MY28. In MY29 PFS dust opacity are averaged between latitude range 25$^{o}$S to 45$^{o}$S at Ls = 240$^{o}$ to 275$^{o}$ due to observational constraints (Wolkenberg et al., 2018).

In figure 3.1 we have not plotted optical depth of recent global dust storm that has been observed by the Opportunity Mars Exploration Rover (MER) and the MRO in June 2018 (MY34: https://mars.nasa.gov/resources/21917/atmospheric-opacity-from-opportunitys-point-of-view). The previous dust storms that occurred in MY 10, MY 13, MY 25, and MY 28 were slower to build in comparison to the new dust storm of MY 34. The new dust storm observed maximum UV dust opacity $\tau = 8.5$ on June 2018 at about Ls = 190° and spread quickly all over the globe (Guzewich et al., 2019). Guzewich et al. (2019) noted ~ 97% reduction in incident solar radiation on the surface of Mars during this dust storm event. This dust storm reduced about 30 K temperature in the Mars' atmosphere.

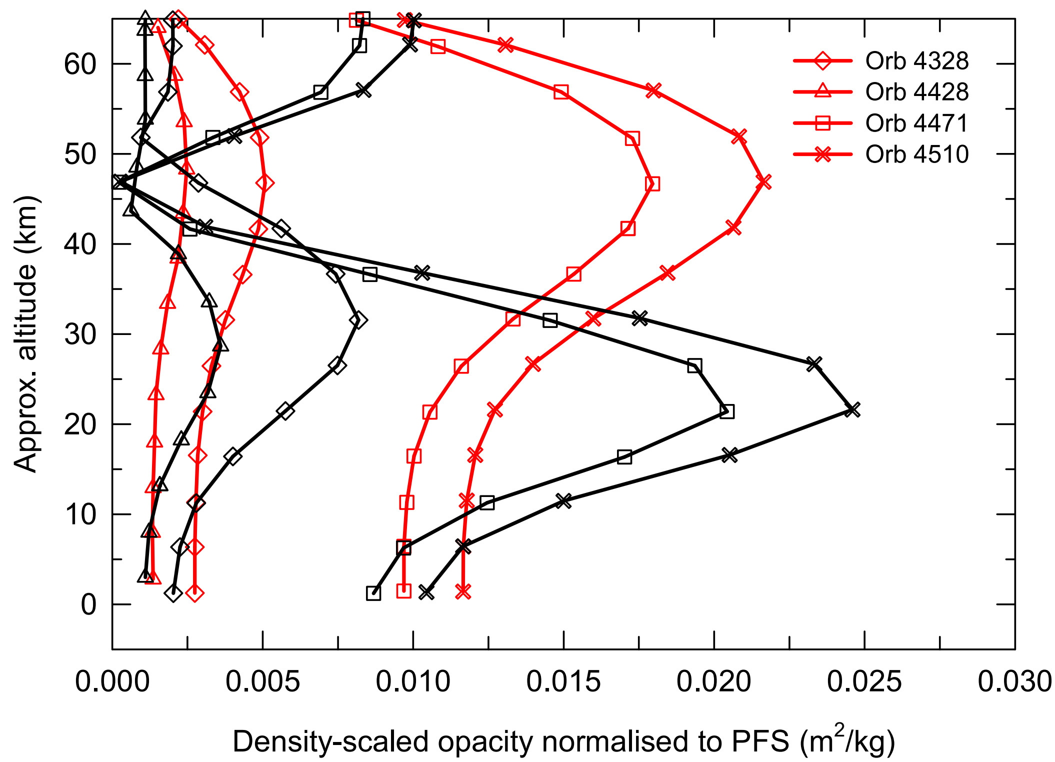


**Figure 3.9. The altitude profiles of dust opacity as observed by PFS onboard MEX in MY28 and MY29 (Wolkenberg et al., 2018) for four orbits of the spacecraft. The red colour shows PFS measurements of dust opacity in MY28 while black colour represents PFS measurements of dust opacity in MY29.**

❒❒❒

# REFERENCES

Bougher, S. W., Pawlowski, D., Bell, J. M., Nelli, S., McDunn, T., Murphy, J. R., et al. (2015). Mars Global Ionosphere-Thermosphere Model: Solar cycle, seasonal, and diurnal variations of the Mars upper atmosphere. Journal of Geophysical Research: Planets, **120**(2), 311-342.

Fenton, L. K., Pearl, J. C., and Martin, T. Z. (1997). Mapping Mariner 9 dust opacities. Icarus, **130**(1), 115-124.

Forget, F., and Montabone, L. (2017). Atmospheric dust on Mars: A review. 47th International Conference on Environmental Systems.

Guzewich, S. D., Lemmon, M., Smith, C. L., Martínez, G., de Vicente-Retortillo, Á., Newman, C. E., et al. (2019). Mars science laboratory observations of the 2018/mars year 34 global dust storm. Geophysical Research Letters, **46**(1), 71-79.

Guzewich, S. D., Smith, M. D., and Wolff, M. J. (2014). The vertical distribution of Martian aerosol particle size. Journal of Geophysical Research: Planets, **119**(12), 2694-2708.

Haider, S. A., Batista, I. S., Abdu, M. A., Muralikrishna, P., Shah, S. Y., and Kuroda, T. (2015). Dust storm and electron density in the equatorial D region ionosphere of Mars: Comparison with Earth's ionosphere from rocket measurements in Brazil. Journal of Geophysical Research: Space Physics, **120**(10), 8968-8977.

Heavens, N. G., Johnson, M. S., Abdou, W. A., Kass, D. M., Kleinböhl, A., McCleese, D. J., et al. (2014). Seasonal and diurnal variability of detached dust layers in the tropical Martian atmosphere. Journal of Geophysical Research: Planets, **119**(8), 1748-1774.

Heavens, N. G., Richardson, M. I., Kleinböhl, A., Kass, D. M., McCleese, D. J., Abdou, W., et al. (2011). Vertical distribution of dust in the Martian atmosphere during northern spring and summer: High-altitude tropical dust maximum at northern summer solstice. Journal of Geophysical Research: Planets, **116**(E1).

Liu, G., England, S. L., Lillis, R. J., Withers, P., Mahaffy, P. R., Rowland, D. E., et al. (2018). Thermospheric expansion associated with dust increase in the lower atmosphere on Mars observed by MAVEN/NGIMS. Geophysical Research Letters, **45**(7), 2901-2910.

Montabone, L., Spiga, A., Kass, D. M., Kleinböhl, A., Forget, F., and Millour, E. (2019). Martian Year 34 Column Dust Climatology from Mars Climate Sounder Observations: Reconstructed Maps and Model Simulations. arXiv preprint arXiv:1907.08187.

Sheel, V., and Haider, S. A. (2016). Long-term variability of dust optical depths on Mars during MY24-MY32 and their impact on subtropical lower ionosphere: Climatology, modeling, and observations. Journal of Geophysical Research: Space Physics, **121**(8), 8038-8054.

Wolff, M. J., Smith, M. D., Clancy, R. T., Arvidson, R., Kahre, M., Seelos, F., et al. (2009). Wavelength dependence of dust aerosol single scattering albedo as observed by the Compact Reconnaissance Imaging Spectrometer. Journal of Geophysical Research: Planets, **114**(E2).

Wolkenberg, P., Giuranna, M., Grassi, D., Aronica, A., Aoki, S., Scaccabarozzi, D., and Saggin, B. (2018). Characterization of dust activity on Mars from MY27 to MY32 by PFS-MEX observations. Icarus, **310**, 32-47.

❒❒❒

# CHAPTER - 4

# RESPONSE OF DUST ON THERMAL EMISSION SPECTRA OBSERVED BY PLANETARY FOURIER SPECTROMETER

# CONTENTS

*The thermal emission spectra have provided many useful insights about the Martian atmosphere and surface. The interpretation of the thermal emission spectra can give us information about atmospheric temperature, pressure, mineralogy and presence of atmospheric constituents including their isotopes. In the present chapter, we have analysed the thermal emission data obtained in MY 28 from PFS onboard MEX in presence and absence of dust storm. We have developed a radiative transfer model for dusty atmosphere of Mars. This model is used to reproduce thermal emission spectra in presence (Ls = $280^o$ and $300^o$) and absence (Ls = $240^o$ and $320^o$) of the dust storm at latitude range $0^o$-$10^o$S, $10^o$-$20^o$S and $20^o$-$30^o$S. The estimated results are compared with thermal emission measurements made by PFS between wave numbers 250-1400 $cm^{-1}$. We have also retrieved brightness temperatures from thermal emission spectra by inverting the Planck function. There is a good agreement between estimated and measured thermal emission spectra. The model reproduces the observed features at wave numbers 600-750 $cm^{-1}$ and 900-1200 $cm^{-1}$ due to absorptions by $CO_2$ and dust respectively. The maximum brightness temperature ~280 K is measured at Ls = $240^o$ when Mars received a large amount of solar radiation at perihelion. The minimum brightness temperature ~ $220^o$ K is observed at Ls = $320^o$ in the absence of dust storm. In presence of dust storm thermal emission spectra and brightness temperatures are reduced by factors of ~ 2.0 between wave numbers 900-1200 $cm^{-1}$ in comparison to that observed in absence of dust storm.*

# 4.1 INTRODUCTION

The infrared spectroscopy is an important remote sensing technique to study the planetary atmospheres and surfaces. Over several decades this technique has been used on Mars to study the composition of the surface, minerals, dust, water ice clouds, temperature and atmospheric gases (Hanel et al., 1972; Kieffer et al., 1977; Christensen et al., 2001). The atmosphere of Mars consists several $CO_2$ bands, weak water vapour lines, radiatively active water ice clouds, and signatures of dust periodically stirred up by strong surface winds. The surface of Mars can be observed in certain spectral windows: 780-1000 $cm^{-1}$, 1080-1240 $cm^{-1}$ and 2500-2800 $cm^{-1}$. The Mariner 9, Viking, MGS, Mars Odyssey and Mars Express have observed the presence of water and dust on the surface of Mars from infrared thermal emission spectrometer (Hanel et al., 1972; Kieffer et al., 1977; Christensen et al., 2001). These missions have also observed surface minerals, rocks and temperatures on Mars. A global dust storm in MY 28 was reported by previous workers (Wolkenberg et al., 2011; Kass et al., 2016; Wolkenberg et al., 2018). Studies have revealed that the dust storm can affect the whole Martian atmosphere. It can cause heating of the lower atmosphere, can reduce the hydrated cluster ions and the electrical conductivity in the ionosphere (Sheel and Haider, 2016), and causes enhancement of water content thereby increasing hydrogen escape flux (Forget and Montabone, 2017). Recently, an improved climatology dataset derived from PFS has been released (Giuranna et al., 2018). The Martian dust compositions, vertical distribution, diurnal and seasonal variations require comprehensive modeling. In this chapter we have analysed PFS data obtained from MEX during the dust storm period in MY28. The modeling of thermal emission spectra observed by PFS is carried out between wave numbers 250-1400 $cm^{-1}$.

### 4.1.1 PFS Observations

The MEX carried out PFS instrument for the measurement of thermal emission spectra emitted by the surface/atmosphere of Mars. This instrument has a short-wavelength (SW) channel covering the spectral range 1700-8200 $cm^{-1}$ (1.2-5.5 μm) and long-wavelength (LW) channel covering 250-1700 $cm^{-1}$ (5.5-45 μm) (Giuranna et al., 2005; Fouchet et al., 2008; Wolkenberg et al., 2011). In SW channel of PFS spectra, methane was first discovered by Formisano et al. (2005) at wave number 3018 $cm^{-1}$. They have reported global average of methane mixing ratio to be 10 ± 5 ppbv. Later Geminale et al. (2008, 2011) studied the seasonal, diurnal and spatial variations of methane in the atmosphere of Mars. Recently Sindoni et al. (2011) have observed mixing ratios of water vapour and carbon monoxide at wave numbers 3845 $cm^{-1}$ (2.6 μm) and 4235 $cm^{-1}$ (2.36 μm) respectively. They have found anti-correlation between the concentrations of water vapour and CO. This is due to sublimation of the carbon dioxide and water vapour from north polar ice cap, which decreases concentration of non-condensable species CO. Similar process also occurs in south polar cap but in this case the condensation of carbon dioxide and water vapour increases the concentration of non-condensable species CO.

Fouchet et al. (2008) used PFS data of LW channel to study the seasonal and geographical variations of water vapour for MY 26 and MY 27. They observed two maxima in the geographical distributions of water vapour over Tharsis and Arabia regions. Giuranna et al. (2008) studied the mechanisms of $CO_2$ condensation and accumulation over south polar cap of Mars. They found that the polar cap expands symmetrically with a constant speed during the fall season. Zasova et al. (2008) suggested that the atmospheric dust has a significant impact on radiative heating. Later Mättänen et al. (2009) analysed PFS data to study the response of local dust storm on atmospheric thermal structure near the equator of Mars in the late northern summer. They reported that the temperatures were about ~ 10 K colder near the surface and ~ 5 K warmer in the upper atmosphere during the dust storm period. Sato et al. (2011) investigated tidal variations in the atmospheric temperature at low altitude (< 45 km) during the dust-clear period from PFS data. Montabone et al. (2015) analysed the data obtained from MGS and Mars Odyssey for MY24 to MY32 and studied the inter-annual and seasonal variability of dust optical depths**.** Aoki et al. (2015) have reported $H_2O_2$ in the Martian atmosphere at wave number 379 $cm^{-1}$. They have derived mixing ratios 16 ± 19 ppb at Ls = $0^o$-$120^o$, 35 ± 32 ppb at Ls = $120^o$-$240^o$ and 41 ± 28ppb at Ls = $240^o$-$360^o$.

## 4.1.2 PFS Data Analysis

We have analysed PFS data of LW channel for MY28 when a major dust storm occurred at low latitude in southern hemisphere between Ls = 260°-300° for about a couple of weeks. The thermal emission spectra and brightness temperature are retrieved from these observations in absence and presence of dust storm. We have considered that the thermal emission emitted from the surface of Mars in the infrared wavelength **v**, under local thermal equilibrium conditions is characterized by Planck function (Haus and Titov, 2000) **B** and it is expressed as:

$$B(T)=\frac{2hc^2v^3}{\left\{e^{\frac{hcv}{kT}}-1\right\}} \tag{4.1}$$

where v is the wavenumber and **T** is temperature, **h** is Planck constant ($6.62\times10^{-34}$ J.s), **k** is Boltzmann constant ($1.38\times10^{-34}$ $JK^{-1}$), and **c** is speed of light ($3.0\times10^{8}$ $ms^{-1}$). The altitude dependent brightness temperatures (Haus and Titov, 2000) are calculated by inverting above equation:

$$T_B=\frac{hcv}{k\ln\left(\frac{2hc^2v^3}{B_T+1}\right)} \tag{4.2}$$

The radiative transfer equation describes that the radiation is affected through the Martian atmosphere. The emission, absorption and scattering processes are considered in the radiative transfer equation (Ignatiev et al., 2005). Thermal emission is characterized by the Planck function **B**. In chapter 2 we have described Planck function and radiative transfer method in detail. The modeled results are presented in this chapter. The description of the PFS data processing is shown in the figure 4.1

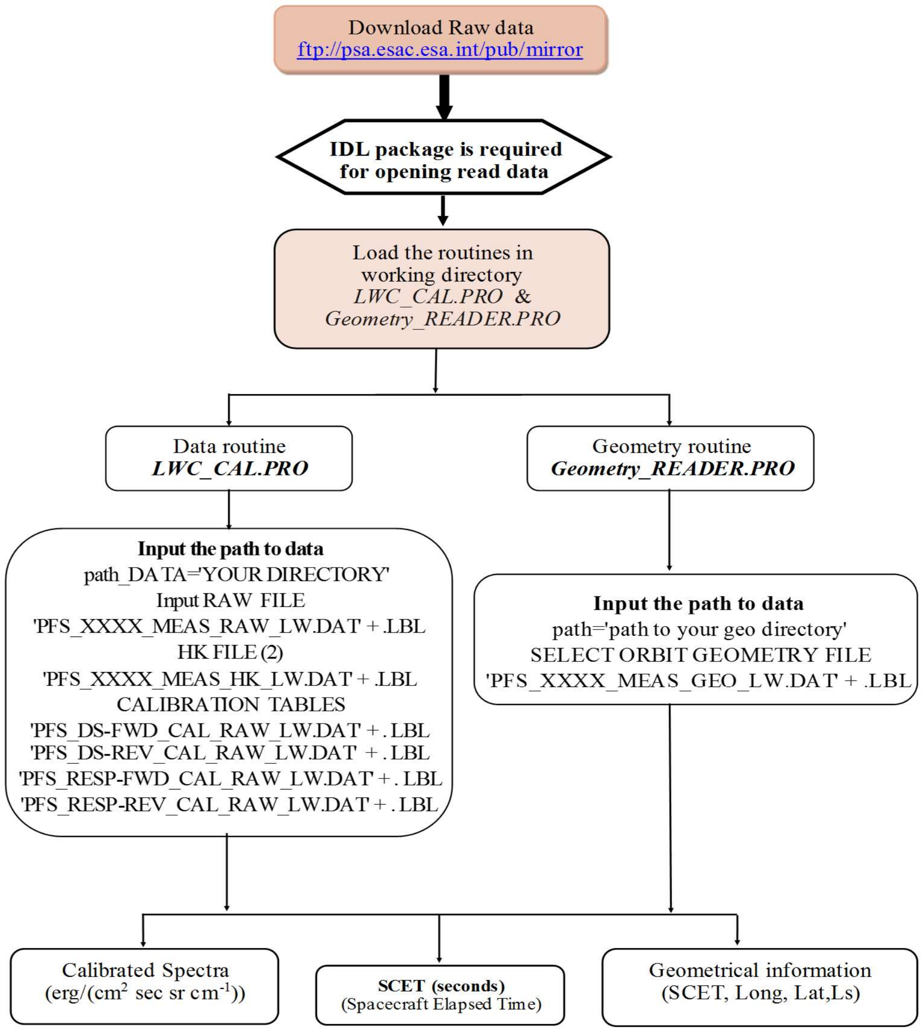


**Figure 4.1: Schematic diagram for processing of raw data of PFS measurements and spacecraft geometry using IDL package and other data/geometry routines.**

We have used the IDL routines provided by the ESA, to process the raw data files. The routine "LWC_CAL.PRO" and Geometry_READER.PRO reads raw data of PFS instrument and the spacecraft geometry respectively. We select LWC_CAL.PRO routine. This routine processes the raw data along with two HK files and corresponding six LABEL files. Later we select the path DATA directory Geometry_READER.PRO and give orbit number 'XXXX'. We run this routine, which outputs radiance spectra versus wave numbers at SpaceCraft Elapsed Time (SCET) for each selected ORBIT. The orbit's geometry of MEX spacecraft can be known by processing GEO files of the orbit. This routine provides the SpaceCraft Elapsed Time (SCET) and geometry information (MY, Ls, Latitude, and Longitude etc).

Like other instruments, PFS instrument also observed instrumental error while measuring thermal emission spectra. This error depends upon the measurement conditions and mechanical and non-mechanical vibration of the spacecraft (Formisano et al., 2005). Comolli and Saggin (2010) showed that the uncertainties can be reduced by the averaging of the spectra, which has been performed in the present study. Giuranna et al. (2005) reported about 1-σ error less than 1% in PFS measurements. These PFS data are averaged over 10 degree latitudes between $0^o$ to $30^o$S to decrease the instrumental noise (Comolli and Saggin, 2010). The radiative transfer modelling of these measurements are carried out at Ls = $240^o$, $280^o$, $300^o$ and $320^o$ due to absorptions of $CO_2$, $H_2O$ and dusts in southern hemisphere at low latitudes. Our calculated brightness temperature and thermal emission spectra matches well with the observations made by PFS instrument between wave number 250-1400 $cm^{-1}$.

# 4.2 MEX ORBIT COVERAGE AT LOW LATITUDE

The figure 4.2 represents the track coverage of MEX in MY28 when PFS observed thermal emission spectrum in four orbits at Ls = $240^o$, $280^o$, $300^o$, and $320^o$. We have selected these orbits where MEX passed through southern low latitude region (0-$30^o$S) at fixed longitude of Mars. This figure shows that spacecraft longitudes are not changing with latitude in the tropical low latitude region.

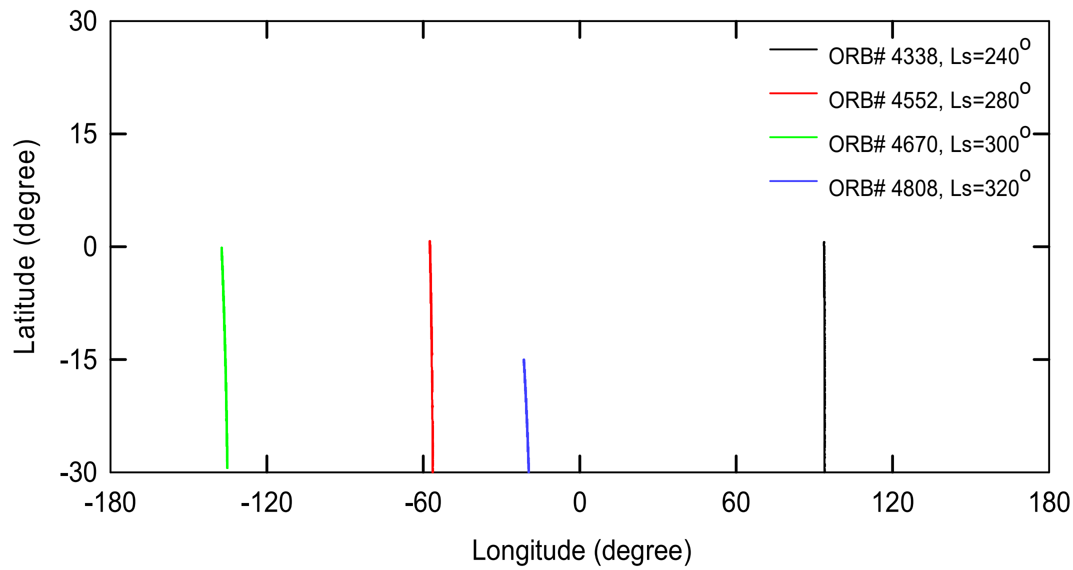


**Figure 4.2 Geographical distribution of PFS measurements carried out from MEX for Ls=240°, 280°, 300° and 320° during orbit # 4338, 4552, 4670 and 4808 respectively.**

## 4.2.1 Temperature Profiles at Low Latitude

We have estimated temperature profiles and thermal emission spectra for these four orbits corresponding to Ls = 240°, 280°, 300°, and 320° at low latitude range 0-10°S, 10°-20°S and 20°-30°S in MY28. The figures 4.3a, 4.3b, 4.3c, and 4.3d represent temperature profiles estimated by Mars Climate Datasets (MCD) v5.2 using $CO_2$ 15 μm band for Ls = 240°, 280°, 300°, and 320° respectively at low latitudes. These temperature profiles are estimated between 0 km and 70 km. Wolkenberg et al. (2011) retrieved atmospheric temperature between 5 km and 25 km at same Ls and same latitudes from PFS observations using $CO_2$ 15 μm band. The observed temperatures are also plotted in figures 4.3a-4.3d and compared with the estimated temperature profiles. There is a reasonable agreement between two temperature profiles above 5 km as far as the exponential behavior is concerned. The atmospheric temperature is not measured at the surface of Mars. The temperature estimated by MCD v5.2 increases maximum up to 240-250 K near the surface. The observed temperature is higher than the estimated temperature by 5-10 K up to ≤ 10 km altitude during the dust storm period. In the decline period of the dust storm, observed temperature is decreasing by ~ 5 K from the estimated temperature. The estimated temperature is not increasing during the dust storm period because the MCD model is not developed for the dust storm condition. The observed temperature is high by 5-10 K during the dust storm period at low latitudes ($0^o$-$30^o$S) up to 10 km altitude.

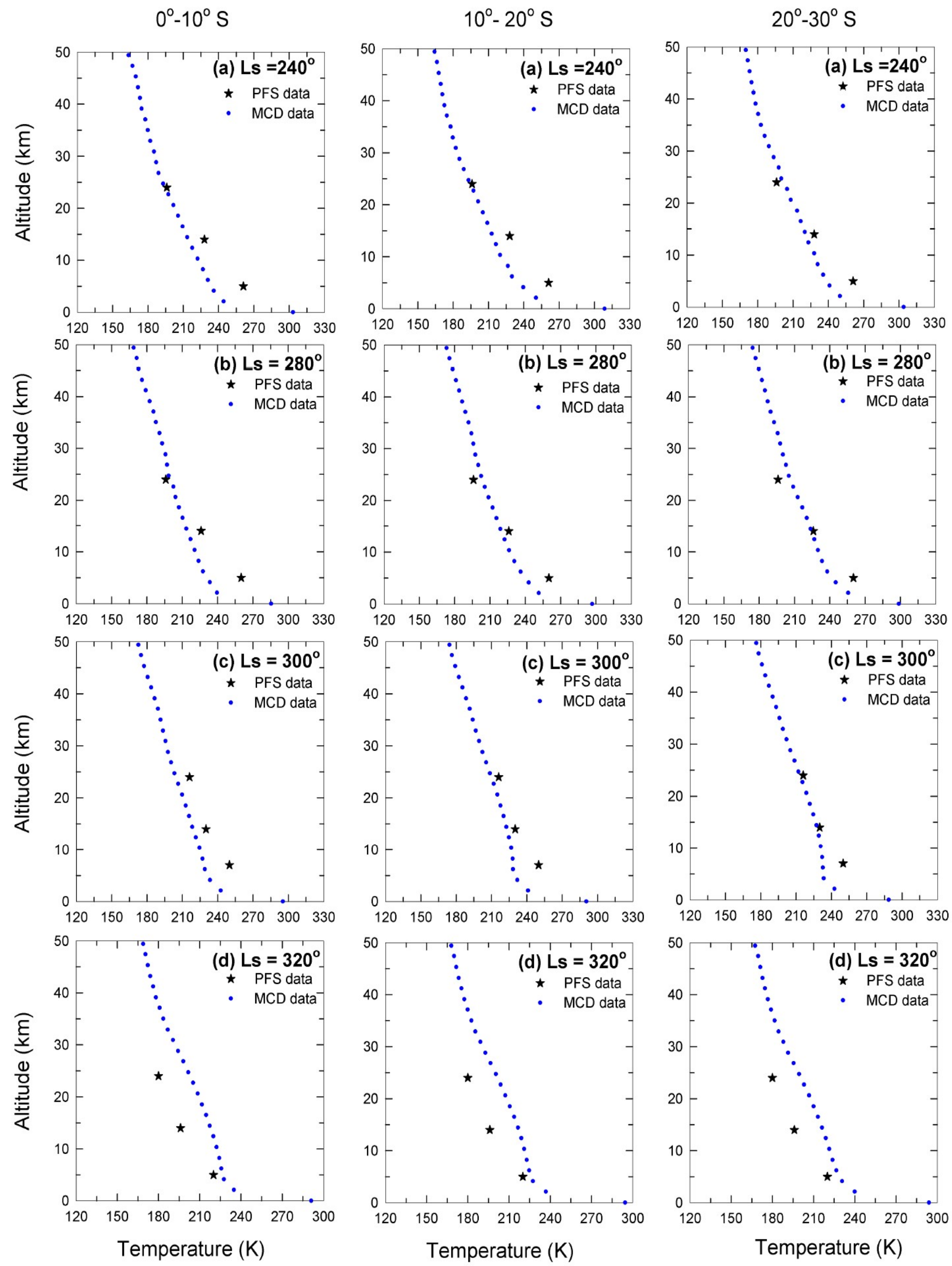


**Figure 4.3 Comparison of temperature profiles between MCD and PFS observations at low latitudes 0-10°S, 10-20°S, 20-30°S for (a) Ls=240°, (b) Ls= 280°, (c) Ls=300° and (d) Ls=320°.**

## 4.2.2 Observed Thermal Emission Spectra

The Figure 4.4a-c represents the thermal emission measurements carried out by PFS between wave numbers 250-1400 $cm^{-1}$ at latitude range $0^o$-$10^o$S, $10^o$-$20^o$S and $20^o$-$30^o$S respectively. These spectra were observed in MY28 at Ls = $240^o$, $280^o$, $300^o$ and $320^o$ corresponding to orbit # 4338, 4552, 4670 and 4808 respectively (The emission spectra is not observed at Ls=$320^o$ between latitude range $0^o$ -$10^o$S). We have averaged 23, 19, and 19 spectrum for latitude range $0^o$-$10^o$S, $10^o$-$20^o$S, and $20^o$-$30^o$S respectively corresponding to orbit # 4338 at Ls = $240^o$. The 17, 25, and 20 spectra are averaged for latitude range $0^o$-$10^o$S, $10^o$-$20^o$S and $20^o$-$30^o$S respectively corresponding to orbit # 4552 at Ls = $280^o$. For orbit # 4670 we have averaged 24, 23, and 26 spectra for latitude range $0^o$-$10^o$S, $10^o$-$20^o$S and $20^o$-$30^o$S respectively at Ls = $300^o$. Finally, 18 and 15 emission spectra were averaged for latitude range $10^o$-$20^o$S and $20^o$-$30^o$S respectively corresponding to orbit # 4808 at Ls = $320^o$. In these spectra prominent dip at about 667 $cm^{-1}$ is observed due to absorption of $CO_2$. The broad peak at about 300-400 $cm^{-1}$ is observed due to absorption of $H_2O$. The emission intensity is decreased by factor of ~ 2 due to absorption of dust between wave number 900-1200 $cm^{-1}$ in presence of dust storm. The absorption of dust is maximum during peak dust storm period at latitude range $10^o$-$20^o$S.

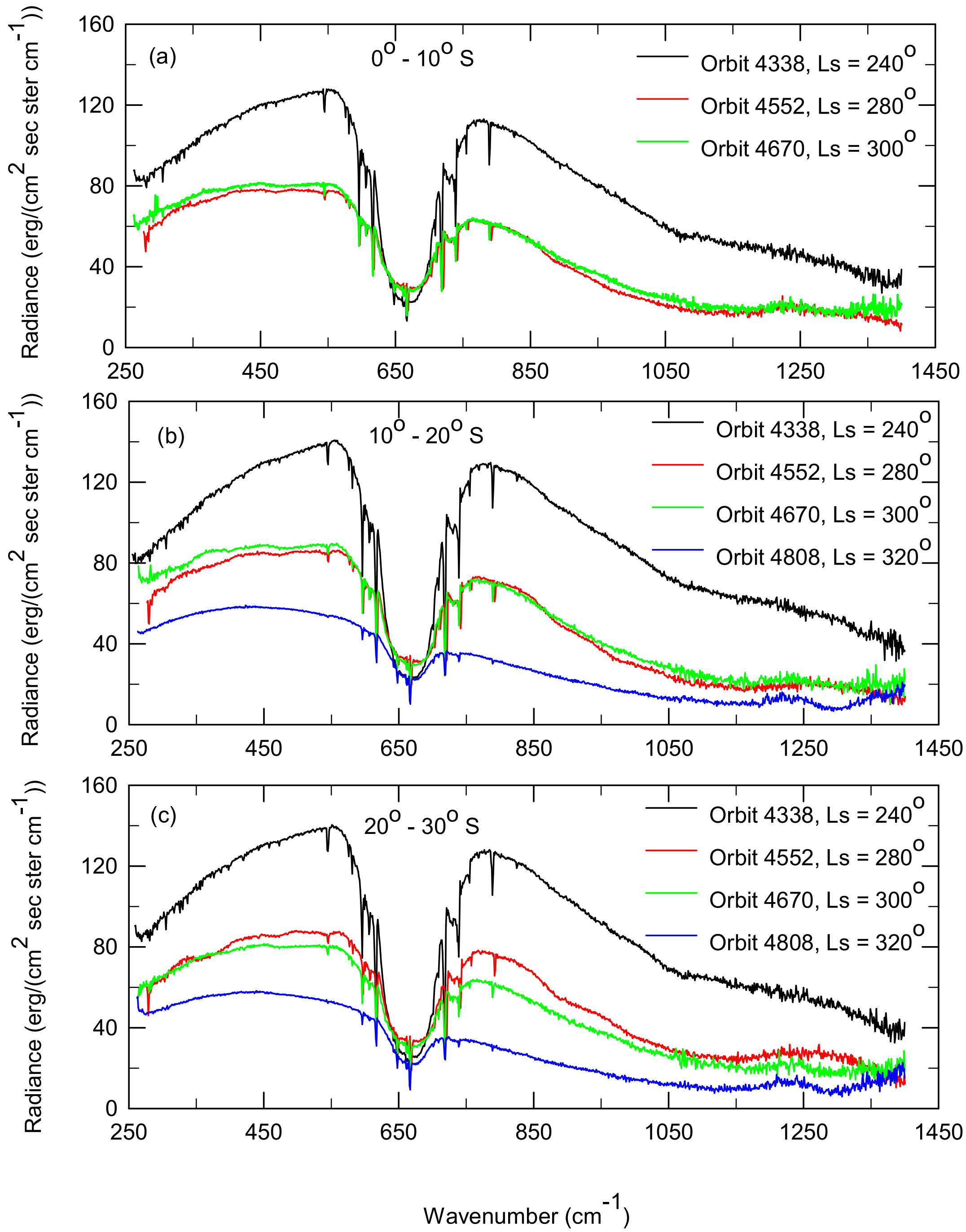


**Figure 4.4a-c The thermal emission spectra observed by PFS instrument during orbit # 4338, 4552, 4670 and 4808 at Ls=240°, 280°, 300° and 320° respectively. These emission spectra are averaged over 10° latitude: (a) 0°-10°S, (b) 10°-20°S and (c) 20°-30°S**.

Several Q-branches are observed in the emission spectra at wave numbers 545, 596, 618, 667, 720, 742 and 792 $cm^{-1}$ due to $CO_2$ isotopic molecules $O^{16}C^{12}O^{16}$,

$O^{16}O^{12}O^{16}$ and $O^{16}C^{13}O^{16}$ (Giuranna et al., 2008). The wave numbers in these spectra are chosen at interval 1.5 $cm^{-1}$. It is found that thermal infrared emission intensities are decreasing with increasing Ls at 240°, 280° and 320° during spring, summer onset and late summer respectively. There is no significant change in the thermal intensities at Ls = 280° and 300° because the season is almost same. In summer the polar caps experiences sublimation due to increase in temperature. The $H_2O$ and $CO_2$ are condensable gases. The abundances of these gases are large during summer due to sublimation process in comparison to that in spring. The thick atmosphere produces less infrared thermal radiations from the surface of Mars. The thermal emission spectra are not changing significantly with latitudes 0°-10°S, 10°-20°S and 20°-30°S. It produces a flat dip at around 900-1200 $cm^{-1}$ due to absorption of dust during storm period at Ls = 280° and Ls = 300°. The effect of dust storm in the emission spectra is not seen in the late spring at Ls = 320°.

Figure 4.5a-c represents the brightness temperature profiles between wave numbers 250-1400 $cm^{-1}$ at latitude range 0°-10°S, 10°-20°S and 20°-30°S respectively. The brightness temperatures are obtained from the thermal emission spectra (shown in Figure 4.5a-c) by inverting Planck function. In the invert calculation, the non-linearity of Planck function will be eliminated. Therefore, the brightness temperature is nearly same at wave number $\leq$ 600 $cm^{-1}$. There is a decrease in brightness temperature due to absorption of dust between wave numbers 900-1200 $cm^{-1}$. When the dust is raised into the atmosphere the daytime temperature decreases because atmospheric layers are cooler than the surface of Mars (Montabone et al., 2015; Wolkenberg et al., 2011).

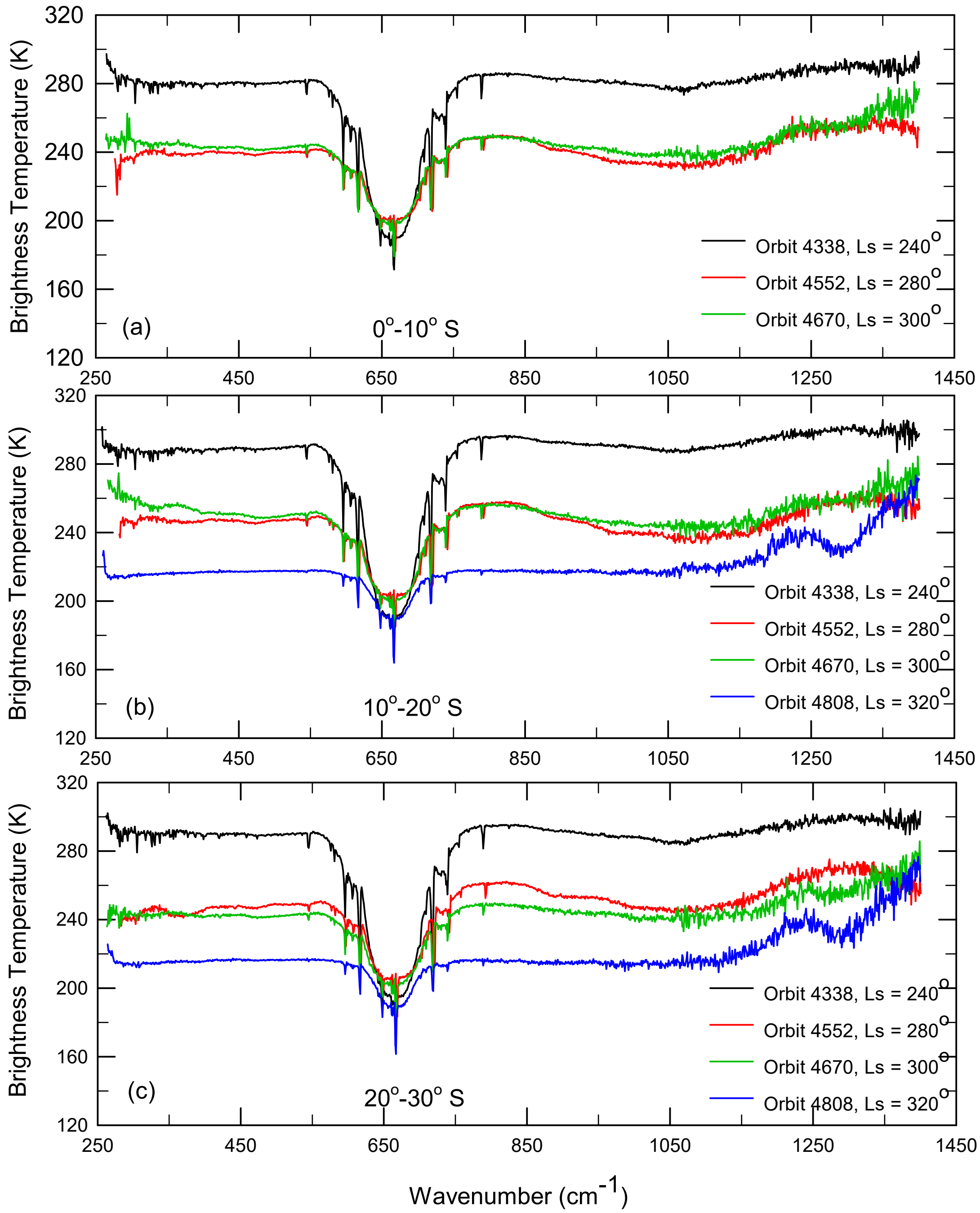


**Figure 4.5a-c The brightness temperature inverted from radiances observed by PFS instrument during orbit # 4338, 4552, 4670 and 4808 at Ls=240º, 280º, 300º and 320º respectively. These temperature spectra are averaged over 10º latitude: (a) 0º-10ºS, (b) 10º-20ºS and (c) 20º-30ºS.**

The major dip in the brightness temperature due to absorption by $CO_2$ is observed at wave number 667 $cm^{-1}$. The Q branches of $CO_2$ isotopic molecules are also seen in the temperature spectra as observed in the infrared thermal emission spectra. The temperature is decreasing with increasing Ls between wave numbers 250-1400 $cm^{-1}$.

The maximum temperature ~ 260-280 K is observed at Ls = 240° when Mars reaches at perihelion and it receives a large amount of solar radiation. The dust storm is observed between summer onset and mid-summer at Ls = 280° and 300° respectively when Mars was moving away from perihelion. The temperature decreases to ~ 220 K during the late summer at Ls = 320°. In this season we have observed a small dip in the temperature at wave number 1300 $cm^{-1}$, which is produced due to low emissivity in presence of larger particles of mineral dust near Christiansen frequency (Formisano et al., 2005).

# 4.3 MODELING OF THERMAL EMISSION SPECTRA

In chapter 2 we have described radiative transfer method for the calculation of thermal emission radiation spectra between wavelength range 200-1400 $cm^{-1}$ at low latitude range 0°-10°S, 10°-20°S, and 20°-30°S for Ls=240°, 280°, 300°, and 320°. These calculations are carried out in MY 28, when a major dust storm occurred in southern hemisphere at low latitude (0°-30°S). The radiative transfer model depends on the density and infrared absorption cross sections of dust, $CO_2$, and $H_2O$. The cross sections of $CO_2$ and $H_2O$ at wave numbers 600-750 $cm^{-1}$ and 300-400 $cm^{-1}$ are taken from ExoMol Spectroscopic Database (www.exomol.com) respectively (Tennyson and Yurchenko, 2012). ExoMol database provides extensive list of molecular transitions which are valid over extended temperature ranges. Hill et al. (2013) reported ~ 2% error in ExoMol data based on computation of rotational and vibrational parameters inside the computer program. The cross section of dust at wave number 900-1200 $cm^{-1}$ is taken from Conrath et al. (1973), who assumed that dust content is pure silicon oxide ($SiO_2$) of spherical size. This assumption is not appropriate because dust is not a pure $SiO_2$ (quartz) nor it is composed of spherical particles. Further this cross section is calculated at room temperature and terrestrial pressure. The cross section of dust (including all type of dust content) at Martian temperature and pressure are not available. Future calculations/or measurement of dust cross section will provide a better data than what is known at present. About 10-20% changes are expected in our model results due to change in dust cross section. The neutral density of $CO_2$ and $H_2O$ are taken from MCD datasets v5.2 (Millour et al., 2014).

## 4.3.1 Calculated Thermal Emission Spectra

In figure 4.6a-c we have compared measured and estimated thermal emission spectra in MY28 between wave number 250-1400 $cm^{-1}$ at latitude range $0^o$-$10^o$S, $10^o$-$20^o$S, and $20^o$-$30^o$S respectively. The thermal emission spectra are calculated in MY 28 at Ls = $240^o$, $280^o$, $300^o$, and $320^o$ by using radiative transfer method. The model reproduces the absorption features of water vapour and $CO_2$ at wave numbers 300-550 $cm^{-1}$ and 600-750 $cm^{-1}$ respectively, except the isotopic Q-branches of $CO_2$ which was not our objective to study in this chapter. The absorption feature due to dust is also reproduced by the model during Ls = $280^o$ and $300^o$ at wave number 900-1200 $cm^{-1}$. This effect is not found in the model and observations during spring and summer at Ls = $240^o$ and $320^o$ respectively because the dust storm was absent in these seasons. We have estimated thermal infrared spectra for different aerosol particle sizes 0.2 to 3 micron at latitude range $0^o$-$10^o$S, $10^o$-$20^o$S, and $20^o$-$30^o$S. The best fit to the measured spectra is obtained between wave number 900-1200 $cm^{-1}$ in presence of aerosol particle of size 0.2 micron. The estimated spectra do not produce a dip at wave number 1300 $cm^{-1}$ during late summer (Ls=$320^o$) because we have not considered compositions of dust materials in the model. We have found that troposphere temperature is reduced by a factor of ~ 2 in presence of dust storm. In the cooler atmosphere the neutral density can also decrease in the troposphere. This can reduce estimated thermal emission spectra by about 50% during the dust storm period.

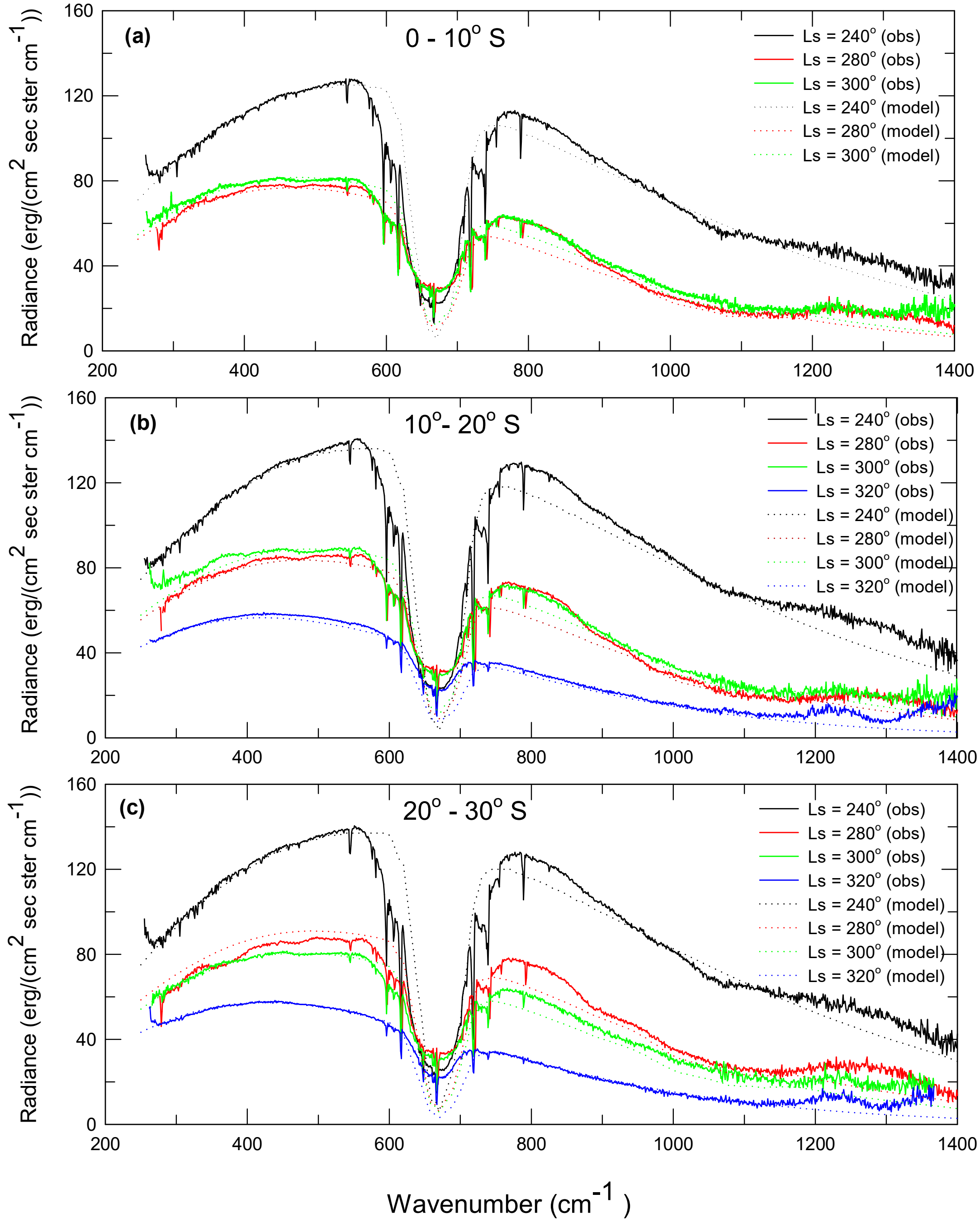


**Figure 4.6a-c Comparison of estimated thermal emission spectra with the measurements carried out by PFS onboard MEX during orbit # 4338, 4552, 4670 and 4808 at Ls = 240°, 280°, 300° and 320° respectively. These emission spectra are averaged over 10° latitude: (a) 0°-10°S, (b) 10°-20°S and 20°-30°**

## 4.3.2 Estimated Thermal Emission Spectra for Dust Storm Condition

In figure 4.7a-c we have shown calculated thermal emission spectra for the peak dust storm period (Ls=280$^{o}$ and $\tau$ =1.2) at latitude range 0$^{o}$-10$^{o}$S, 10$^{o}$-20$^{o}$S and 20$^{o}$-30$^{o}$S respectively. These spectra are plotted between wave number 900-1200 cm$^{-1}$ for aerosol particles of sizes 0.2 to 3.0 micron. The thermal emission intensities are increasing with decreasing the size of the dust particles. It is lowest at wave number 1080 cm$^{-1}$ for dust particle of size 0.2 micron. The absorption is nearly zero for the dust particle of size $\geq$ 3 micron. The maximum emission due to absorption of dust were produced at latitude range 20$^{o}$-30$^{o}$S during the peak dust storm period at Ls = 280$^{o}$ and $\tau$ = 1.2. The emission intensities are lower at latitude range 0$^{o}$-10$^{o}$S and 10$^{o}$-20$^{o}$S by a factor of 1.5-2 in comparison to that estimated at latitude range 20$^{o}$-30$^{o}$S. The figure 4.8a-c shows calculated thermal emission spectra between wave number 900-1200 cm$^{-1}$ for the decline period of the dust storm (Ls=300$^{o}$ and $\tau$=0.5) at latitude range 0$^{o}$-10$^{o}$S, 10$^{o}$-20$^{o}$S and 20$^{o}$-30$^{o}$S respectively. These spectra are also calculated for aerosol particles of sizes 0.2 to 3 micron. During the decline period of dust storm the maximum emissions are produced at latitude range 10$^{o}$-20$^{o}$S. In the decline period of dust storm the emission intensities are lower at latitude range 0$^{o}$-10$^{o}$S and 20$^{o}$-30$^{o}$S by a factor of ~ 1.5 in comparison to that at latitude range 10$^{o}$-20$^{o}$S.

It should be noted that PFS instrument observed instrumental noise in the brightness temperature and thermal emission spectra. The noise in the PFS spectrum is produced due to mechanical and non-mechanical vibration of the spacecraft (Giuranna et al., 2005). Other sources of errors depend upon the measurement conditions. These errors are less than 1% in the measurements (Giuranna et al., 2010). The uncertainties produced by various disturbances can be reduced by the averaging of the spectra (Comolli and Saggin, 2010). We have averaged PFS spectra at 10° latitudes to reduce the random noise. A noise equivalent radiance of 0.2-0.4 erg/cm$^2$/s/sr/cm$^{-1}$ has been deduced from the repeatability of the calibration spectra taken periodically from deep space and from a built-in blackbody (Comolli and Saggin, 2010).

We have studied PFS spectra at low latitude of Mars. The emission spectra can be different at high latitude from low latitude spectra. This is because of the fact that a large amount of $H_2O$ at ≤ 550 cm-1 and $O_3$ at 1042 cm$^{-1}$ are present at high latitude of Mars (Perrier et al., 2006). In order to carry out the modeling of thermal emission spectra at high latitude we should include the $O_3$ gas and its absorption cross section in our model. The concentration of $H_2O$ is also different at low and high latitudes. Therefore, the modeling results of thermal emission spectra and brightness temperature will be significantly different at high latitude from low latitude. There is a need to model high latitude thermal spectra on Mars to understand the global heating of the Martian atmosphere. The PFS has observed thermal emission spectra in northern and southern hemisphere at high latitude region (90$^o$N-67.5$^o$N and 67.5$^o$S-90$^o$S) (Wolkenberg et al., 2018).

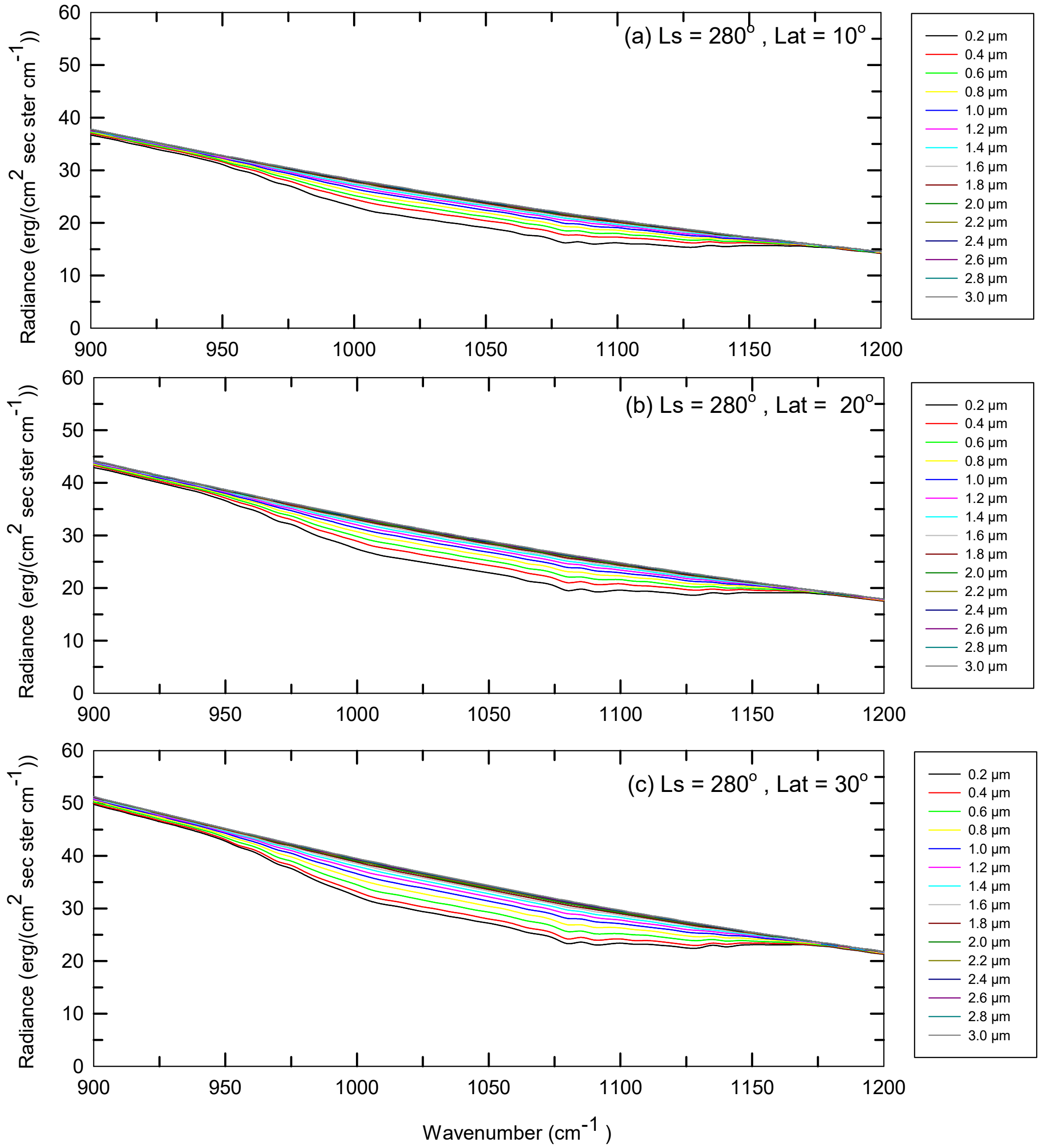


**Figure 4.7a-c The estimated thermal emission spectra between wave number 900-1200 cm$^{-1}$ during dust storm period (Ls=280$^o$) at latitude range (a) 0$^o$-10$^o$S, (b) 10$^o$-20$^o$S and (c) 20$^o$-30$^o$S.**

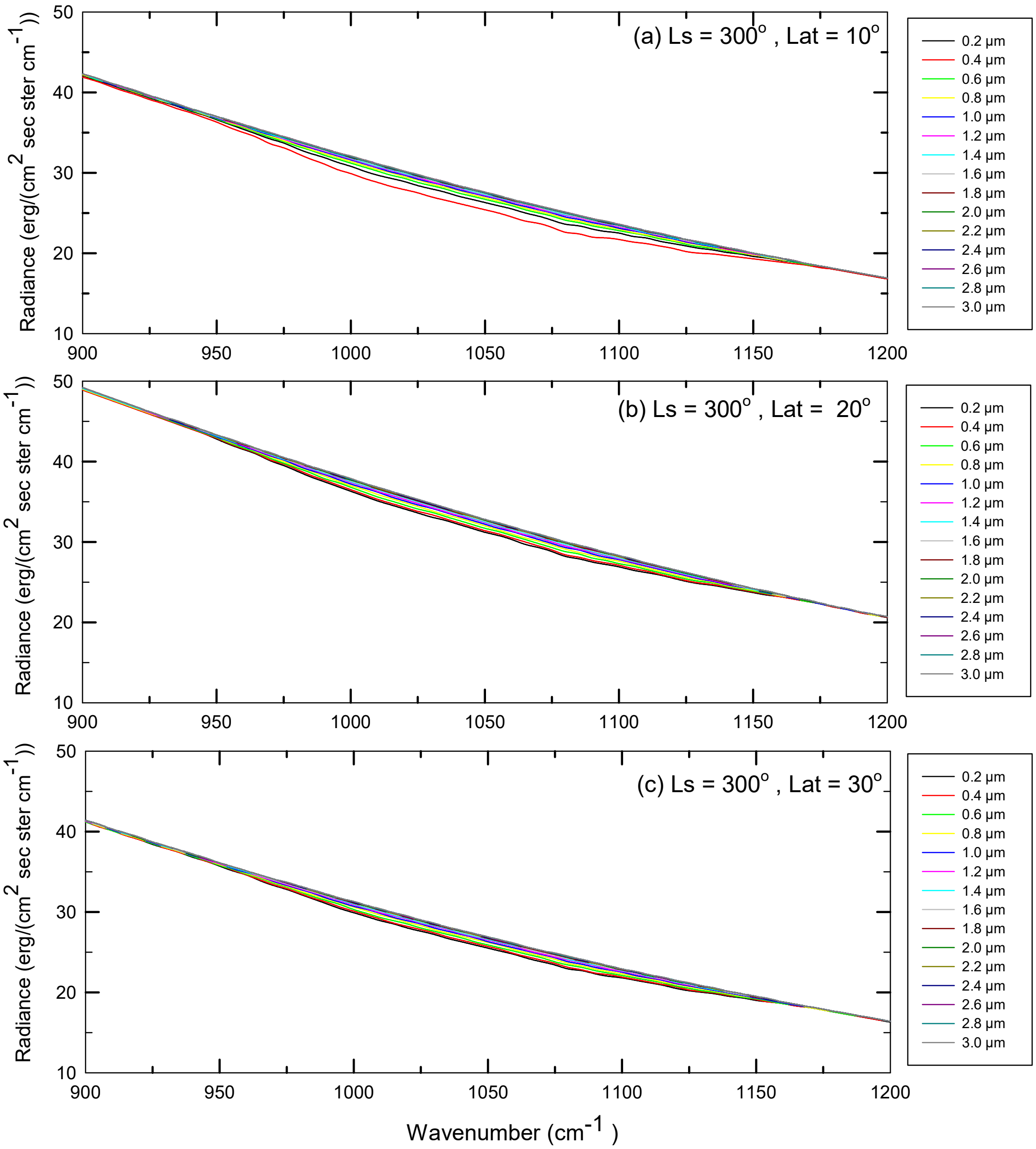


**Figure 4.8a-c The estimated thermal emission spectra between wave number 900-1200 cm$^{-1}$ during the decline period of dust storm (Ls=300°) at latitude range (a) 0°-10°S, (b) 10°-20°S and (c) 20°-30°S.**

# REFERENCES

Aoki, S., Giuranna, M., Kasaba, Y., Nakagawa, H., Sindoni, G., Geminale, A., and Formisano, V. (2015). Search for hydrogen peroxide in the Martian atmosphere by the Planetary Fourier Spectrometer onboard Mars Express. Icarus, **245**, 177-183.

Christensen, P. R., Bandfield, J. L., Hamilton, V. E., Ruff, S. W., Kieffer, H. H., and Titus, T. N., et al. (2001). Mars Global Surveyor Thermal Emission Spectrometer experiment: investigation description and surface science results. Journal of Geophysical Research: Planets, **106**(E10), 23823-23871.

Comolli, L., and Saggin, B. (2010). Analysis of disturbances in the Planetary Fourier Spectrometer through numerical modeling. Planetary and Space science, **58**(5), 864-874.

Conrath, B., Curran, R., Hanel, R., Kunde, V., Maguire, W., Pearl, J., Pirraglia, J., Welker, J., and Burke, T. (1973). Atmospheric and surface properties of Mars obtained by infrared spectroscopy on Mariner 9, Journal of Geophysical Research, **78** (20), 4267-4278.

Forget, F., and Montabone, L. (2017, July). Atmospheric dust on Mars: A review. 47th International Conference on Environmental Systems.

Formisano, V., Atreya, S., Encrenaz, T., Ignatiev, N., and Giuranna, M. (2004). Detection of methane in the atmosphere of Mars. Science, **306**(5702), 1758-1761.

Formisano, V., Angrilli, F., Arnold, G., Atreya, S., Bianchini, G., Biondi, D., et al. (2005). The Planetary Fourier Spectrometer (PFS) onboard the European Mars Express mission, Planetary and Space science, **53**(10), 963-974.

Fouchet, T., Lellouch, E., Ignatiev, N. I., Forget, F., Titov, D. V., Tschimmel, M., et al. (2008). Martian water vapor: Mars Express PFS/LW observations, Icarus, **190**(1), 32-49.

Geminale, A., Formisano, V., and Giuranna, M. (2008). Methane in Martian atmosphere: average spatial, diurnal, and seasonal behaviour. Planetary and Space Science, **56**(9), 1194-1203.

Geminale, A., Formisano, V., and Sindoni, G. (2011). Mapping methane in Martian atmosphere with PFS-MEX data. Planetary and Space Science, **59**(2-3), 137-148.

Giuranna, M., Grassi, D., Formisano, V., Montabone, L., Forget, F., and Zasova, L. (2008). PFS/MEX observations of the condensing CO2 south polar cap of Mars. Icarus, **197**(2), 386-402.

Giuranna, M., Formisano, V., Biondi, D., Ekonomov, A., Fonti, S., Grassi, D., et al. (2005). Calibration of the Planetary Fourier Spectrometer long wavelength channel. Planetary and Space Science, **53**(10), 993-1007.

Giuranna, M., Roush, T. L., Duxbury, T., Hogan, R. C., Carli, C., Geminale, A., and Formisano, V. (2011). Compositional interpretation of PFS/MEx and TES/MGS thermal infrared spectra of Phobos. Planetary and Space Science, **59**(13), 1308-1325.

Giuranna, M., Wolkenberg, P., Grassi, D., Aronica, A., Aoki, S., Scaccabarozzi, D and PFS Team. (2018). New dataset of atmospheric parameters retrieved by PFS-Mex. In workshop: From Mars Express to ExoMars (pp. 27-28).

Hanel, R. A., Conrath, B. J., Hovis, W. A., Kunde, V. G., Lowman, P. D., Pearl, J. C., et al. (1972). Infrared spectroscopy experiment on the Mariner 9 mission: Preliminary results. Science, **175**(4019), 305-308.

Haus, R., and Titov, D. V. (2000). PFS on Mars Express: preparing the analysis of infrared spectra to be measured by the Planetary Fourier Spectrometer. Planetary and Space Science, **48**(12-14), 1357-1376.

Hill, C., Yurchenko, S. N., and Tennyson, J. (2013). Temperature-dependent molecular absorption cross sections for exoplanets and other atmospheres. Icarus, **226**(2), 1673-1677.

Ignatiev, N. I., Grassi, D., and Zasova, L. V. (2005). Planetary Fourier spectrometer data analysis: Fast radiative transfer models. Planetary and Space Science, **53**(10), 1035-1042.

Kass, D. M., Kleinböhl, A., McCleese, D. J., Schofield, J. T., and Smith, M. D. (2016). Interannual similarity in the Martian atmosphere during the dust storm season. Geophysical Research Letters, **43**(12), 6111-6118.

Kieffer, H. H., Martin, T. Z., Peterfreund, A. R., Jakosky, B. M., Miner, E. D., and Palluconi, F. D. (1977). Thermal and albedo mapping of Mars during the Viking primary mission. Journal of Geophysical Research, **82**(28), 4249-4291.

Määttänen, A., Fouchet, T., Forni, O., Forget, F., Savijärvi, H., Gondet, B., et al. (2009). A study of the properties of a local dust storm with Mars Express OMEGA and PFS data. Icarus, **201**(2), 504-516.

Millour, E., Forget, F., Spiga, A., Navarro, T., Madeleine, J. B., Pottier, A., et al. (2014, January). A new Mars climate database v5. 1.

Montabone, L., Forget, F., Millour, E., Wilson, R. J., Lewis, S. R., Cantor, B., et al. (2015). Eight-year climatology of dust optical depth on Mars. Icarus, **251**, 65-95.

Perrier, S., Bertaux, J. L., Lefèvre, F., Lebonnois, S., Korablev, O., Fedorova, A., and Montmessin, F. (2006). Global distribution of total ozone on Mars from SPICAM/MEX UV measurements. Journal of Geophysical Research: Planets, **111**(E9).

Sato, T. M., Fujiwara, H., Takahashi, Y. O., Kasaba, Y., Formisano, V., Giuranna, M., and Grassi, D. (2011). Tidal variations in the Martian lower atmosphere inferred from Mars Express Planetary Fourier Spectrometer temperature data. Geophysical Research Letters, **38**(24).

Sheel, V., and Haider, S. A. (2016). Long-term variability of dust optical depths on Mars during MY24-MY32 and their impact on subtropical lower ionosphere: Climatology, modeling, and observations. Journal of Geophysical Research: Space Physics, **121**(8), 8038-8054.

Sindoni, G., Formisano, V., and Geminale, A. (2011). Observations of water vapour and carbon monoxide in the Martian atmosphere with the SWC of PFS/MEX. Planetary and Space Science, **59**(2-3), 149-162.

Smith, M. D. (2009). THEMIS observations of Mars aerosol optical depth from 2002-2008. Icarus, **202**(2), 444-452.

Tennyson, J., and Yurchenko, S. N. (2012). ExoMol: molecular line lists for exoplanet and other atmospheres. Monthly Notices of the Royal Astronomical Society, **425**(1), 21-33.

Wolkenberg, P., Smith, M. D., Formisano, V., and Sindoni, G. (2011). Comparison of PFS and TES observations of temperature and water vapor in the Martian atmosphere. Icarus, **215**(2), 628-638.

Wolkenberg, P., Giuranna, M., Grassi, D., Aronica, A., Aoki, S., Scaccabarozzi, D., and Saggin, B. (2018). Characterization of dust activity on Mars from MY27 to MY32 by PFS-MEX observations. Icarus, **310**, 32-47.

Zasova, L., Formisano, V., Moroz, V., Grassi, D., Ignatiev, N., Giuranna, M., Hansen, G., Blecka, M., Ekonomov, A., Lellouch, E., and Fonti, S. (2005). Water clouds and dust aerosols observations with PFS MEX at Mars, Planetary and space science, **53**, 1065-1077.

❑❑❑

# CHAPTER - 5

# SEASONAL VARIABILITY OF OZONE HEATING RATES IN LOWER ATMOSPHERE OF MARS

# CONTENTS

*We have used SPICAM observations from MY27 to MY31 to study the seasonal variability of column abundances of ozone and dust opacity at low latitudes (10°-30°N, 10°-30°S), mid-latitudes (30°-50°N, 30°-50°S) and high latitudes (50°-70°N, 50°-70°S). In these observations year-to year seasonal variability of column ozone at latitude ~25°S were nearly same except in MY 28 at Ls~280°-310° when a global dust storm occurred. The altitude profiles of ozone heating rates are calculated in presence of dust storm at latitudes 2°N-S, 25°N-S, 45°N-S and 70°N-S for Ls~7.5°, 47.5°, 87.5°, 127.5°, 167.5°, 207.5°, 247.5°, 287.5° and 327.5°. At low and mid-latitudes, the ozone heating rates increased until Ls~47.5°. Afterwards it decreased until Ls~ 127.5° and then disappeared between Ls~ 167.5° and 327.5°. We have also used MCD datasets (https:hal.archives-ouvertes.fr/hal-01139592) to study the seasonal variability of zonal, meridional and vertical winds in the tropical atmosphere of Mars during MY28 and MY29. It is found that the density of ozone, wind speeds and ozone heating rates were severely affected by the global dust storm at latitude ~25°S and Ls ~ 280°.*

# 5.1 INTRODUCTION

Several dust storms have been observed on Mars. Some dust storms affect small region of the planet while other dust storms can cover the entire planet. These observations were carried out in last 2-3 Martian decades between MY10 and MY34 (Martin, 1995; Montmessin et al., 2017; Willame et al., 2017, Guzewich et al., 2019). The infrared spectrometers onboard MGS and Mars Odyssey have observed two major dust storms in MY25 and MY28 at low latitude ~ 25°S where the optical depths were increased up to ~ 1.7 and 1.2 at Ls = 210° and Ls = 280° respectively (Sheel and Haider, 2016). These dust optical depths were observed by MGS and Mars Odyssey between 14 July 1998 to 31 August, 2004 and 1 September, 2004 to 31 October, 2014 respectively. The zonal mean UV dust opacity is also observed in southern hemisphere onboard MEX between MY27 and MY30. The dust opacity measured by SPICAM is larger by a factor of 2.5 than that observed by Mars Odyssey.

During a dust storm elevated dust heats the atmosphere at high altitudes while shading and cooling near the surface. Because of increased heating during large dust storms the dust amplifies the Hadley circulation (Zalucha et al., 2010; Mitchell et al., 2015). The atmospheric dust slowly settles on the surface of Mars in absence of the winds. The dust in the atmosphere absorbs solar radiation and radiates heat at night and thus significantly changes the forcing of atmospheric dynamics. This can lead to extremely strong winds, which in turn cause more dust lifting which can lead to planet-wide dust storms. The major dust storms occur after 3-4 Mars years at low latitudes of southern hemisphere while regional dust storms occur every year during the summer (Sheel and Haider, 2016).

In this chapter, we have used SPICAM observations from MY27 to MY30 to study the seasonal variability of zonally averaged column abundances of ozone and dust opacity in the daytime atmosphere of Mars. We have also calculated the seasonal variability of zonal mean heating rates in the troposphere of Mars due to UV absorption by $O_3$ between wavelengths 200 nm and 300 nm in presence and absence of dust storm corresponding to MY28 and MY29 respectively between altitudes 0 to 60 km and Ls ~ $0^o$ to $360^o$ at low latitudes ($2^o$N, $2^o$S, $25^o$N and $25^o$S), mid latitudes ($45^o$N and $45^o$S) and high latitudes ($70^o$N and $70^o$S) (González-Galindo et al., 2005). MCD data is used to investigate the seasonal variability of ozone heating rates, zonal, meridional and vertical winds at different altitudes and latitudes in MY28 and MY29. The strong effects of the dust storm were found on ozone heating rates and winds at altitude ≤ 10 km in southern summer at latitude ~ $25^o$S and Ls ~ $280^o$. During the dust storm period the ozone heating rates increased by a factor of ~ 2.5-3.

### 5.1.1 General Circulation Model (GCM)

MCD is developed based on GCM for different scenario of dust and solar conditions (Millour et al., 2014; Wang and Lee, 2017), which has been developed at Laboratoire de Meteorologic Dynamique du CNRS (Paris, France) in collaboration with Open University (UK), Oxford University (UK), Institute de Astrofisica de Andalucia (Spain), and Centre National d' Etudes Spatiales. This model solves a finite difference primitive equations that self-consistently calculates neutral, ion, and electron densities over the globe under solar minimum, moderate and maximum conditions for different Mars seasons (website: http://www-mars.lmd.jussieu.fr). The zonal, meridional, and vertical winds, temperature and pressure in the Mars' atmosphere at different latitude, longitude and season are also calculated in this model. The MCD model can be varied for individual cases including $f_{10.7}$ index (solar X-ray/EUV/UV flux variation), heliocentric distance (orbital-variation), solar declination (seasonal variation) and maximum eddy coefficient (eddy diffusion and viscosity). This model is also modified to accommodate atmospheric inflation and semi-diurnal/diurnal tidal mode amplitudes and phases consistent with dusty conditions in the Mars lower atmosphere during the dust storms. This model is validated using the available observed data (Lefevre et al., 2008; Millour et al., 2014; Haider et al., 2019).

The atmosphere of Mars is changing in presence of low, medium and high dust storm condition. The ionosphere of Mars is also changing during low, medium and high solar activity, in presence of solar flares, and 27-day solar rotation. The MCD model predicts air density and mixing ratios of various gases at different latitude, longitude and season for climatology scenario, cold scenario, warm scenario and dust scenario of Mars' atmosphere (Millour et al., 2014). The solar minimum, medium and maximum conditions of the Mars' atmosphere are considered in the climatology scenario. The cold scenario corresponds to extremely clear atmosphere. The warm dust scenario represents dusty atmosphere. The dust opacity is considered to be the minimum between MY24 and MY31 except maximum during global dust storms occurred in MY25 and MY28 at Ls ~ $280^o$. The effects of global dust storms are included in the dust scenario. In this scenario dust opacity $\tau = 5$ is taken for dust storm period at a given location and season.

## 5.1.2 SPICAM Observations

The SPICAM UV-IR dual spectrometer is dedicated to study the atmosphere of Mars (Bertaux et al., 2006). The UV spectrometer observed vertical profiles of $O_3$ and dust opacity by stellar occultation in the nighttime atmosphere of Mars. This instrument cannot measure the altitude profiles of $O_3$ and dust opacity in the daytime atmosphere at altitude ≤ 60 km where the star signals are very weak. It has observed column integrated UV dust opacity and ozone column abundances during the daytime atmosphere at different seasons, latitudes and longitudes between MY27 and MY30 (Montemessin et al., 2017). The IR spectrometer observed water column abundances in the daytime atmosphere. Both spectrometers were carried out simultaneously in nadir mode to understand the coupling processes of dust, $H_2O$ and $O_3$ in the Martian atmosphere.

The UV spectrometer also observed density of $CO_2$ and temperature profiles in the nighttime atmosphere from stellar occultation between altitudes 70 km and 130 km (Forget et al., 2009). The IR spectrometer is measuring vertical profiles of $O_2$ ($a^1\Delta g$) nightglow emissions at 1.27 μm in northern and southern polar latitudes. The emission peaks of $O_2$ ($a^1\Delta g$) band were observed at altitude range 35-42 km and 40-55 km above the north and south poles respectively. The integrated column emission rate of $O_2$ ($a^1\Delta g$) is reported by Montmessin et al. (2017) in the daytime atmosphere of Mars between MY27 and MY31. The nightglow aurora was also discovered by UV spectrometer in δ (190-240 nm) and γ (225-270 nm) bands, which were produced by radiative recombination process between $O(^3P)$ and $N(^4S)$ due to electron impact excitation of nitric oxide (NO) molecules (Bertaux et al., 2005; Cox et al., 2008). The Martian NO nightglow aurora is a localized emission controlled by the southern crustal magnetic field anomalies.

The SPICAM has also observed the CO and $CO_2^+$ ultraviolet dayglow limb profiles. Cox et al. (2010) have reported altitude profiles of limb intensity of CO ($a^3\pi$ - $X^1\Sigma^+$) Cameron bands and $CO_2^+$ doublet at 298 nm and 299 nm respectively between altitude 100 km and 150 km. The average peak height of Cameron band intensity is located at 121.1 ± 6.5 km. They have reported that the Cameron band intensity depends on solar zenith angle, solar activity and local $CO_2$ density profiles. The SPICAM dayglow spectra also observed $N_2$ Vegard-Kaplan bands (Leblanc et al., 2007). The altitude profile of this emission was modelled by Jain and Bhardwaj (2011) and Fox and Hac (2013). The latter found that the predicted limb intensities were fully consistent with those observed by SPICAM. In the present chapter we have studied the effects of dust loading on ozone, winds and heating rates in the dayside atmosphere of Mars.

Among the various observations of SPICAM we have used column abundance of ozone and dust opacity measurements in this chapter to study the seasonal dependence on Mars' atmosphere. The dust plays an important role in absorbing and scattering the solar and thermal radiations on Mars. It affects the thermal contrast between the atmosphere and the surface by heating and cooling during the dust storm seasons. The dust also affects the chemistry of ozone and their abundances (Haider et al., 2019). There is a need to study thermal emission of Mars in order to understand the atmospheric heating rates and atmospheric circulation where dust actively controls the heat transfer in the lower atmosphere (Mischna et al., 2012; Willame et al., 2017). The ozone strongly absorbs UV radiation in the 255 nm region and hence continuous monitoring and modeling of ozone heating rate is essential to characterize the UV radiation reaching on the surface of Mars.

## 5.2 MARS' SEASONS

The Mars has two different kinds of seasons that interact throughout the course of a Martian year (nearly two times longer than what we know as a year on Earth). These are the familiar winter, spring, summer and fall seasons caused by the Mars' tilt ~ $25^{o}$ in comparison to Earth's tilt ~ $23^{o}$. But there are also two additional seasons, aphelion and perihelion, which occur because of Mars' highly elliptical orbit. Earth's orbit is nearly circular, meaning its distance from the sun stays largely stable. Mars' orbit is more elongated, bringing it much closer to the sun at some times of the year than others.

Mars gets about 40% more energy from the sun during perihelion, when the planet is closest to the sun than during aphelion. Mars is warmer when it is near the sun and cooler when it is far from the sun. It has been found that heavy storms of thick cloud cover in the winter and dust move over Mars' continents toward the equator. When Mars sweeps closest to the Sun during its southern hemisphere summer, temperature increases greatly and the extra energy creates the dust storms that cover a large region of Mars. The global dust storms occur only during perihelion season and once every 3-4 MY. During dust storm period winds blow up to 100-150 mph in the Martian atmosphere.

### 5.2.1 Seasonal variability of column ozone and dust opacity observed by SPICAM

The figures 5.1 (a-f) and 5.2 (a-f) represent comparison of seasonal variability of zonally averaged column ozone and column dust opacity respectively for four Martian years as observed by SPICAM between MY 27 and MY 30 in northern and southern hemispheres at low latitudes ($10^o$-$30^o$N, $10^o$-$30^o$S), mid-latitudes ($30^o$-$50^o$N, $30^o$-$50^o$S) and high latitudes ($50^o$-$70^o$N, $50^o$-$70^o$S). These are complete datasets which have been observed by SPICAM for the study of the Martian atmosphere. In these observations, year-to-year seasonal variability of column ozone is nearly the same in the southern low latitudes, except in MY 28 at Ls ~ $280^o$- $310^o$ when a global dust storm occurred. In northern hemisphere the column ozone is maximum in spring and minimum in summer at low latitude (figure 5.1a). In this region the maximum column ozone is also observed during autumn and winter. The SPICAM data is not available in MY 27 and MY 30 at low latitude during northern autumn. The column ozone is also not observed in MY28 at low latitude during northern winter. The maximum column ozone is produced in southern autumn (figures 5.1 (d-f)). In figure 5.1d SPICAM represents the second peak in column ozone at Ls ~ $300^o$. This peak is produced due to effect of dust storm on ozone column density in MY 28. In both hemispheres column ozone at low latitudes are lower by a factor of 4-5 than at mid and high latitudes. It is also found that the column ozone is more in southern hemisphere than the northern hemisphere. At mid-to-high latitudes, the column ozone is the largest between late winter and early spring in northern hemisphere and between spring and summer in southern hemisphere (figures 5.1b, 5.1c and 5.1e, 5.1f). Similarly, at these latitudes the column ozone is the largest in southern winter and close to zero in northern summer. This observation shows that ozone loss is very fast in northern hemisphere during the early spring (Ls ~$10^o$-$40^o$), and decreases by about 10 μm-atm in the mid-summer (Ls ~ $100^o$-$150^o$). The figures 5.2 (d-f) represent that the column dust opacity increased by a factor of ~ 3 at about all southern latitudes during the global dust storm which occurred in MY28 between Ls ~ $280^o$ to $310^o$. The effects of MY28 dust storm was found on column ozone at low latitudes only because the column ozone is almost zero at mid and high latitudes (figures 5.1d-f). In absence of dust storm during MY 27 to MY 30 - the minimum clear opacity of dust is observed ~ 0.2 to 0.5 in northern hemisphere (figures 5.2 (a-c)) while in southern hemisphere the dust opacity is observed ≤ 0.5 at Ls ~ $0^o$ to $120^o$ and then stabilized at about ~ 1.0 between Ls ~ $130^o$ and $360^o$ (figures 5.2 (d-f)). The dust opacity close to 1.0 may be associated with the regional dust storm which occurs every year during MY27 to MY30 in southern hemisphere. During these years the regional dust storms are relatively mild at low latitude ($10^o$-$30^o$S) in comparison to mid latitude ($30^o$-$50^o$S) and high latitude ($50^o$-$70^o$S). In MY 28 the dust opacity increased up to 3 over the entire planet in southern hemisphere for several weeks.

The dust opacity ≤ 0.5 can be considered for clear atmosphere of Mars during the absence of dust storm. In the dust storm of MY 28 a large amount of dust was lifted up into the atmosphere and formed two distinct layers at altitude range of ~ 20-30 km and ~ 45-65 km (Haider et al., 2015). These dust layers have been observed by CRISM and MCS onboard MRO (Guzewich et al., 2014; Heavens et al., 2014; Haider et al, 2015). These dust layers cannot be seen in figures 5.2 (a-f) because the column integrated dust opacity is plotted in these figures. Since year to-year seasonal change are nearly same we have used only two Martian years of SPICAM observations carried out in MY 28 and MY 29 to study the meteorology of the Martian atmosphere in presence and absence of dust storm respectively.

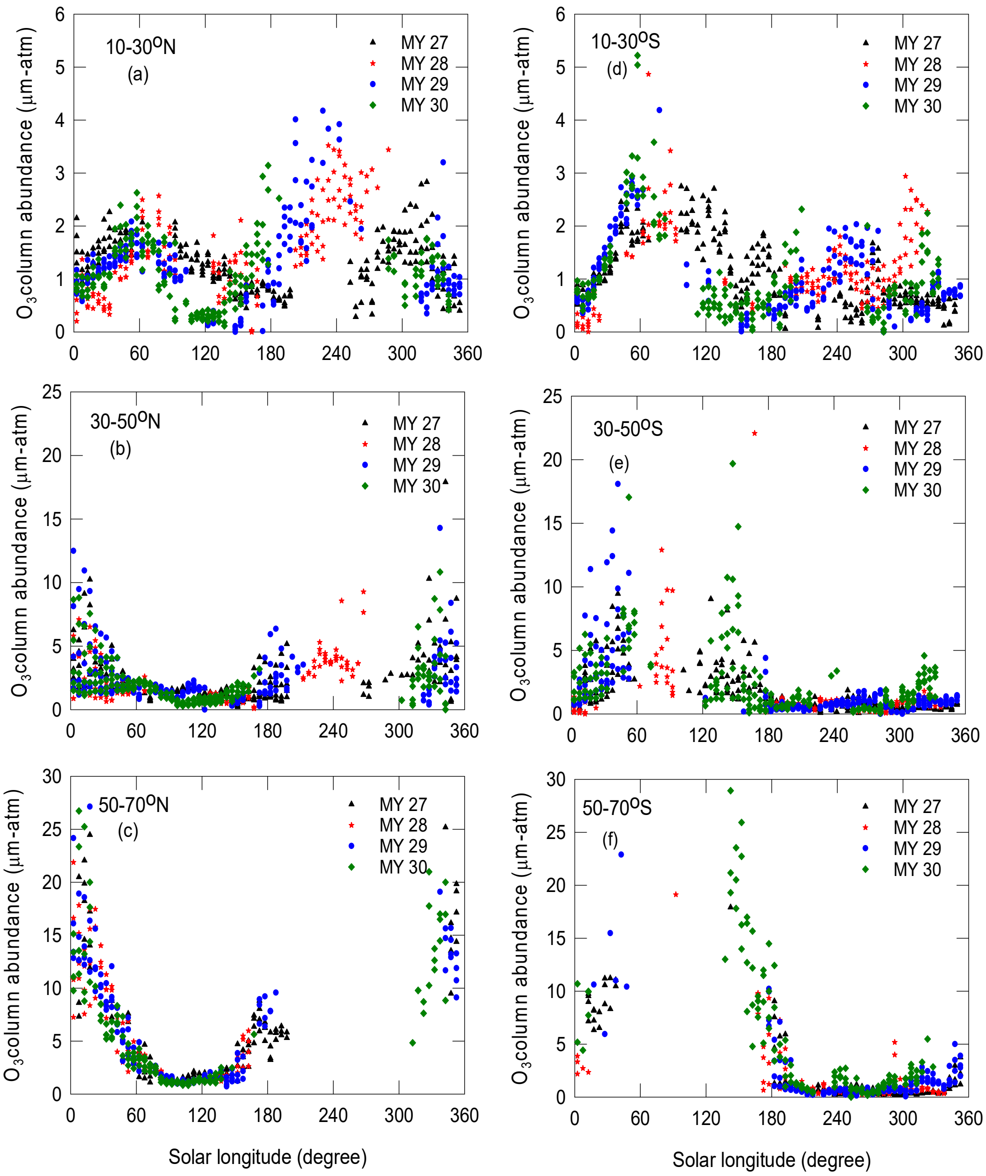


**Figure 5.1 (a-f) The seasonal variability of zonally averaged column ozone at (a) 10$^{o}$-30$^{o}$N, (b) 30$^{o}$-50$^{o}$N, (c) 50$^{o}$-70$^{o}$N, (d) 10$^{o}$-30$^{o}$S, (e) 30$^{o}$-50$^{o}$S, (f) 50$^{o}$-70$^{o}$S observed by SPICAM between MY 27 and MY 30.**

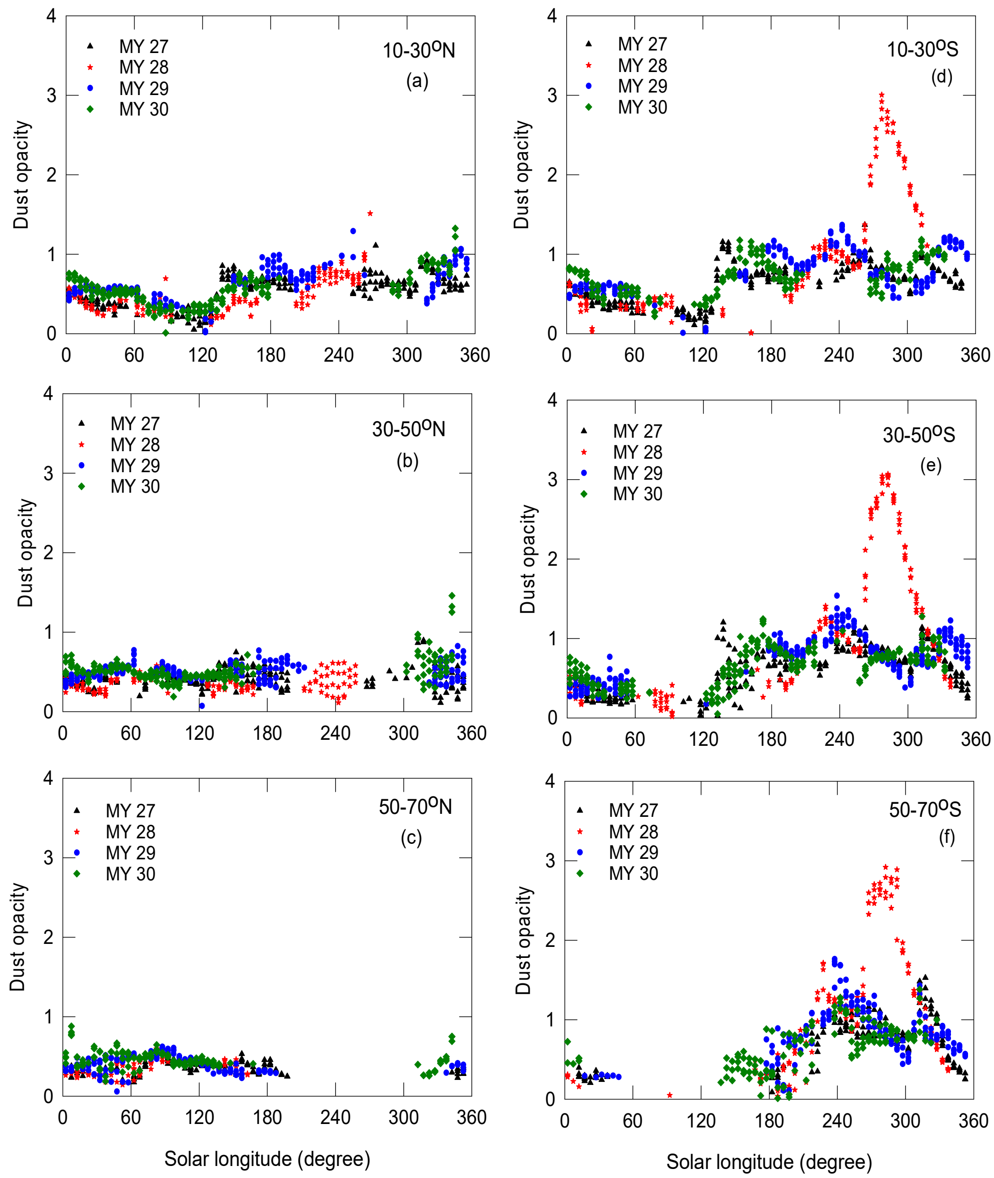


**Figure 5.2 (a-f) The seasonal variability of zonally averaged dust opacity at (a) 10$^{o}$-30$^{o}$N, (b) 30$^{o}$-50$^{o}$N, (c) 50$^{o}$-70$^{o}$N, (d) 10$^{o}$-30$^{o}$S, (e) 30$^{o}$-50$^{o}$S, (f) 50$^{o}$-70$^{o}$S observed by SPICAM between MY 27 and MY 30.**

### 5.2.2 Estimated seasonal variability of density and heating rates of ozone

We have plotted zonal mean ozone density in figures 5.3 (a-e) (left) and zonal mean ozone heating rates in figures 5.3 (f-j) (right) at low latitude 25°S between Ls ~ 0° to 360° and altitude 0 km to 60 km in MY28 and MY29. The altitude profiles of ozone heating rates at low, mid and high latitudes (2°N-S, 25°N-S, 45°N-S, and 70°N-S) are shown in section 5.3.2 for MY28. In the calculation of heating rates, density of ozone is taken from the MCD model (Millour et al., 2014). The solar flux and absorption cross-section of $O_3$ in the wavelengths of 200-300 nm are taken from Tobiska et al. (2000) and Serdyuchenko et al. (2014) respectively. The amplitude of seasonal changes in ozone and ozone heating rates are low at altitudes ≤ 10 km, but at altitudes ≥ 10 km it is chaotic and indicates that atmospheric ozone is highly perturbed. We have found three peaks at Ls ~ 50°, 170°, and 280° in figures 5.3a and 5.3f at altitude 0 km and two peaks at Ls ~ 50° and 280° in figures 5.3b and 5.3g at altitude 10 km. The seasonal variability of ozone and ozone heating rates are almost the same in MY 28 and MY 29 except at Ls ~ 280° during the global dust storm period in MY 28. In the presence of the global dust storm ozone and ozone heating rates increased by a factor of ~ 2.5-3 (it is marked by arrow) up to 10 km at Ls ~ 280°. Above this altitude the effect of dust storm is almost negligible on them.

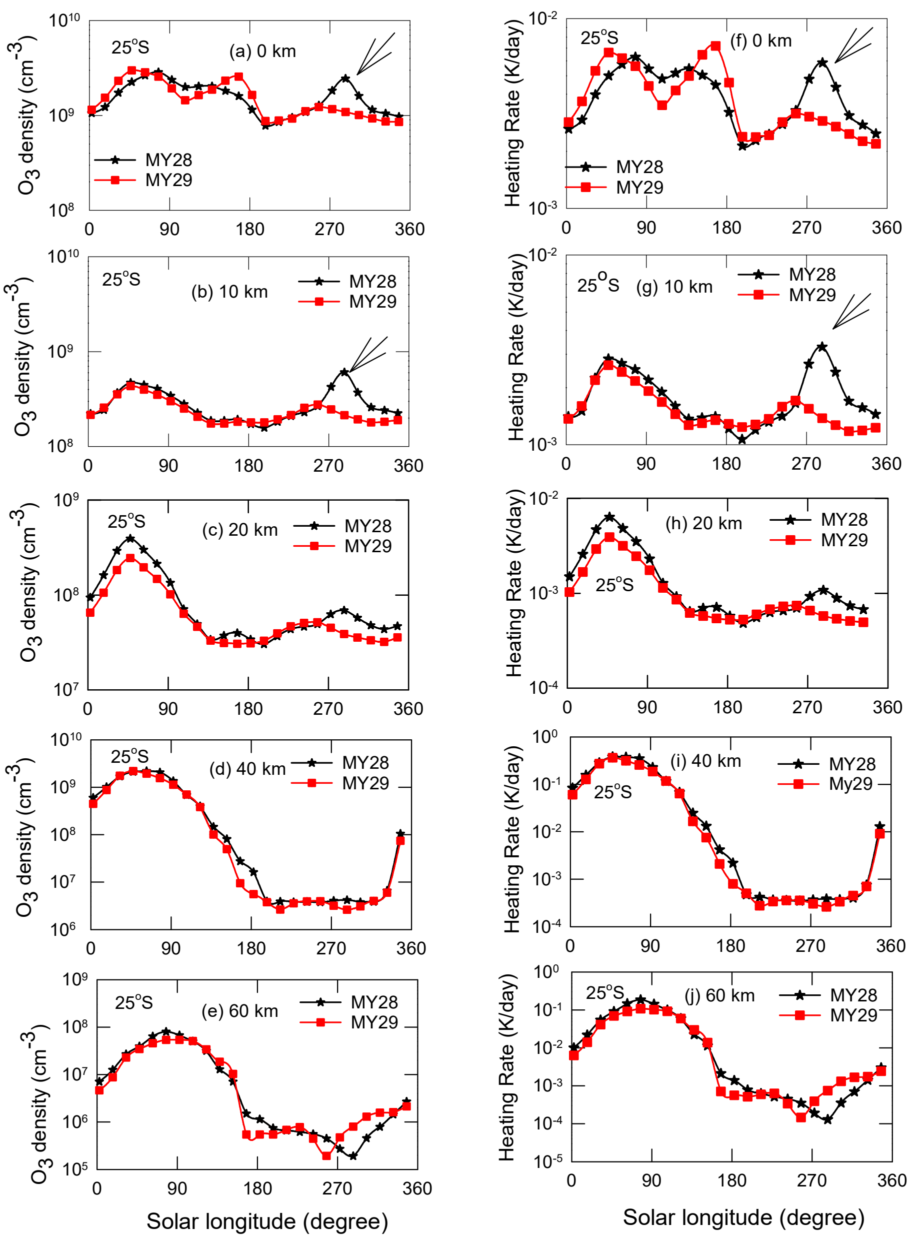


**Figure 5.3 (a-j) The estimated seasonal variability of zonally averaged ozone density at (a) 0 km, (b) 10 km, (c) 20 km, (d) 40 km and (e) 60 km (left panel); The estimated seasonal variability of ozone heating rates at (f) 0 km, (g) 10 km, (h) 20 km, (i) 40 km and (j) 60 km (right panel) for MY28 and MY29 at 25ºS.**

## 5.3 DUST LOADING ON WIND SPEED AND HEATING RATES OF OZONE

The dust storms on Mars can develop in few hours and spread over the entire planet within couple of days. The dust storms are known to affect the meteorological parameters viz. ozone, water vapor, temperature, pressure, humidity and winds on Mars (Cavalie et al., 2008; Lefevre et al., 2008; Kuroda et al., 2008; Medvedev et al., 2011; Wilson et al., 2018; Haider et al., 2019). In the present section we have studied responses of the dust loading on wind speed and heating rates in the tropics of the southern atmosphere of Mars corresponding to the dust storm of MY 28 when optical depths were increased up to 1.2. Recently MSL curiosity rover measured a global dust storm in MY 34 by MASTCAM instrument. The optical depth was increased up to 8.5 during this dust storm on June 10, 2018 at Ls ~ 190$^o$ (Guzewich et al., 2019). This optical depth is larger than that observed by earlier dust storms by a factor of ~ 5 to 7. In the MCD model the neutral density profiles are not upgraded for recent dust storm of MY 34. Recently Liu et al. (2018) have reported based on Mars Atmosphere and Volatile Evolution (MAVEN) observations that the neutral atmosphere in response to dust increases at altitudes as high as 160 km by factors of 2 to 5. This increase in the neutral atmosphere can change the meteorology of Mars significantly and we can find nearly 50% to 200% enhancement more on the present results for the dust storm of MY 34. These studies indicate that during the major dust storm whole atmosphere expands and rises, and modified circulation can be involved in the Mars' atmosphere. In section 5.3.1 we have described zonal wind, meridional wind, and vertical wind speeds in presence and absence of dust storm in MY 28 and MY 29 respectively. Since there is no much difference in ozone heating rate profiles corresponding to MY 28 and MY 29 except near the surface when a global dust storm occurred in MY 28, we have plotted estimated results of ozone heating rates of MY 28 only in section 5.3.2. The wind speeds are calculated by GCM in MY 28 and MY 29. In brief GCM is described in section 5.1.1. The theory and input parameters for the calculation of ozone heating rates are given in chapter 2.

### 5.3.1 Estimated wind speeds in MY 28 and MY 29

The figures 5.5(a-e), 5.5(f-j) and 5.5(k-o) represent the seasonal and latitudinal variability of zonal, meridional and vertical winds respectively in presence of dust storm that occurred in MY 28. These wind distributions are represented at altitude 0 km, 10 km, 20 km, 40 km and 60 km in the troposphere of Mars. In absence of dust storm the seasonal and latitudinal variations of these winds are shown in figure 5.6 for MY 29. In both figures the winds are averaged over longitude. The zonal mean circulation exhibits change according to the seasonal cycle on Mars. The atmospheric winds represent seasonal variability due to formation of the polar ice caps on Mars (Pollack et al., 1979; Kuroda et al., 2008). It is found that the dust significantly affects mean meridional circulation in southern summer at low latitudes Unlike the Earth, a single cross-equatorial Hadley cell exists on Mars during northern hemisphere winter (Ls=270$^o$), which dominates in the subtropics (from southern summer hemisphere to northern winter hemisphere) and can extend to the extra-tropics (Read et al., 2015). This can be seen in meridional winds, increasing towards the northern hemisphere at higher altitudes, for example in figures 5.5(h-j) and 5.6(h-j), the winds are increasing from the southern near equatorial regions (a few m/s) towards the northern subtropics (10-20 m/s) (Medvedev et al*.,* 2011).

During the dust storm of MY28, the wind speed increased up to 40 m/s in comparison to that estimated to be 10 m/s in MY29. At 25$^o$S and Ls ~ 270$^o$, the meridional winds are blowing from south to north direction and changing slowly from 4 to 8 m/s between Ls = $0^o$ and $180^o$ at lower altitudes. The meridional circulation along with the rotation of the planet also creates strong zonal winds in southern tropical region at Ls ~ $270^o$. These strong winds near the surface can be seen in MY28 blowing from west to east (westerly) with speed ~ 20 m/s. In MY29 the westerly wind is reduced by about 5 m/s in this region. The westerly winds at altitude 10 km are estimated to be ~ 10 m/s and ~ 4m/s in MY28 and MY29 respectively. At high latitudes the zonal winds are higher in northern winter in comparison to northern summer and represent a strong westerly jet (Read et al., 2015). The zonal wind speeds in these jets can reach up to 120 m/s in northern hemisphere (upper right corner) and 80 m/s in southern hemisphere (lower left corner) (Barnes et al., 2017). The asymmetry between the jet strength in the two hemispheres may be due to combined effect of asymmetry in the topography and the dust distribution between the two hemispheres. The zonal winds in the southern hemisphere are highest up to 120 m/s in MY 28. In MY 29 these jets represent the increasing and decreasing slopes in northern and southern hemispheres respectively towards the pole (Mitchell et al., 2015). In MY 28 two symmetric jets have been found in northern winter.

It should be noted that westerly jets are less intense at the equinox as obtained by Lewis and Read (2003). The southern summer is dominated by easterly winds at high latitudes (figures 5.4c-e and 5.5c-e). Branes et al. (2017) have reported that the vertical shear of the zonal wind is proportional to the meridional gradient of the temperature and it blows easterly winds in the extra-tropics during the summer. At about 60 km the easterly zonal wind speeds up to 150 m/s in MY28 at Ls ~ 270 during the southern summer. In MY29 this wind is blowing with low speed of 80 m/s at the same location. Since the winds are averaged over longitudes we cannot study the tidal oscillations of longitudinal waves in figures 5.4 and 5.5. The vertical winds in the tropics are mostly in the upward direction at about all altitudes. In presence of dust storm these winds are highest up to 0.3 m/s in southern summer at Ls ~ 270$^{o}$ and latitude ~ 25$^{o}$S. As expected these vertical wind speeds in absence of dust storm were decreased at the same location by a factor of 3. The vertical wind speeds are below 0.05 m/s during the other seasons. It is found that the vertical winds are always high in the equatorial region than that obtained at mid and high latitudes.

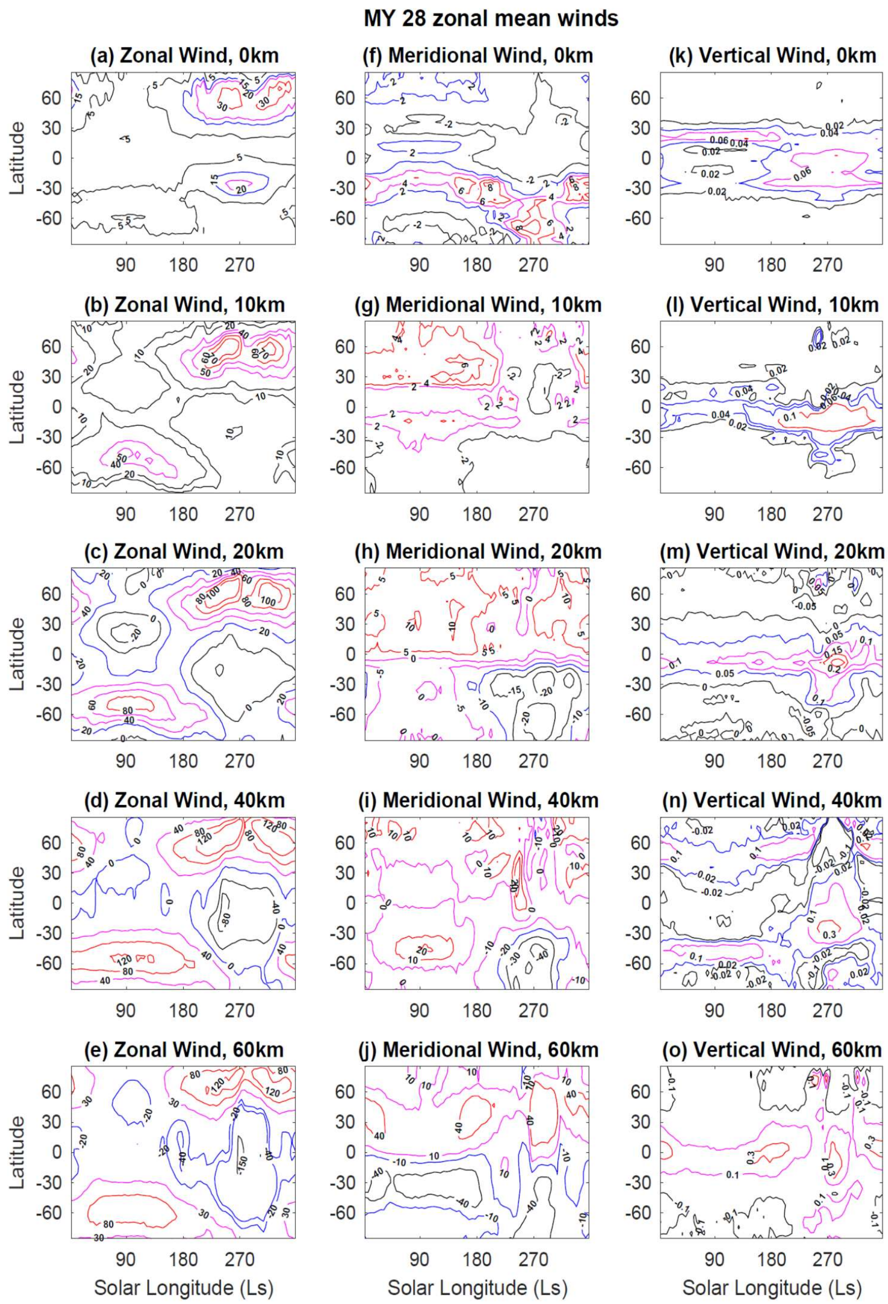


**Figure 5.4 The seasonal and latitudinal variability of zonally averaged zonal wind at (a) 0 km, (b) 10 km, (c) 20 km, (d) 40 km and (e) 60 km (left panel); meridional wind at (f) 0 km, (g) 10 km, (h) 20 km, (i) 40 km and (j) 60 km (middle panel), and vertical wind at (k) 0 km, (l) 10 km, (m) 20 km, (n) 40 km and (o) 60 km (right panel) for MY28.**

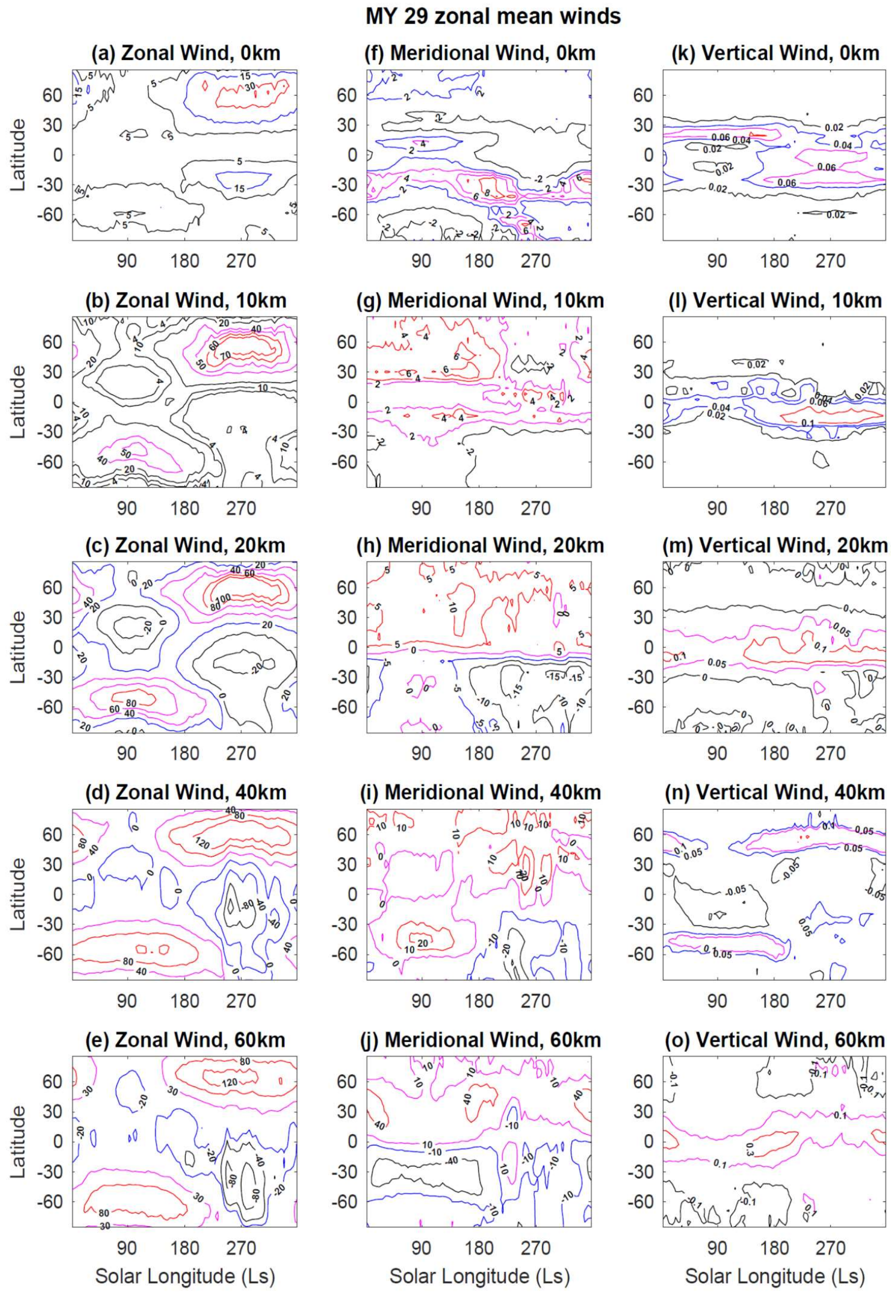


**Figure 5.5 Same seasonal and latitudinal variability of zonally averaged zonal, meridional and vertical winds as shown in figure 5.4 but for MY29.**

## 5.3.2 Altitude profiles of ozone heating rates at different latitudes

The figures 5.6 (a, b), 5.7 (a, b), 5.8 (a, b) and 5.9 (a, b) represent the altitude profiles of ozone heating rates in the daytime during MY28 at latitudes 2°N-S, 25°N-S, 45°N-S and 70°N-S respectively for Ls ~ 7.5°, 47.5°, 87.5°, 127.5°, 167.5°, 207.5°, 247.5°, 287.5° and 327.5°. We have not plotted these profiles for MY29 because the ozone heating rates in the daytime are nearly the same as MY28. At low and mid-latitudes (2°N-S, 25°N-S and 45°N-S) daytime ozone heating rates increased up to Ls ~ 47.5° with maximum value of ~ 0.65 K/day. Afterwards it decreased up to Ls ~ 127.5° and almost disappeared between Ls ~ 167.5° and 327.5°. The clear peaks are found in these profiles between altitudes 30 km and 50 km. It should be noted that the SPICAM has observed a broad ozone layer in southern polar night at 40-60 km. This layer is not observed at northern pole (Lebonnois et al., 2006). Montmession and Lefevre (2013) suggested that this layer is produced due to atmospheric circulation that creates distinct oxygen emission in the southern polar night. This circulation is formed due to huge Hadley cell in which warmer air rises and travels pole-ward before cooling and sinking at higher latitudes. The oxygen atoms produced by photolysis of $CO_2$ in the upper layer of the Hadley cell recombine in the polar night to form molecular oxygen and ozone. Therefore, the nighttime concentration of southern polar ozone depends on the supply of oxygen and rate of destruction due to hydrogen radicals.

In figures 5.6 (a, b) and 5.7 (a, b) the ozone heating rates are higher in altitude at low latitudes 2°N-S and 25°N-S respectively but in figure 5.8 (a, b) it is lower in altitude at mid-latitude 45°N-S, particularly in southern region. In figures 5.9 (a, b) the clear peaks are not found in ozone heating rates at high latitude 70°N-S. At latitudes 45°N-S and 70°N-S the ozone heating rates on the surface of Mars are larger by about 2 orders of magnitude during northern winter due to condensation of $CO_2$ frost. At these latitudes the heating rates of the surface ozone are decreasing by about 2 orders of magnitude in southern summer due to sublimation of $CO_2$ frost. This is because polar caps are releasing water vapor, which destroys ozone during southern summer (Lefevre et al., 2008). The northern polar winter is very cool and this process does not occur there. At latitudes 2°N-S and 25°N-S the peak in heating rates can be obtained in both hemispheres between altitudes 30 km and 50 km at Ls ~ 7.5°, 47.5°, 87.5° and 127.5° due to photolysis of $O_2$ which attach with O and forms the $O_3$ layer (Lefevre et al., 2004). This layer is fully destroyed by the photodissociation of ozone. It is found that the peak heights of ozone heating rates are reduced by about 10-20 km at southern mid-latitudes in comparison to northern mid-latitudes. These peaks are not clearly seen in the ozone heating rates at high latitudes in all seasons of both hemispheres.

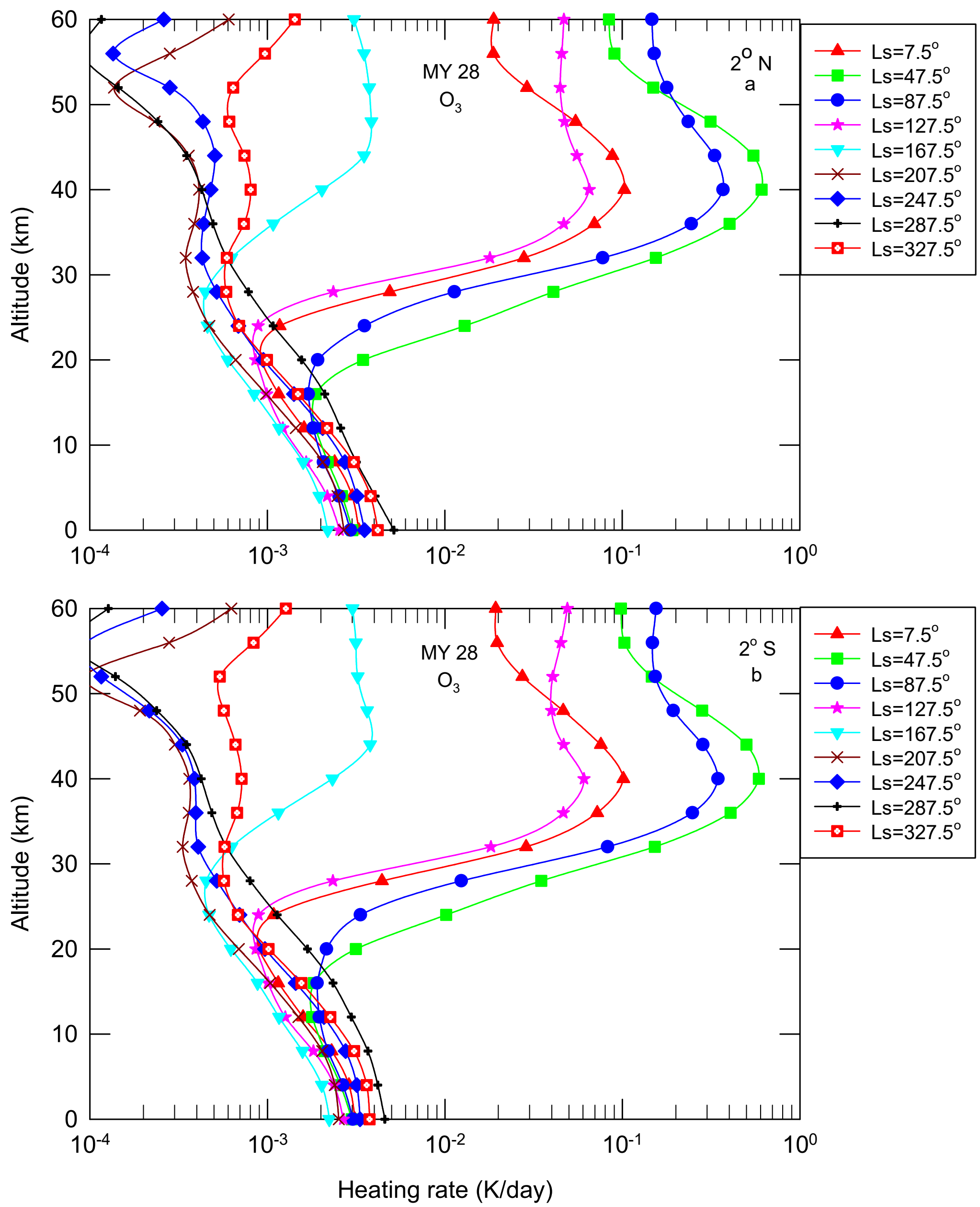


**Figure 5.6 The altitude profiles of the ozone heating rates in MY 28 at latitudes (a) 2ºN and (b 2ºS for Ls = 7.5º, 47.5º, 87.5º, 127.5º, 167.5º, 207.5º, 247.5º,287.5º and 327.5º.**

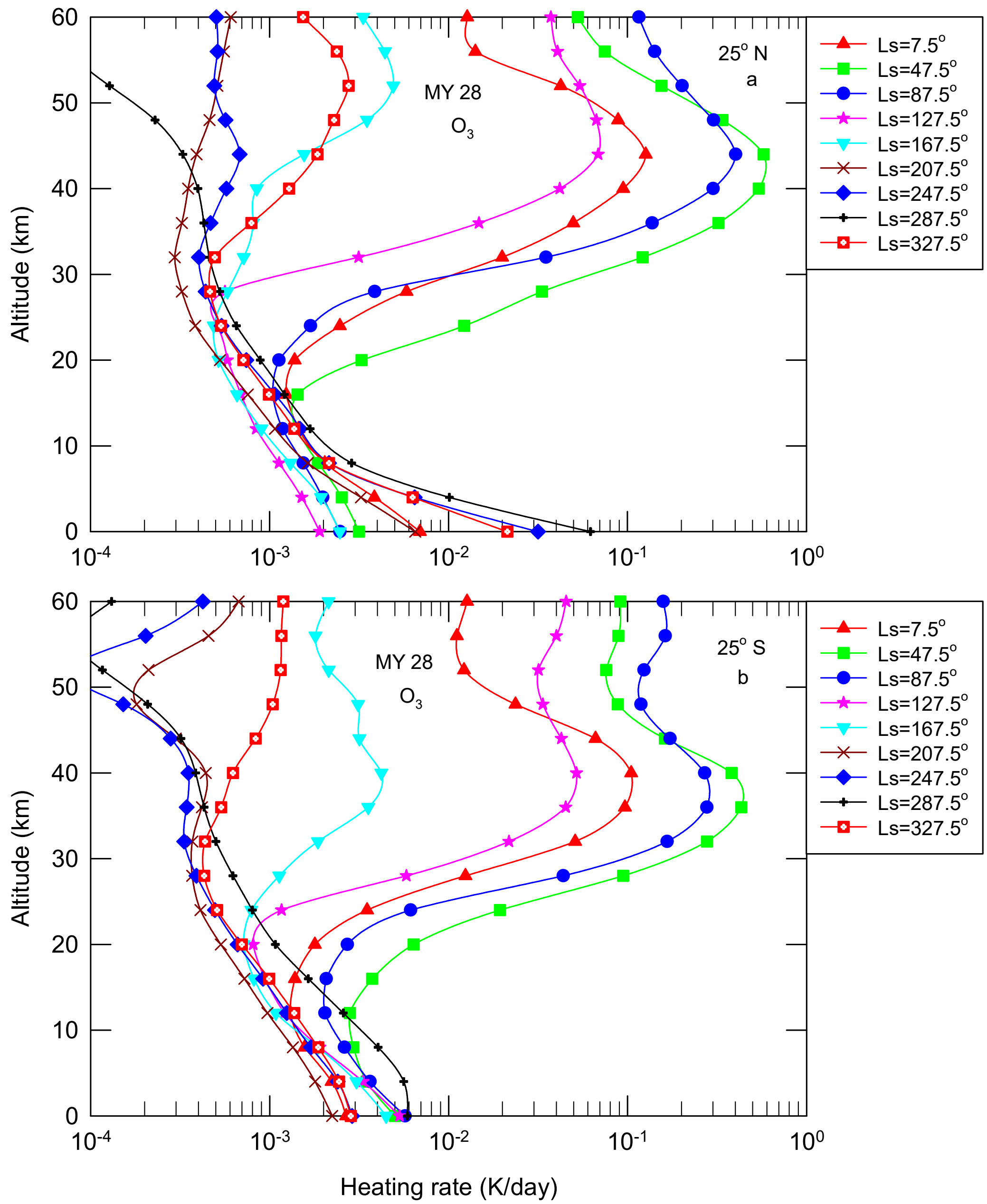


**Figure 5.7 Same as in figure 5.6 but for latitudes (a) 25ºN and (b) 25ºS.**

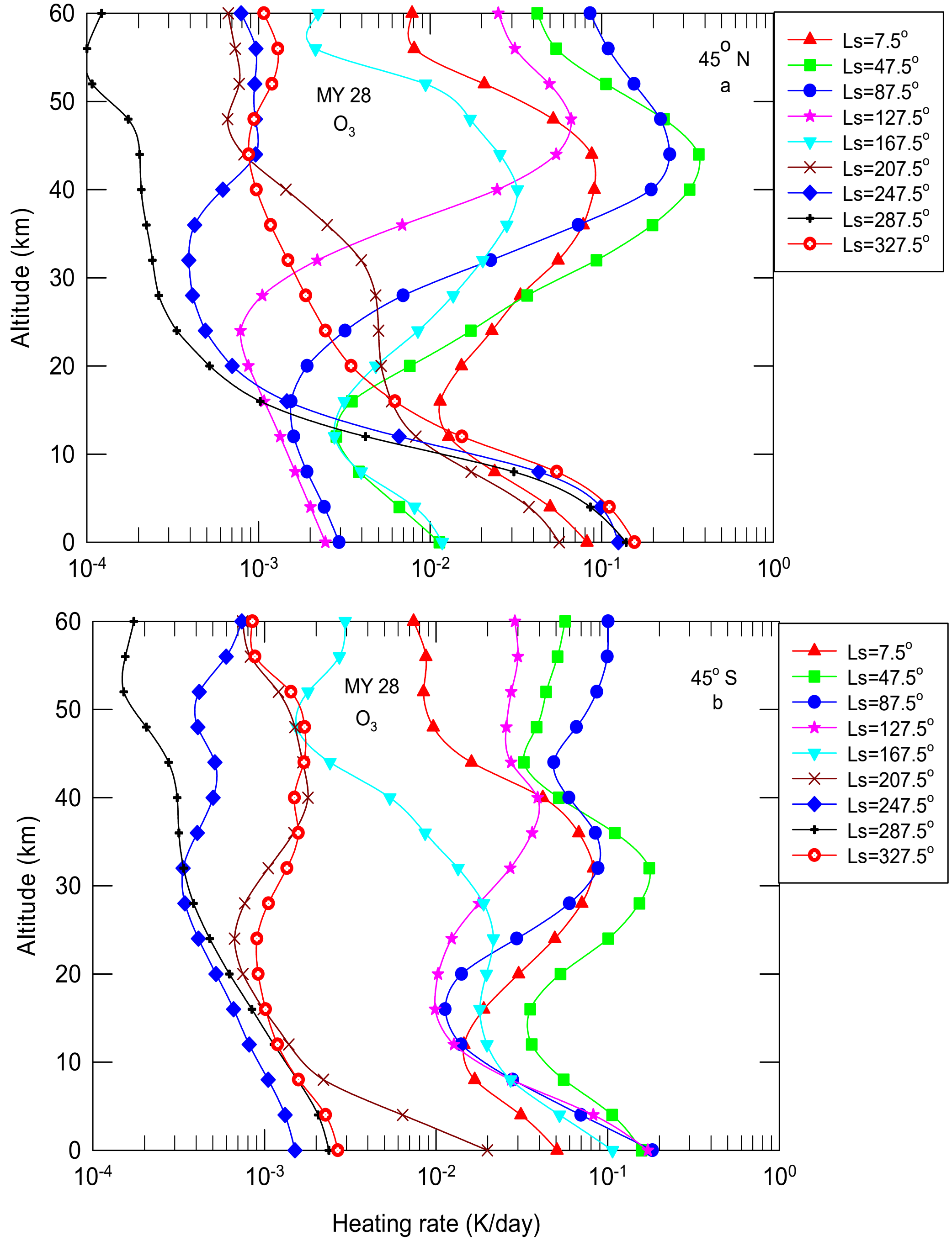


**Figure 5.8 Same as in figure 5.6 but for latitudes (a) 45°N and (b) 45°S.**

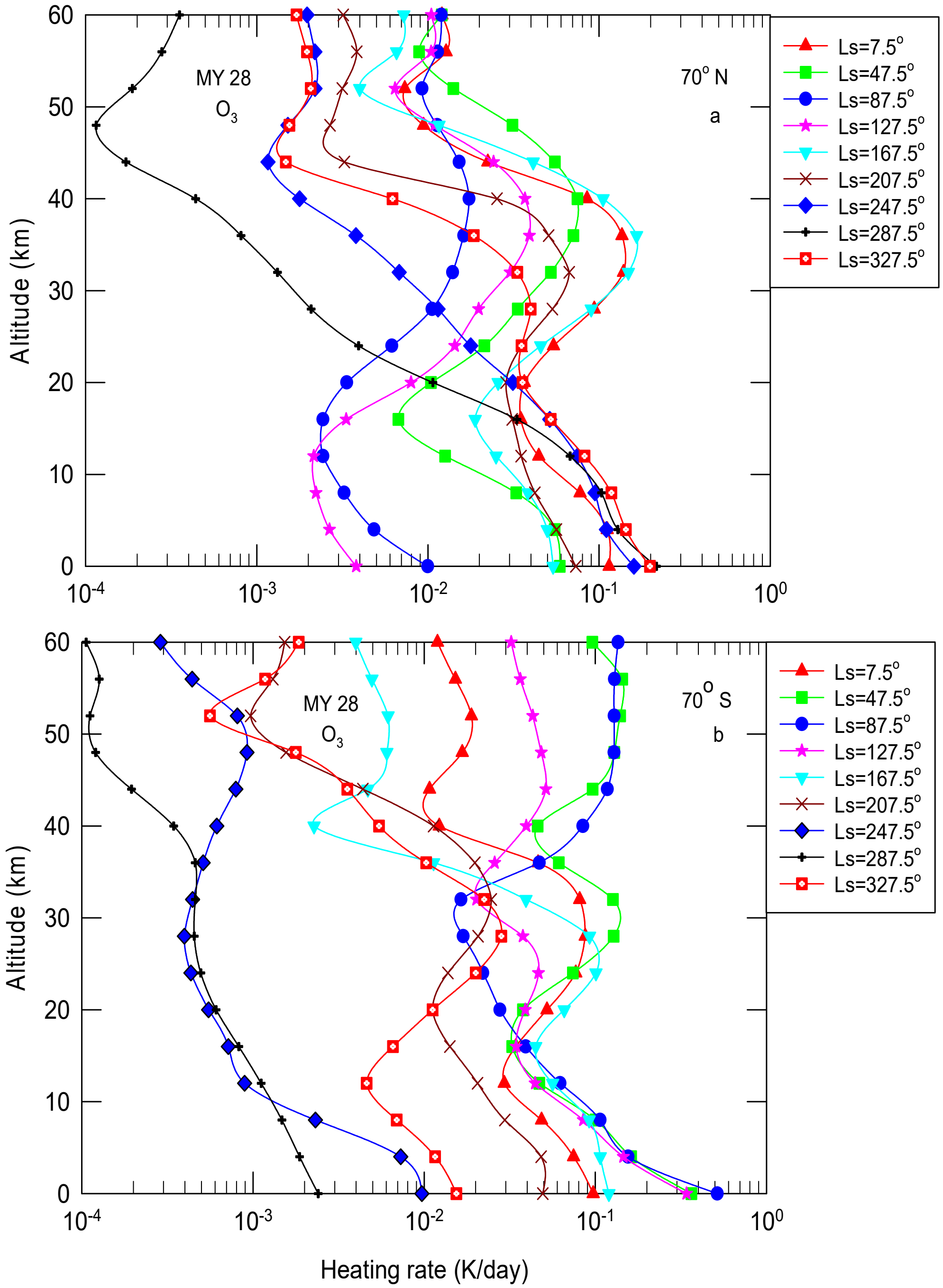


**Figure 5.9 Same as in figure 5.6 but for latitudes (a) 70ºN and (b) 70ºS.**

❒❒❒

# REFERENCES

Barnes, J. R., Haberle, R. M., Wilson, R. J., Lewis, S., Murphy, J. R., and Read, P. L. (2017). The global circulation.

Bertaux, J. L., Leblanc, F., Perrier, S., Quémerais, E., Korablev, O., Dimarellis, E., et al. (2005). Nightglow in the upper atmosphere of Mars and implications for atmospheric transport. Science, **307**(5709), 566-569.

Bertaux, J. L., Korablev, O., Perrier, S., Quemerais, E., Montmessin, F., Leblanc, F., et al. (2006). SPICAM on Mars Express: Observing modes and overview of UV spectrometer data and scientific results. Journal of Geophysical Research: Planets, **111**(E10).

Cavalié, T., Billebaud, F., Encrenaz, T., Dobrijevic, M., Brillet, J., Forget, F., and Lellouch, E. (2008). Vertical temperature profile and mesospheric winds retrieval on Mars from CO millimeter Observations-Comparison with general circulation model predictions. Astronomy & Astrophysics, **489**(2), 795-809.

Cox, C., A. Saglam, J.-C. Gérard, J.-L. Bertaux, F. Gonza´lez-Galindo, F. Leblanc, and Reberac, A. (2008). Distribution of the ultraviolet nitric oxide Martian night airglow: Observations from Mars Express and comparisons with a one-dimensional model. Journal of Geophysical Research: Planets, **113**(E8).

Cox, C., Gérard, J. C., Hubert, B., Bertaux, J. L., and Bougher, S. W. (2010). Mars ultraviolet dayglow variability: SPICAM observations and comparison with airglow model. Journal of Geophysical Research: Planets, **115**(E4).

Forget, F., Montmessin, F., Bertaux, J.-L., González-Galindo, F., Lebonnois, S., Quémerais, E., Reberac, A., Dimarells, E., and López-Valverde, M. A. (2009). Density and temperatures of the upper Martian atmosphere measured by stellar occultations with Mars Express SPICAM. Journal of Geophysical Research: Planets. **114**(E1), E01004.

Fox, J. L., and F. Hać, N. E. (2013). Intensities of the Martian N2 electron-impact excited dayglow emissions. Geophysical Research Letters, **40**(11), 2529-2533

González-Galindo, F., Forget, F., López-Valverde, M. A., Angelats i Coll, M., and Millour, E. (2009). A ground-to-exosphere Martian general circulation model: 1. Seasonal, diurnal, and solar cycle variation of thermospheric temperatures. Journal of Geophysical Research: Planets, **114**(E4).

Guzewich, S. D., Lemmon, M., Smith, C. L., Martínez, G., de Vicente-Retortillo, Á., Newman, C. E., et al. (2019). Mars Science Laboratory observations of the 2018/Mars year 34 global dust storm. Geophysical Research Letters, **46**(1), 71-79.

Guzewich, S. D., Smith, M. D., and Wolff, M. J. (2014). The vertical distribution of Martian aerosol particle size. Journal of Geophysical Research: Planets, **119**(12), 2694-2708.

Haider, S. A., Batista, I. S., Abdu, M. A., Muralikrishna, P., Shah, S. Y., and Kuroda, T. (2015). Dust storm and electron density in the equatorial D region ionosphere of Mars: Comparison with Earth's ionosphere from rocket measurements in Brazil. Journal of Geophysical Research: Space Physics, **120**(10), 8968-8977.

Haider, S. A., Siddhi, Y. S., Masoom, J., and Bougher, S. (2019). Effect of Dust Storm and GCR Impact on the Production Rate of O3+ in MY 28 and MY 29: Modeling and SPICAM Observation. Journal of Geophysical Research: Space Physics, **124**(3), 2271-2282.

Heavens, N. G., Johnson, M. S., Abdou, W. A., Kass, D. M., Kleinböhl, A., McCleese, D. J., et al. (2014). Seasonal and diurnal variability of detached dust layers in the tropical Martian atmosphere. Journal of Geophysical Research: Planets, **119**(8), 1748-1774.

Jain, S. K., and Bhardwaj, A. (2011). Model calculation of N2 Vegard-Kaplan band emissions in Martian dayglow. Journal of Geophysical Research: Planets, **116**(E7).

Kuroda, T., Medvedev, A. S., Hartogh, P., and Takahashi, M. (2008). Semiannual oscillations in the atmosphere of Mars. Geophysical Research Letters, **35**(23).

Leblanc, F., Chaufray, J. Y., and Bertaux, J. L. (2007). On Martian nitrogen dayglow emission observed by SPICAM UV spectrograph/Mars Express. Geophysical Research Letters, **34**(2).

Lebonnois, S., Quémerais, E., Montmessin, F., Lefèvre, F., Perrier, S., Bertaux, J. L., and Forget, F. (2006). Vertical distribution of ozone on Mars as measured by SPICAM/Mars Express using stellar occultations. Journal of Geophysical Research: Planets, **111**(E9).

Lefèvre, F., Lebonnois, S., Montmessin, F., and Forget, F. (2004). Three-dimensional modeling of ozone on Mars. Journal of Geophysical Research: Planets, **109**(E7).

Lefèvre, F., Bertaux, J. L., Clancy, R. T., Encrenaz, T., Fast, K., Forget, F., et al. (2008). Heterogeneous chemistry in the atmosphere of Mars. Nature, **454**(7207), 971.

Lewis, S. R., and Read, P. L. (2003). Equatorial jets in the dusty Martian atmosphere. Journal of Geophysical Research: Planets, **108**(E4).

Liu, G., England, S. L., Lillis, R. J., Withers, P., Mahaffy, P. R., Rowland, D. E., et al. (2018). Thermospheric expansion associated with dust increase in the lower atmosphere on Mars observed by MAVEN/NGIMS. Geophysical Research Letters, **45**(7), 2901-2910.

Martin, T. Z. (1995). Mass of dust in the Martian atmosphere. Journal of Geophysical Research: Planets, **100**(E4), 7509-7512.

Medvedev, A. S., Kuroda, T., and Hartogh, P. (2011). Influence of dust on the dynamics of the Martian atmosphere above the first scale height. Aeolian Research, **3**(2), 145-156.

Millour, E., et al. 2014 A new Mars climate database v5.1, paper 1301 presented at The Fifth International Workshop on Mars Atmosphere: Modeling and Observations, Oxford, U. K., Jan. 2014.

Mischna, M. A., Lee, C., and Richardson, M. (2012). Development of a fast, accurate radiative transfer model for the Martian atmosphere, past and present. Journal of Geophysical Research: Planets, **117**(E10).

Mitchell, D. M., Gray, L. J., Fujiwara, M., Hibino, T., Anstey, J. A., Ebisuzaki, W., et al. (2015). Signatures of naturally induced variability in the atmosphere using multiple reanalysis datasets. Quarterly Journal of the Royal Meteorological Society, **141**(691), 2011-2031.

Montmessin, F., and Lefèvre, F. (2013). Transport-driven formation of a polar ozone layer on Mars. Nature Geoscience, **6**(11), 930.

Montmessin, F., Korablev, O., Lefèvre, F., Bertaux, J. L., Fedorova, A., Trokhimovskiy, A., et al. (2017). SPICAM on Mars Express: a 10 year in-depth survey of the Martian atmosphere. Icarus, **297**, 195-216.

Pollack, J. B., Colburn, D. S., Flasar, F. M., Kahn, R., Carlston, C. E., and Pidek, D. (1979). Properties and effects of dust particles suspended in the Martian atmosphere. Journal of Geophysical Research: Solid Earth, **84**(B6), 2929-2945.

Read, P. L., Lewis, S. R., and Mulholland, D. P. (2015). The physics of Martian weather and climate: a review. Reports on Progress in Physics, **78**(12), 125901.

Serdyuchenko, A., Gorshelev, V., Weber, M., Chehade, W., and Burrows, J. P. (2014). High spectral resolution ozone absorption cross-sections-Part 2: Temperature dependence. Atmospheric Measurement Techniques, **7**(2), 625-636.

Sheel, V., and Haider, S. A. (2016). Long-term variability of dust optical depths on Mars during MY24-MY32 and their impact on subtropical lower ionosphere: Climatology, modeling, and observations. Journal of Geophysical Research: Space Physics, **121**(8), 8038-8054.

Tobiska, W. K., Woods, T., Eparvier, F., Viereck, R., Floyd, L., Bouwer, D., et al. (2000). The SOLAR2000 empirical solar irradiance model and forecast tool. Journal of Atmospheric and Solar-Terrestrial Physics, **62**(14), 1233-1250.

Wang, B., and Lee, S. S. (2017). MJO propagation shaped by zonal asymmetric structures: Results from 24 GCM simulations. Journal of Climate, **30**(19), 7933-7952.

Willame, Y., Vandaele, A. C., Depiesse, C., Lefèvre, F., Letocart, V., Gillotay, D., and Montmessin, F. (2017). Retrieving cloud, dust and ozone abundances in the Martian atmosphere using SPICAM/UV nadir spectra. Planetary and Space Science, **142**, 9-25.

Wilson, S. A., Grant, J. A., Howard, A. D., and Buczkowski, D. L. (2018). The nature and origin of deposits in Uzboi Vallis on Mars. Journal of Geophysical Research: Planets, **123**(7), 1842-1862.

Zalucha, A. M., Plumb, R. A., and Wilson, R. J. (2010). An analysis of the effect of topography on the Martian Hadley cells. Journal of the Atmospheric Sciences, **67**(3), 673-693.

❒❒❒

# CHAPTER - 6

# MODELING AND OBSERVATION OF DIFFUSE AURORA IN THE NIGHTTIME ATMOSPHERE OF MARS

# CONTENTS

*The nighttime limb intensity of diffuse auroral emission of $CO_2^+$ ($B^2\Sigma_u^+$ - $X^2\pi_g$) UVD is observed in northern hemisphere of Mars during 17-21 December, 2014 from IUVS instrument onboard MAVEN. We have used hybrid model and four dimensional yield spectrum approach based on Monte Carlo simulation to calculate the ionization rate, limb intensity, ion and electron densities of diffuse aurora due to precipitation of SEP and $H^+$-H fluxes in the nighttime ionosphere of Mars. It is found that the production rates of atmospheric ions ($CO_2^+$, $N_2^+$ and $O^+$) are dominant in the upper ionosphere at about 100-150 km due to impact of $H^+$-H. The SEP formed auroral ionosphere ($CO_2^+$, $NO^+$ and $O^+$) in the middle ionosphere between 50 km and 100 km due to precipitation of monoenergetic electrons of energies 25 to 100 keV. The simulated limb intensities of $CO_2^+$UVD due to impact of $H^+$-H and auroral electrons are compared with IUVS observations. Our model results are overestimating the observations but 100 keV electrons deposited maximum energy around 75 km, closer to the observed altitude of the maximum emission. The densities of upper ionosphere ($O_2^+$, $NO^+$, and $CO_2^+$) due to impact of $H^+$-H are smaller by 1-2 orders of magnitude than that produced by auroral electrons in the middle ionosphere.*

# 6.1 INTRODUCTION

Aurora occurs both on Earth and Mars, when energetic particles impact on their atmospheres. On Earth, these particles are moving towards the poles along the global magnetic field lines (McIlwain, 1960). On Mars, there is no planetary magnetic field to guide the particles north and south. Three kinds of aurora (1) discrete aurora (2) proton aurora and (3) diffuse aurora have been detected on Mars from IUVS instrument (Schneider et al., 2015). The discrete aurora (Bertaux et al., 2005) has been observed near the crustal magnetic field lines in southern hemisphere of Mars. This aurora is produced in the nighttime atmosphere due to precipitation of energetic electrons. The proton aurora (Deighan et al., 2018) is observed in the daytime due to energetic proton precipitation into the Martian atmosphere. During this event Lyman-α limb profiles are enhanced at altitude between 120 and 150 km. The diffuse aurora (Schneider et al., 2015) is observed in the nighttime due to precipitation of SEP electrons down up to 1 microbar altitude. This aurora is neither restricted to location nor linked to the magnetic field. It is globally distributed and is closely correlated to solar wind velocity. Previously, there are several studies which calculated theoretical intensity for ultraviolet doublet (B-X) of $CO_2$ (Stewart, 1972; Mantas and Hanson, 1979; Fox and Dalgarno, 1979; Fox, 1991). Recently Gérard et al. (2017) have used incident flux ~ 1 $mWm^{-2}$ at the top of the atmosphere and calculated limb intensity profiles of $CO_2^+$ UVD band for comparison with IUVS observations. They found that electrons of 50-200 keV can produce the observed peak limb intensity of diffuse aurora.

### 6.1.1 SEP electron spectrum

The major disturbances happen in the solar system's heliosphere due to SEP events. Due to SEP events, the electron and the proton fluxes are enhanced significantly. There are mainly two types of SEP namely impulsive and gradual events, which are accelerated by solar X-ray flares and CMEs respectively (Cane et al., 1986). Impulsive events are relatively of short duration (< 1 day) while gradual events are of longer duration (days). There have been several efforts to describe the interaction of SEPs with the Mars' atmosphere. Initially Leblanc et al. (2002) carried out the theoretical the altitude profiles of energy deposition rate in the Martian ionosphere due to SEP impact on 20 October, 1995. Later Mars Advanced Radar for Subsurface and Ionosphere Sounding (MARSIS) experiment onboard Mars Express observed that the electron densities were increased significantly in the upper ionosphere of Mars during SEP events (Morgan et al., 2006). ESA and NASA have developed a Mars Energetic Radiation Environment model to study the effects of SEP radiation around Mars (cf. McKenna-Lawlor et al., 2012). Sheel et al. (2012) investigated the response of SEP event of 29 September, 1989 at Mars. They found that SEP event enhanced the electron density by a factor of ~ 2-3 than that observed by MGS in the dayside ionosphere of Mars at altitude range 120-140 km. MAVEN has been making regular observations of the response of Mars to CME since November 2014. Six significant CME events have been detected by MAVEN during

15-23 December, 2014, 25-27 March, 5-7 May, 28 October - 9 November, 2015, 6-9 January, 2016 and 10-23 September, 2017 (Jakosky et al., 2015; Lee et al., 2017; Ramstad et al., 2018). The diffuse auroras were observed by MAVEN in two major SEP events that occurred during 15 - 23 December, 2014 and 11-14 September, 2017 (Schneider et al., 2015, 2018).

The figures 6.1(a-d) shows the time series of electron spectra at energies 25 keV, 50 keV, 75 keV, and 100 keV, observed by Solar Energetic Particle instrument onboard MAVEN from 15 to 23 December, 2014. During this period, MAVEN completed 48 periapse passes between orbits # 408 to # 456. We have shown the SEP observations without averaging over the orbit (thus all the data of periapsis pass are plotted for every orbit). The solid red line represents smooth fitting obtained from 'Smooth Data Moving Average Filter' technique (https://mathworks.com/help/curvefit/smooth.html/). The smoothed data clearly shows the enhancement in the electron fluxes of 25 keV, 50 keV, 75 keV, and 100 keV. The large enhancements in SEP electron spectra have been observed between 17 and 21 December, 2014 when diffuse auroras were observed by IUVS instrument. These spectra observed maximum electron fluxes ~ $2.4 \times 10^4$, $1.3 \times 10^4$, $7.0 \times 10^3$ and $5.1 \times 10^3$ $cm^{-2}$ $s^{-1}$ $sr^{-1}$ at energies 25 keV, 50 keV, 75 keV and 100 keV respectively. The SEP peak electron fluxes are decreasing with increasing energy. We have used these fluxes in our calculation.

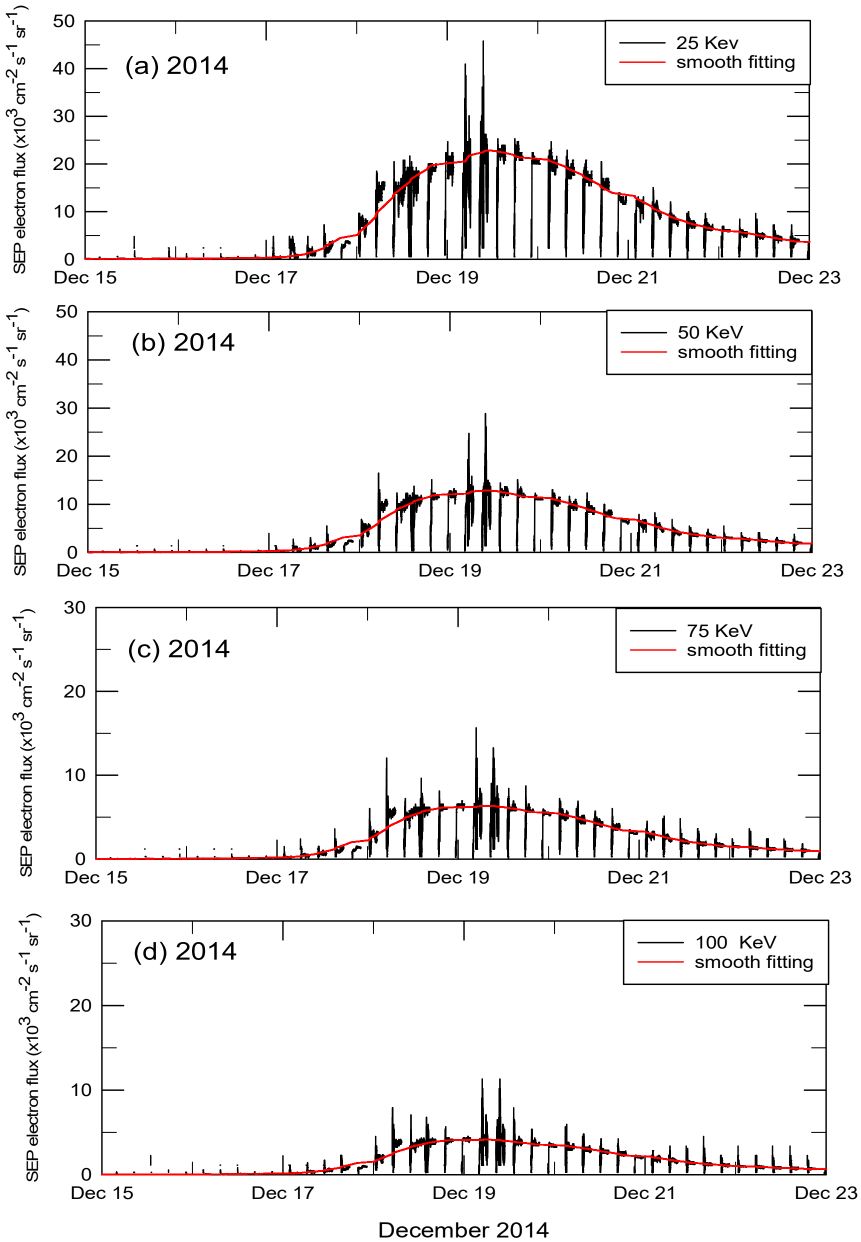


**Figure 6.1 A time series of SEP electron fluxes at energies 25 keV (a), 50 keV (b), 75 keV (c) and 100 keV (d) as observed by SEP instrument onboard MAVEN during 15-23 December, 2014.**

## 6.1.2 MAVEN/IUVS Observations

In this chapter, we have calculated ion production rates, its limb intensity, along with ion and electron densities on 19 December, 2014. We have considered the precipitation of $H^+$-H and SEP electrons as a source in the nighttime ionosphere of Mars. The limb intensity of $CO_2^+$ UVD is observed in the nighttime diffuse aurora that occurred at 17 periapsis during orbit # 418- 444 of MAVEN from 17 to 21 December, 2014 at latitude ~ 35°N spanning nearly at all longitudes (Schneider et al., 2015). The SEP electron spectra have been measured from MAVEN between energy range from 25 keV to 200 keV (https://pds-ppi.igpp.ucla.edu) (Larson et al., 2015). Mars does not have a dipole magnetosphere as on Earth. In absence of dipole magnetosphere, the solar wind carries magnetic field lines from the sun. As magnetic field lines cannot pass through electrically conducting objects (like Mars), they drape themselves around the planet creating an induced magnetosphere (as shown in Figure 6.1) even if the planet does not necessarily have a global magnetic field. These draped field lines allow $H^+$-H and SEP electrons to penetrate deeper into the nighttime atmosphere of Mars during solar storms. We have carried out modeling of diffuse aurora due to impact of these particles by using four dimensional yield spectrum and hybrid model (Singhal et al., 1980; Haider and Singhal, 1983; Bhardwaj et al., 1995; Kallio and Janhunen, 2001; Haider et al., 2002, 2009, 2011). In this model six gases ($CO_2$, $N_2$, $O_2$, CO, O and He) are taken from Mars MCD V5.2 (Millour et al., 2014). There is a reasonable agreement between our calculation and IUVS limb observation at altitude range 100 to 150 km due to precipitation of $H^+$-H. The calculated limb intensity is overestimated by a factor of 2-10 than the observations at altitude range ~ 50 to 100 km.

## 6.2 MODELING TOOLS

In this chapter we have considered a four dimensional AYS method based on Monte Carlo approach (Singhal et al., 1980; Haider and Singhal, 1983; Bhardwaj et al., 1995). In this method SEP electrons of different incident energies $E_o$ were introduced at the top of the atmosphere. These electrons are precipitating down into the nighttime atmosphere along the IMF lines at some pitch angle. The IMF field lines are draped through the atmosphere of Mars in absence of dipole magnetosphere. The four dimensional AYS method is described in chapter in section 2.3.1. We have also used hybrid model for studying the effect of precipitating $H^+$-H flux into the nighttime atmosphere of Mars (Kallio and Janhunen, 2001, Haider et al., 2002, 2009, 2011). In this model $H^+$ ions are accelerated up to energies 10 keV in presence of electric and magnetic fields. In absence of dipole magnetic field, an interplanetary shock compresses the magnetosheath of Mars. The Magnetosheath contains the planetary neutrals, mostly H atoms of hydrogen corona. The ENAs are formed by charge exchange reaction between solar wind protons and hydrogen corona. Thus, an ENA is produced from $H^+$ and H (Galli et al., 2008) and are represented as $H^+$-H. Recently, Analyzer of Space Plasmas and Energetic Atoms (ASPERA) experiment onboard MEX observed ENAs in the nightside of Mars from (Galli et al., 2006, 2008; Milillo et al., 2009). As discussed in chapters 2, the hybrid model is used for the calculation of the ion production rates of $CO_2^+$, $N_2^+$ and $O^+$ due to precipitation of $H^+$-H into the nightside ionosphere of Mars.

## 6.2.1 $H^+$-H flux spectra

We have estimated $H^+$-H flux ~1.0 x $10^6$ $cm^{-2}$ $s^{-1}$ in the nighttime ionosphere of Mars by using the hybrid model. These fluxes are precipitating into the nightside atmosphere of Mars. Recently, the brightest proton aurora was detected in the dayside atmosphere of Mars from the IUVS and SPICAM instrument on board MAVEN and MEX respectively due to precipitation of proton flux ~1-3 x $10^6$ $cm^{-2}$ $s^{-1}$ (Deighan et al., 2018; Ritter et al., 2018). The brightest diffuse aurora is also observed during September 11-14, 2017 due to precipitation of SEP electron flux ~ 1.29 x $10^6$ $cm^{-2}$ $s^{-1}$ of nearly same magnitude in the nighttime atmosphere of Mars (Schneider et al., 2018). Therefore, our estimated $H^+$-H flux ~ 1.0 x $10^6$ $cm^{-2}$ $s^{-1}$ is in good agreement with the observed electron/proton fluxes producing bright auroras on Mars. The atmospheric effects of $H^+$-H precipitation in the night side ionosphere of Mars was included in the hybrid model by Kallio and Barabash (2001) using the Monte Carlo simulation.

The hybrid model includes 6 elastic and 24 inelastic collision processes (ionization, electron stripping, charge exchange, Lyman alpha (Lα) and Balmer alpha (Hα) between energy 10 eV and 10 keV for the impact ionizations of $H^+$-H with atmospheric neutrals $CO_2$, $N_2$, and O. The elastic cross sections due to proton and hydrogen impact on $CO_2$, $N_2$ and O are calculated by Rudd et al. (1995). The inelastic cross sections due to $H^+$ and H impact ionizations, electron stripping, charge exchange, Lyman and Balmer alpha emissions are also calculated by these authors. These cross sections have been used in this model and were compiled in the Appendix by Haider et al. (2002). The energy losses and the number of collisions are recorded into different matrices, which produce ion production rates at different SZA. The grid size of altitude and SZA are taken as 2.5 km and 15° respectively (Kallio and

Janhunen, 2001). The atmospheric effects of $H^+$-H precipitation depend on the incident flux ~ 1.0 x $10^6$ $cm^{-2}$ $s^{-1}$. We have used this flux to calculate the production rates of $CO_2^+$, $N_2^+$ and $O^+$ in the nighttime ionosphere of Mars at SZA 105° and 127°. In presence of large incident flux, the ion production rates will increase. Therefore, the production rates will be high during medium and high solar activity. These calculations are performed by hybrid model at solar minimum condition when the solar wind velocity, the IMF field and the density were observed as 400 km/s, 3 nT and 2.5 $cm^{-3}$ respectively (Haider and Masoom, 2019). These plasma parameters are closely matching with the observations carried out by SWIA instrument on board MAVEN during SEP events of December 2014, when diffuse aurora occurred in the nighttime atmosphere of Mars during 17 to 21 December, 2014.

### 6.2.2 Limitations of models

The hybrid model has some limitations in computing $H^+$-H precipitation into the nighttime atmosphere of Mars. These limitations are given as (1) the $H^+$-H impact ionization depends on various elastic and inelastic cross sections which are taken from various investigators. These cross sections used by various investigators are not consistent with each other and a factor of 2-3 variations can be seen among the values used. Therefore, the results are uncertain by a factor of ~ 2 depending upon the cross sections obtained from the models or observations (Kallio and Barabash, 2001), (2) Monte Carlo code is not self-consistent because the electromagnetic field in this model is derived from an empirical or analytical model (Kallio et al., 1994), and (3) the hybrid approach assumes mass less electrons. Therefore, this approach cannot describe electron gyroradius effects that may play role at cross tail current sheet. The advantage of the hybrid model is that it includes kinetic effects of ions, wave particle interactions, and instabilities associated with the non-Maxwellian velocity distribution function.

We have used two sources of ionizations viz. (1) SEP electron impact and (2) $H^+$-H impact ionizations in the calculations of the production rates of $CO_2^+$, $N_2^+$ and $O^+$. These production rates are used in the steady state coupled chemical model to calculate the altitude profiles of ions and electron density in the nighttime ionosphere of Mars between altitudes 50 km and 200 km. The electron density, $\mathbf{n_e}$ is calculated as $n_e = \Sigma n_i^+$, where $\Sigma n_i^+$ is the sum of all ion densities. Using charge neutrality and steady state conditions the electron density $n_e$ is obtained by iteration process. The chemical reactions, ion and electron temperatures for the calculation of the ion and electron densities are taken from Haider et al. (2013). The steady state conditions are valid up to ~ 200 km because the chemical life time is much lower than the transport time in this region. The limb intensity of $CO_2^+$ UVD is also calculated due to two sources of ionizations. These estimated results can change if the cross sections are changing in future.

### 6.2.3 Nightglow auroral emission

The nightglow limb intensity I(h) of $CO_2^+$ UVD is estimated by integration the ion production rates along the horizontal direction X as follows:

$$I(h) = 2\int_0^\infty P_{ki}\left(\sqrt{X^2 + (r+h)^2} - r\right)dX \tag{6.1}$$

where $\mathbf{r}$ = 3390 km is the radius of Mars and $P_{ki}\left(\sqrt{X^2 + (r+h)^2} - r\right)$ is the total production rate (SEP electron + $H^+$-H impact ionization) of $CO_2^+$ in horizontal direction $\mathbf{X}$. The production rate $P_{ki}$ is integrated over a very small interval of 2 km in horizontal direction. The horizontal distance X is varying from 0 km to 220 km at each altitude **h**, which is a vertical height and is varying from 50 to 200 km at interval of 2 km.

## 6.3 INDUCED MAGNETOSPHERE

In absence of dipole magnetosphere on Mars, bow shock and magnetosheath acts as an obstacle to the solar wind. In order to reach the ionosphere, the solar wind has to cross these barriers. From the MGS electron reflectometer and magnetometer measurements, it has been observed that the Magnetosheath of Mars is at altitude ~ 435 km on the sunlit hemisphere during quiet condition (Mitchell et al., 2000). There's an imaginary boundary between magnetosheath and ionosphere known as "Ionopause". In Figure 6.2 the solar wind IMF field lines are draped around Mars in absence of dipole magnetosphere. The IMF field lines are connected to the planet at both ends. The $H^+$-H and SEP electrons are precipitating in to nighttime ionosphere along the open field lines. In this figure the mini-magnetosphere is located at southern mid-latitudes where discrete aurora occurred in presence of crustal fields (Bertaux et al., 2005). The solar wind accelerated particles of sufficient energies (~ 100 eV) enter into the mini-magnetosphere and cause discrete auroras.

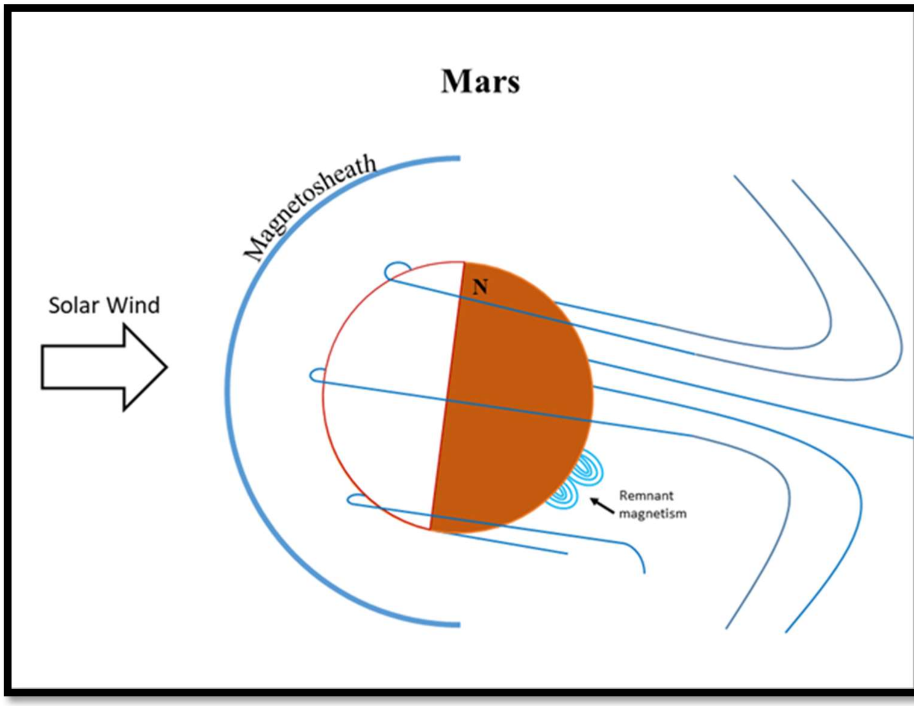


**Figure 6.2 Schematic diagram of IMF field lines around Mars (Schneider et al., 2015). The SEP electrons can enter into the atmosphere of Mars along these IMF field lines.**

## 6.3.1 Solar wind parameters

The figure 6.3 represents a time series of orbit averaged solar wind plasma parameters obtained from two different instrument viz. Solar Wind Plasma Analyzer (SWIA) and Magnetometer (MAG) between 15 and 23 December, 2014 (Lee et al., 2017). Figure 6.3a shows that concurrent IMF fields, changing at about 22:40 UT on 17 December, 2014 from anti-sunward to sunward directions at $\varphi = 120^o$ to $\varphi = 300^o$ respectively. Around the same time magnetic field components also rotated from $-B_x$, $+B_y$ to $+B_x$, $-B_y$ (see figure 6.3d). The angle (theta) is nearly zero when the magnetic fields are rotating from x to y components. This confirmed that the heliospheric current sheets (HCS) were crossing at this time. After HCS crossings SWIA observed a peak density ~ 15 $cm^{-3}$ and peak pressure 2.5 nPa at about 02:00 UT on 18

December, 2014. The total IMF fields and solar wind speed also increased up to ~ 9 nT and ~390 km/s respectively between December 18 to 21, 2014. It should be noted that after SEP events, the solar wind plasma and IMF values reaches back to their background levels. These solar wind parameters are important to understand the auroral formation in the Martian environment. Aurora occurs during disturbed conditions when SEP events occurred. During auroral events the solar wind velocity increased up to ~ 400 km/s. The solar wind density was also increased up to ~10 $cm^{-3}$.

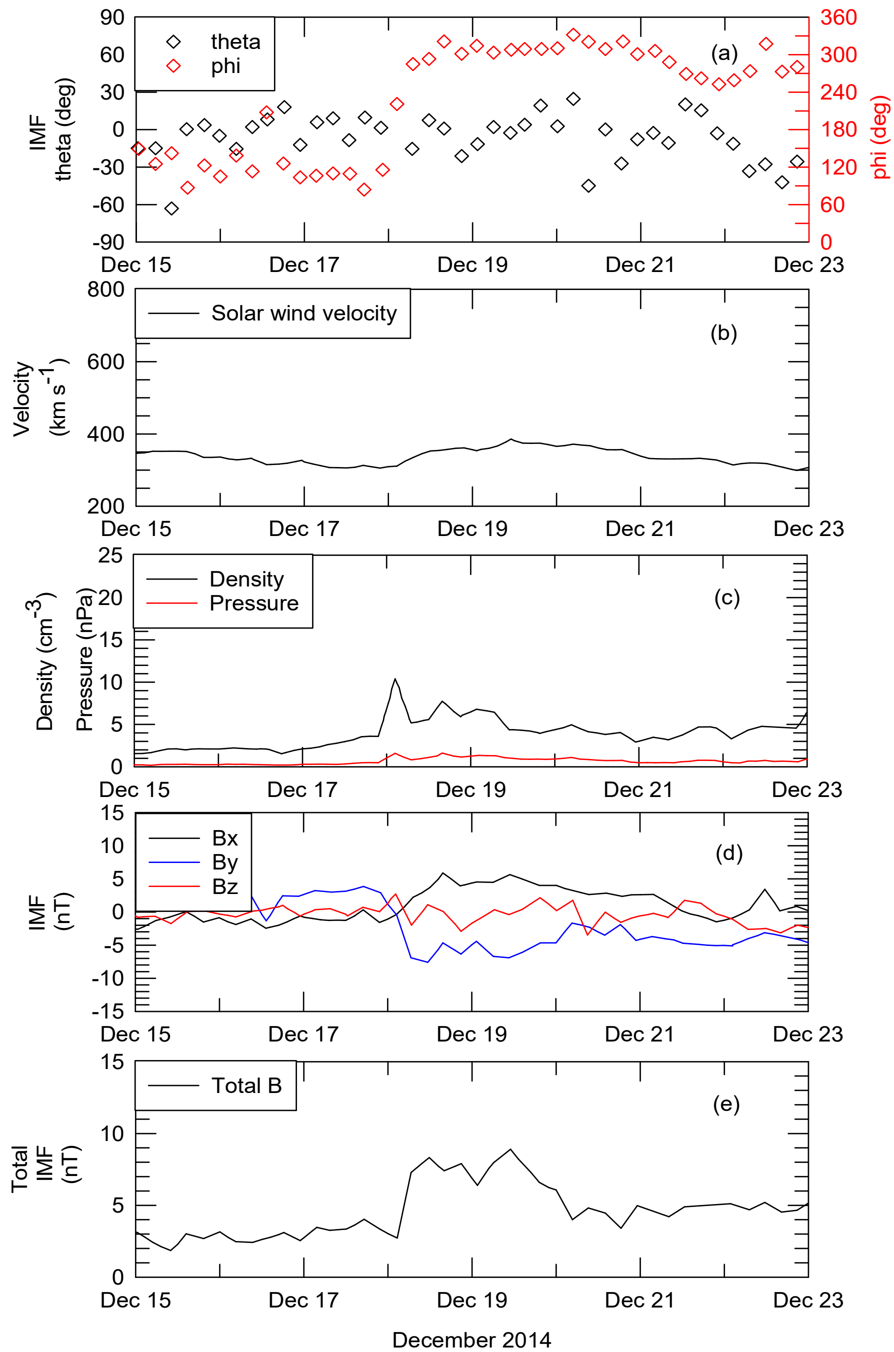


**Figure 6.3 The orbit average solar wind plasma parameters between 15 and 23 December, 2014. First top panel: (a) IMF field directions, theta and phi in degrees; Second panel: (b) solar wind velocity in km/s; Third panel: (c) density and pressure in $cm^{-3}$ and nPa respectively; Fourth panel: (d) IMF field components $B_x$, $B_y$ and $B_z$; Fifth panel: (e) Total IMF field (c.f. Lee et al., 2017).**

## 6.3.2 Ion production rates

We have calculated sixteen altitude profiles of ion production rates of $CO_2^+$ due to precipitation of auroral electrons of energies between 25 keV and 100 keV at 5 keV intervals in the nighttime ionosphere of Mars. In figure 6.4 we have plotted only four profiles of these production rates due to impact of SEP electron fluxes 2.4 x $10^4$, 1.3 x $10^4$, 7.0 x $10^3$ and 5.1 x $10^3$ $cm^{-2}$ $s^{-1}$ $sr^{-1}$ at energies 25 keV, 50 keV, 75 keV, and 100 keV respectively. The peak heights and peak production rates are varying with incident SEP electron fluxes. The peak production rates of $CO_2^+$ occurs at altitudes 100 km, 85 km, 80 km and 75 km due to impact of 25 keV, 50 keV, 75 keV and 100 keV respectively. It is found that the highest energy 100 keV is penetrating deep into the Mars' atmosphere up to ~ 75 km where MAVEN observed nighttime auroral emissions for 5 days continuously. In figure 6.5 we have compared ion production rates of three major ions $CO_2^+$, $N_2^+$, and $O^+$ in the nighttime ionosphere of Mars due to impact of SEP electrons (of energy 100 keV) and $H^+$-H fluxes at SZA 105$^o$ and 127$^o$ respectively. The $H^+$-H impact ionization rates are decreasing with increasing SZA. The upper ionosphere of Mars is formed between altitudes 100 km and 200 km due to $H^+$-H impact ionizations. The auroral ionosphere is formed in the middle ionosphere of Mars due to impact of SEP electrons between altitudes 50 km and 100 km. The auroral ion production rates are greater by 1-2 orders of magnitude than that produced by $H^+$-H impact ionizations. The ion production rates of $CO_2^+$, $N_2^+$ and $O^+$ are proportional to their neutral densities around the peak altitude. In figures 6.4 and 6.5 the production rate of $CO_2^+$ is maximum because $CO_2$ is a major gas in the atmosphere of Mars.

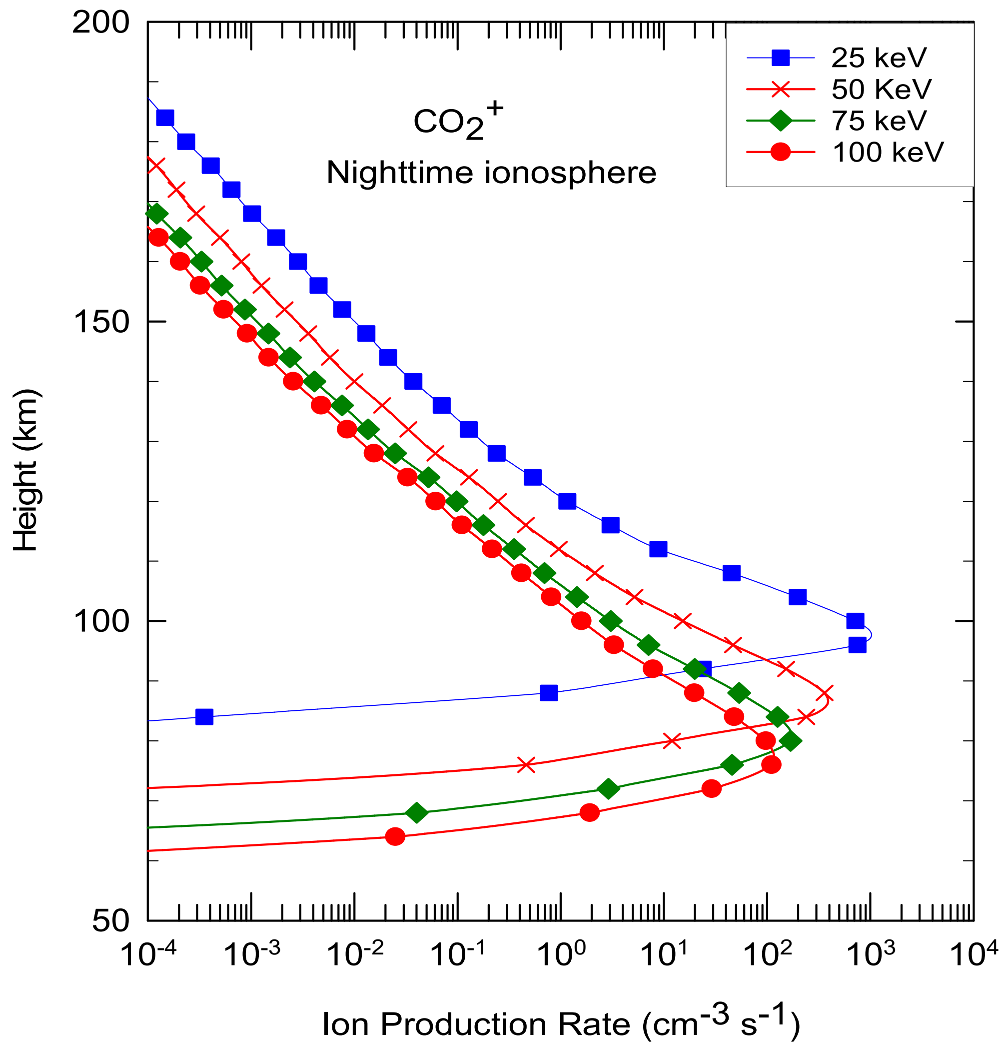


**Figure 6.4 The ion production rates of $CO_2^+$ due to precipitation of SEP electrons at energies 25 keV, 50 keV, 75 keV and 100 keV in the nighttime ionosphere of Mars.**

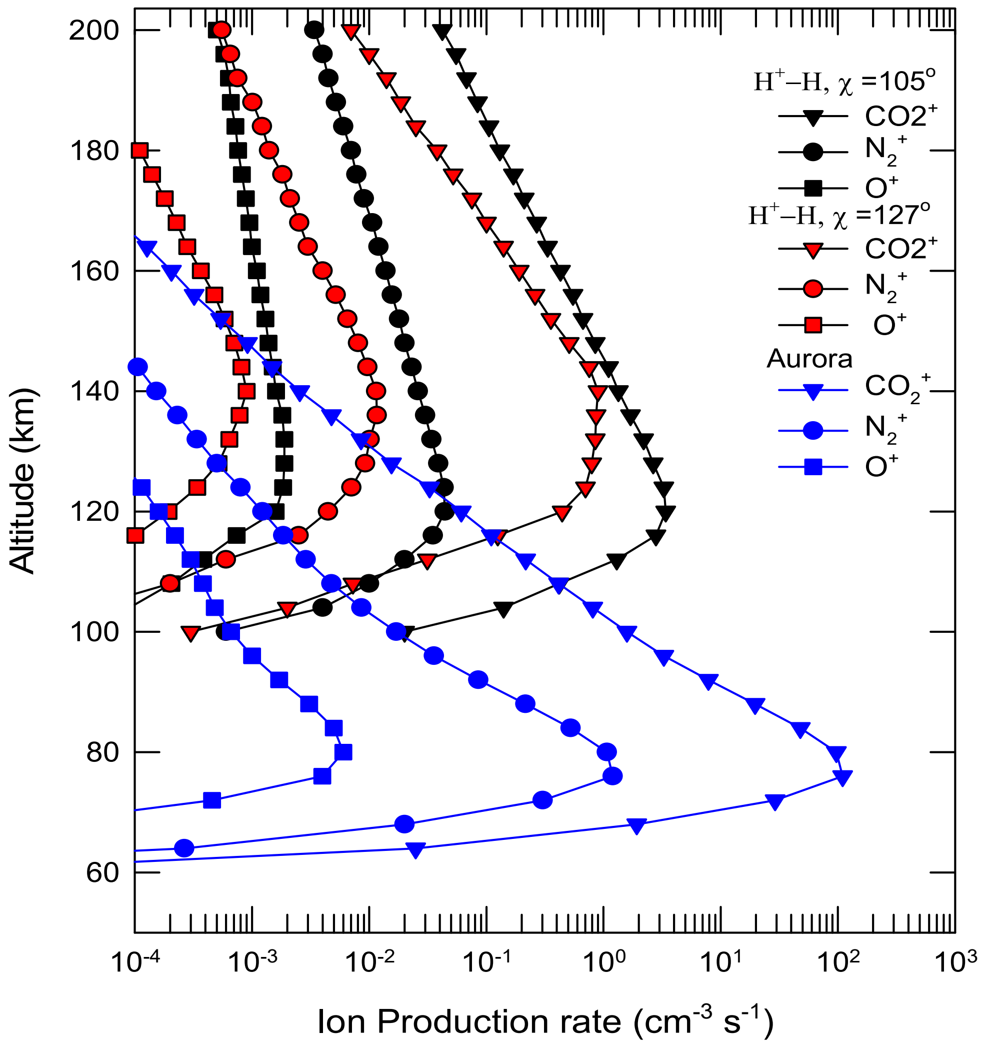


**Figure 6.5 The ion production rates of $CO_2^+$, $N_2^+$ and $O^+$ due to impact of SEP electrons of 100 keV and $H^+$-H impact at SZA=105° and 127° in the nighttime ionosphere of Mars.**

## 6.3.3 Auroral ionosphere

The figure 6.6 represents the comparison between observed and modelled vertical profiles of the limb intensities of $CO_2^+$ UVD in the nighttime ionosphere of Mars. The peak limb intensities are estimated to be ~ 6 x $10^3$ R, ~ 3 x $10^3$ R, ~ 1.2 x $10^3$ R and ~1 x $10^3$ R at about 95 km, 85 km, 80 km and 75 km due to precipitation of SEP electrons of energies 25 keV, 50 keV, 75 keV and 100 keV respectively. The estimated peak value and peak height of the limb intensity are highest due to electron impact of 25 keV because the electron flux of 25 keV is larger than the other energies. The observed limb intensity (Schneider et al., 2015) of $CO_2^+$ UVD represents a broad peak with 500 R, at altitude ~ 70 km. This is an observed vertical profile averaged over 5 days of continuous auroral emissions at the limb. There is a reasonable agreement between the peak altitudes of the measured and estimated limb intensities of 100 keV precipitating electrons. However, the peak intensity estimated for the impact of 100 keV electrons is larger by a factor of 2 than the measurement because the analytical fits of the yield spectra is producing high production rates by a factor of 2 at low altitudes (Haider and Singhal, 1983). As expected the peak limb intensities and peak altitudes of $CO_2^+$UVD band are increasing with the measurements by a factor of 2-10 at energies decreasing from 100 keV, 75 keV, 50 keV and 25 keV. Above 100 km, the observed limb intensity is reproduced by the sum of the $H^+$-H impact ionizations at SZA 105$^o$ and 127$^o$. The limb intensity due to impact of $H^+$-H at SZA 127$^o$ are smaller by a factor of 3-4 than that estimated at SZA 105$^o$.

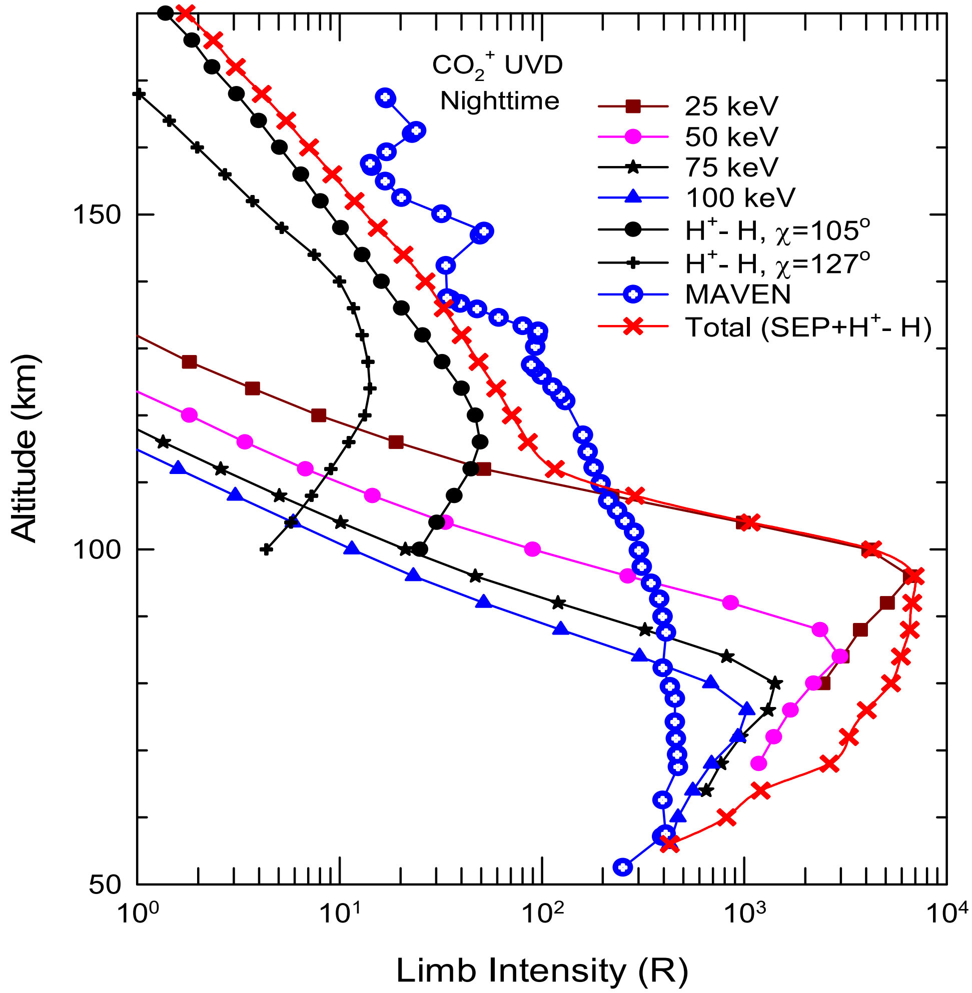


**Figure 6.6 The limb intensities of $CO_2^+$ UVD due to impact of $H^+$-H at SZA 105° and 127° and SEP electron impact at energies 25 keV, 50 keV, 75 keV and 100 keV in the nighttime ionosphere of Mars. The estimated results are compared with the observed profile of $CO_2^+$ UVD (Schneider et al., 2015) obtained from MAVEN when diffuse aurora occurred on Mars.**

The figure 6.7 represents the comparison between the ion and electron densities ($CO_2^+$, $O_2^+$, $NO^+$, and $N_e$) in the upper and middle ionosphere of Mars due to precipitation of $H^+$-H and SEP electrons respectively. We have calculated these ion and electron densities under steady state equilibrium conditions. The $H^+$-H impact ionizations do not provide a substantial source in the upper ionosphere as SEP electrons have produced in the middle ionosphere. The peak densities of $O_2^+$, $NO^+$ and

$CO_2^+$ are calculated to be 1 x $10^3$ $cm^{-3}$, 8 x $10^2$ $cm^{-3}$ and 1 x $10^1$ $cm^{-3}$ at altitudes 140 km, 135 km and 138 km respectively due to $H^+$-H impact ionizations at SZA 127°. At SZA 105°, the peak altitudes of these ions are lowered by 10-15 km and their peak densities were increased by a factor of ~ 2. The peak electron densities are estimated to be ~ 3.3 x $10^3$ and 1.2 x $10^3$ at SZA 105° and 127° respectively due to $H^+$-H impact ionizations. The precipitation of auroral electrons of 100 keV is considered for the production of $O_2^+$, $NO^+$ and $CO_2^+$ ions. The peak densities of $O_2^+$, $NO^+$ and $CO_2^+$ were estimated to be 3 x $10^4$ $cm^{-3}$, $10^3$ $cm^{-3}$ and 65 $cm^{-3}$ at altitudes 75 km, 90 km and 80 km respectively. It is quite evident that the both ionizing sources have produced major ion $CO_2^+$ which is quickly removed by atomic oxygen, leading to $O_2^+$ as the dominant ion. The major source of $NO^+$ is due to loss of $O_2^+$ with NO. We have used charge exchange, charge transfer and dissociative recombination reactions in the chemistry of the middle and upper ionosphere of Mars. Three body reactions are not important in both ionospheric regions (Haider et al., 2009). The diffuse aurora on Mars occurred on a global scale spanning at all longitudes. However, IUVS sampled a limited range on the nightside of Mars with a relatively fixed ground track from 35°N and ~ 00:30 local time to 70°N and 5:00 local time (Schneider et al., 2015, 2018). We have calculated auroral emission and ionosphere at one location of the spacecraft observations (35°N, 66°W). The neutral density of $CO_2$ is not changing significantly with longitudes between latitudes 35°N and 70°N (Millour et al., 2014). Therefore, our model results can be representative of a global diffuse aurora. The challenge for the future is to study diurnal and seasonal changes that may occur in the diffuse aurora over the entire Martian globe. By comparing model results with observations, we can constraint the model parameters to understand the physical processes.

In the diffuse aurora only a part of energy is utilized in the excitation and emissions processes. The SEP electrons ionize, dissociate and heat the atmospheric gases. Thus, detailed modeling of the excitation rates, ionization rates, limb intensities, ion and electron densities are required to understand the complete physio-chemical processes of diffuse aurora on Mars. The ionization rates, ion and electron densities are not measured in the diffuse auroral ionosphere. In absence of these measurements our estimated results serve as benchmark values that guide the design of future ionospheric payloads. Our theoretical prediction of auroral ionosphere awaits experimental validation.

Unlike Earth, diffuse auroras are different on Mars. In some sense, it is common with the auroras on Venus and moons of the Jovian planets. The Earth's diffuse aurora occurred due to accelerated electrons along the open field lines of the auroral oval. However, Mars' diffuse aurora occurred away from the strong closed crustal magnetic fields. The open or draped field lines allow SEP electrons to penetrate deep into the atmosphere of Mars and produce diffuse aurora during solar storms. The draped field lines mostly spread over the entire planet. The location of this field lines are changing due to rotation of the planet. Therefore, diffuse auroras on Mars can occur anywhere on the planet. Venus has neither magnetic field nor any crustal fields. The diffuse aurora is also observed on Venus from oxygen emission at 130 nm due to impact of low energy electrons (Fox, 1991). This emission is not detected on Mars from IUVS observations (Schneider et al., 2015).

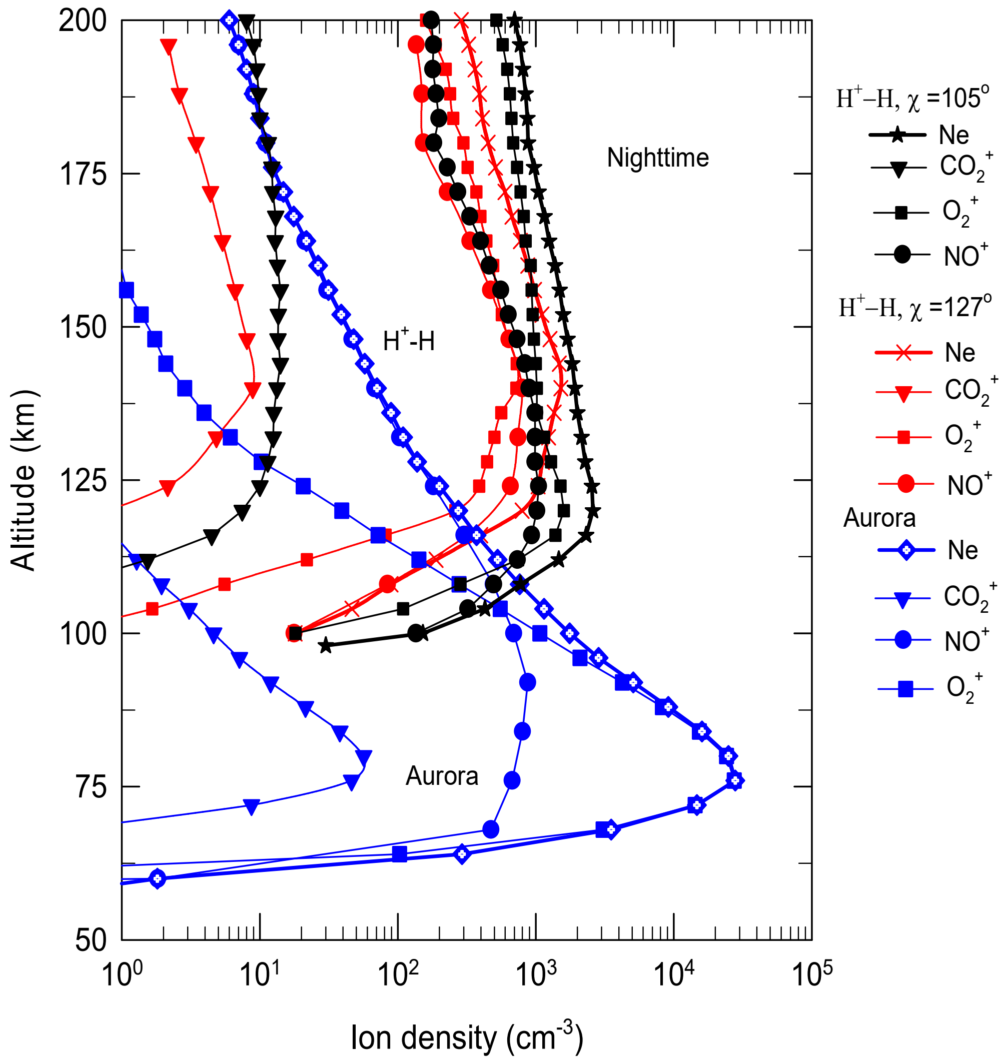


**Figure 6.7 The ion densities of $CO_2^+$, $O_2^+$ and $NO^+$ due to impact of SEP electrons of 100 keV and $H^+$-H impact at SZA 105° and 127° in the nighttime ionosphere of Mars. The electron density ($N_e$) due to impact of $H^+$-H and SEP electrons of 100 keV are also plotted in this figure.**

❐❐❐

# REFERENCES

Bertaux, J. L., Leblanc, F., Witasse, O., Quemerais, E., Lilensten, J., Stern, S. A., and orablev, O. (2005). Discovery of an aurora on Mars. Nature, **435**, 790-794.

Bhardwaj, A., Haider, S. A., and Singhal, R. P. (1995). Consequences of cometary aurora on the carbon chemistry at comet P/Halley. Advances in Space Research, **16**(2), 31-36.

Bhardwaj, A., and Jain, S. K. (2013). CO Cameron band and CO2+ UV doublet emission in the dayglow of Venus: Role of CO in the Cameron band production. Journal of Geophysical Research: Space Physics, **118**, 3660-3671.

Cane, H. V., Kahler, S. W., and Sheeley, N. R. (1986). Interplanetary shocks preceded by solar filament eruptions. Journal of Geophysical Research: Space Physics, **91**(A12), 13,321-13,329.

Deighan, J., Jain, S. K., Chaffin, M. S., Fang, X., Halekas, J. S., Clarke, J. et al. (2018). Discovery of proton aurora at Mars. Nature Astronomy, **2**(10), 802-807.

Fox, J. L. (1991). Cross sections and reaction rates of relevance to Aeronomy. Reviews of Geophysics, **29**, 1110-1131.

Fox, J. L., and Dalgarno, A. (1979). Ionization, luminosity, and heating of the upper atmosphere of Mars. Journal of Geophysical Research: Space Physics, **84**, 7315-7333.

Galli, A., Wurz, P., Barabash, S., Grigoriev, A., Gunell, H., Lundin, R. et al. (2006). Energetic hydrogen and oxygen atoms observed on the nightside of Mars. Space Science Reviews, **126**, 267-297.

Galli, A., Wurz, P., Kallio, E., Ekenback, A., Holmstrom, M., Barabash, S. et al. (2008). Tailward flow of energetic neutral atoms observed at Mars. Journal of Geophysical Research: Planets, 113, E12012.

Gérard, J. C., Soret, L., Shematovich, V. I., Bisikalo, D. V., and Bougher, S. W. (2017). The Mars diffuse aurora: A model of ultraviolet and visible emissions. Icarus, **288**, 284-294.

Haider, S. A., Abdu, M. A., Batista, I. S., Sobral, J. H., Kallio, E., Maguire, W. C., and Verigin, M. I. (2009). On the responses to solar X-ray flare and coronal mass ejection in the ionospheres of Mars and Earth. Geophysical Research Letters, **36**, L13104.

Haider, S. A., Mahajan, K. K., and Kallio, E. (2011). Mars ionosphere: A review of experimental results and modeling studies. Reviews of Geophysics, **49**, RG4001.

Haider, S. A., Pandya, B. M., and Molina-Cuberos, G. J. (2013). Nighttime ionosphere caused by meteoroid ablation and solar wind electron-proton-hydrogen impact on Mars: MEX observation and modeling. Journal of Geophysical Research: Space Physics, **118**, 6786-6794.

Haider, S. A., Seth, S. P., Kallio, E., and Oyama, K. I. (2002). Solar EUV and electron-proton-hydrogen atom-produced ionosphere on Mars: Comparative studies of particle fluxes and ion production rates due to different processes. Icarus, **159**(1), 18-30.

Haider, S. A., and Singhal, R. P. (1983). Analytical yield spectrum approach to electron energy degradation in Earth's atmosphere. Journal of Geophysical Research: Space Physics, **88**(A9), 7185-7189.

Haider, S. A., and Masoom, J. (2019). Modeling of diffuse aurora due to precipitation of $H^+$-H and SEP electrons in the nighttime atmosphere of Mars: Monte Carlo simulation and MAVEN observation. Journal of Geophysical Research: Space Physics, **124**, 9566-9576.

Jakosky, B. M., Grebowsky, J. M., Luhmann, J. G., Connerney, J., Eparvier, F., Ergun, R. et al. (2015). MAVEN observations of the response of Mars to an interplanetary coronal mass ejection. Science, **350**(6261), aad0210.

Kallio, E., Koskinen, H., Barabash, S., Lundin, R., Norberg, O., and Luhmann, J. G. (1994). Proton flow in the Martian magnetosheath. Journal of Geophysical Research: Space Physics, **99**, 23,547-23,559.

Kallio, E., and Barabash, S. (2001). Atmospheric effects of precipitating energetic hydrogen atoms on the Martian atmosphere. Journal of Geophysical Research: Space Physics, **106**(A1), 165-177.

Kallio, E., and Janhunen, P. (2001). Ion escape from Mars in a quasi-neutral hybrid model. Journal of Geophysical Research: Space Physics, **107**(A3).

Larson, D. E., Lillis, R. J., Lee, C. O., Dunn, P. A., Hatch, K., Robinson, M., et al. (2015). The MAVEN solar energetic particle investigation. Space Science Reviews, **195**(14), 153-172.

Leblanc, F., Luhmann, J. G., Johnson, R. E., and Chassefiere, E. (2002). Some expected impacts of a solar energetic particle event at Mars. Journal of Geophysical Research, **107**(A5), 1058.

Lee, C. O., Hara, T., Halekas, J. S., Thiemann, E., Chamberlin, P., Eparvier, F. et al. (2017). MAVEN observations of the solar cycle 24 space weather conditions at Mars. Journal of Geophysical Research: Space Physics, **122**, 2768-2794.

Mantas, G. P., and Hanson, W. B. (1979). Photoelectron fluxes in the Martian ionosphere. Journal of Geophysical Research: Space Physics, **84**(A2), 369-385.

McIlwain, C. E. (1960). Direct measurement of particles producing visible auroras. Journal of Geophysical Research, **65**(14), 2727-2747.

McKenna-Lawlor, S., Gonçalves, P., Keating, A., Reitz, G., and Matthiä, D. (2012). Overview of energetic particle hazards during prospective manned missions to Mars. Planetary and Space Science, **63**, 123-132.

Milillo, A., Mura, A., Orsini, S., Massetti, S., son Brandt, P. C., Sotirelis, T., et al. (2009). Statistical analysis of the observations of the MEX/ASPERA-3 NPI in the shadow. Planetary and Space Science, **57**(8-9), 1000-1007.

Millour, E., Forget, F., Spiga, A., Navarro, T., Madeleine, J. B., Pottier, A. and MCD/GCM Development Team (2014). A new Mars Climate Database v5.1. The Fifth International Workshop on the Mars Atmosphere: Modelling and Observations, Jan 2014, Oxford, United Kingdom (pp. 1301).

Mitchell, D. L., Lin, R. P., Rème, H., Crider, D. H., Cloutier, P. A., Connerney, J. E. P., Acuña, M. H., and Ness, N. F. (2000). Oxygen auger electrons observed in Mars ionosphere. Geophysical Research Letters, **27**, 1871-1874.

Morgan, D. D., Gurnett, D. A., Kirchner, D. L., Huff, R. L., Brain, D. A., Boynton, W. V., Acuna, M. H., Plaut, J. J., and Picardi, G. (2006). Solar control of radar wave absorption by the Martian ionosphere. Geophysical Research Letters, **33**, L13202.

Ramstad, R., Holmström, M., Futaana, Y., Lee, C. O., Rahmati, A., Dunn, P., Lillis, R. J., and Larson, D. (2018). The September 2017 SEP event in context with the current solar cycle: Mars Express ASPERA-3/IMA and MAVEN/SEP observations. Geophysical Research Letters, **45**, 7306-7311.

Ritter, B., Gerard, J.-C., Hubert, B., Rodrigues, L., and Montmessin, F. (2018). Observations of the proton aurora on Mars with SPICAM onboard Mars Express. Geophysical Research Letters, **45**, 612-619.

Rudd, M. E., Kim, Y. K., Madison, D. H., and Gallagher, J. W. (1985). Electron production in proton collisions: Total cross sections. Reviews of Modern Physics, **57**, 965-994.

Schneider, N. M., Deighan, J. I., Jain, S. K., Stiepen, A., Stewart, A. I. F., Larson, D., Mitchell, D. L., Mazelle, C., Lee, C. O., Lillis, R. J., and Evans, J. S. (2015). Discovery of diffuse aurora on Mars. Science, **350**, 6261.

Schneider, N. M., Jain, S. K., Deighan, J., Nasr, C. R., Brain, D. A., Larson, D et al. (2018). Global aurora on Mars during the September 2017 space weather event. Geophysical Research Letters, **45**, 7391-7398.

Sheel, V., Haider, S. A., Withers, P., Kozarev, K., Jun, I., Kang, S., Gronoff, G., and Simon Wedlund, C. (2012). Numerical simulation of the effects of a solar energetic particle event on the ionosphere of Mars. Journal of Geophysical Research: Space Physics, **117**, A05312.

Singhal, R., Jackman, C., and Green, A. E. S. (1980). Spatial aspects of low-and medium-energy electron degradation in $N_2$. Journal of Geophysical Research, **85**(A3), 1246-1254

❐❐❐

CHAPTER - 7

# EXECUTIVE SUMMARY

In chapter 1, we have described the thermal emission and current understanding of Martian atmosphere based on literature survey. The electromagnetic and particle radiations incoming from the Sun and their contributions to the lower atmosphere of Mars are also discussed. Finally, we have outlined the Chapterization of the present thesis.

In chapter 2, we have described the observations of the dust optical depth measured by TES and THEMIS for nine consecutive Martian years. The mathematical formulation for the calculation of dust density profiles of different sizes of aerosol particles are reported. The calculation of Planck function, radiative transfer method, ozone heating rates are also described. Finally, the modeling of auroral emissions using AYS and Hybrid method approach are discussed in detail.

In chapter 3, the thermal emission measurements of dust optical depth from TES and THEMIS from MY 24-32 are discussed. These datasets inferred two global dust storms at MY 25 and MY 28 which occurred at the southern latitudes. The density profiles from 0-70km at Ls = 240°, 280°, 300°, and 320° are calculated. We have considered $\tau = 0.1$ as the normal dust conditions, $\tau = 1.2$ as high conditions and $\tau = 0.5$ as medium conditions for the dust calculation. Our results suggest that lighter particles will be lifted easily as compared to the particles of larger radii. This is evident from the normal dust condition ($\tau = 0.1$). In this chapter, the MCS, CRISM, and PFS observations are also reported. Our study provides an important tool to understand the dust density of various particle sizes in the lower atmosphere of Mars.

In chapter 4, we have carried out analysis of PFS observations. We have discussed the tools and method used to analyse PFS datasets. We have calculated brightness temperature and thermal emission spectra at low latitude of Mars in presence and absence of dust storm. The maximum temperature ~ 280 K is observed at Ls = 240° when Mars received a large amount of solar radiation at perihelion. The minimum temperature ~ 220 K is observed in absence of dust storm at Ls = 320°. From the radiative transfer calculation, we have concluded that PFS thermal emission spectrum and brightness temperatures are reduced by factors of ~ 3 and ~ 1.3 respectively during the dust storm period due to absorption of dust between wave numbers 900-1200 $cm^{-1}$.

In chapter 5, we have studied the seasonal variability of ozone vertical profiles at low, mid and high latitudes from the Mars Climate Database. It is found that the dust opacity increased up to ~ 3.0 when a major dust storm occurred in southern hemisphere during MY28. In northern hemisphere the column ozone is found to be maximum in spring and minimum in summer at low latitudes. At mid-to high latitudes column ozone is found to be largest in northern winter and minimum in southern summer. Similarly, column ozone is largest in southern winter and close to zero in northern summer at mid-to high latitudes. The heating rates of ozone represent a broad peak between 30 km and 50 km at low to mid-latitudes due to photolysis of molecular oxygen which attach with atomic oxygen and form the ozone layer. This layer is fully destroyed by the photodissociation of ozone. The peak heights of ozone heating rates were reduced by about 10-20 km at southern mid-latitudes in comparison to northern mid-latitudes. We have not found these peaks very clear at high latitudes. It has been found that the dust significantly affects the density of ozone and ozone heating rates along with wind speeds in the atmosphere of Mars. The significant effects of dust storm on ozone heating rates are found up to 10 km in MY 28 at latitude 25° S and Ls ~ 280°.

In chapter 6, we have carried out modeling of diffuse aurora by calculating ion production rates of $CO_2^+$, $N_2^+$ and $O^+$, limb intensity of $CO_2^+$ UVD, densities of ions

$CO_2^+$, $O_2^+$ and $NO^+$ and electrons due to precipitation of $H^+$-H and SEP electrons in the nighttime atmosphere of Mars. The calculated limb intensities due to impact of $H^+$-H and SEP electrons are compared with the IUVS observations which were carried out during 17-21 December, 2014. In this model calculation we have used hybrid model and four dimensional AYS method based on Monte Carlo simulation. Our model calculation shows that SEP electrons of 100 keV is enough to produce the observed peak limb intensity at about 75 km where MAVEN observed nighttime auroral emissions. We have found that the densities of the upper ionosphere due to impact of $H^+$-H are smaller by 1-2 orders of magnitude than that produced by SEP electrons in the middle ionosphere. The total limb intensity of $CO_2^+$ UVD due to combined sources of $H^+$-H and SEP electron impact ionizations is also estimated and compared with the IUVS observations. In the upper ionosphere (100-200 km) the observed limb intensity is reproduced by the sum of the $H^+$-H impact ionizations at SZA 105° and 127°. Due to this process the total limb intensity at SZA 105° and 127° peaked at about 120 km with a value of ~ 100 R. The observed limb intensity is produced by SEP electrons of energy 100 keV in the middle ionosphere (50-100 km). Due to this process the peak limb intensity occurred at ~75 km with a value of 1000 R which is higher than the observations by a factor of 2.

❒❒❒

# CHAPTER - 8

# FUTURE WORK

In the present thesis, we have carried out the modeling and observations of dust opacities, dust density profiles, thermal emissions, ozone heating rates and intensity of diffuse aurora in the lower atmosphere of Mars. In future, we plan to investigate the physical processes of the dust storm formation in MY 34.

The dust density profiles of different size will be estimated by using our model. The ion and electron density profiles will also be calculated in presence and absence of this dust storm. In the continuity and momentum model, the dust collision with the atmosphere is a loss process. Therefore, we expect that the lower ionosphere can be significantly reduced in the presence of dust storm. This suggests that the lower ionosphere can be disappeared for few weeks when the dust storm occurred in MY 34. There are no observations in the lower ionosphere of Mars. Due to lack of the measurements, our estimated results will be very use useful for the development of ionospheric payloads which can be flown to Mars in future.

Recently MAVEN has observed ion and electron densities in the upper ionosphere of Mars. In MY 34, the dust is reaching into the upper atmosphere. Therefore, the effects of this dust storm can also be found on ion and electron density distributions. This will be a unique study in the future to study the effects of dust storm in the upper ionosphere of Mars. The dust also heats the atmosphere of Mars. Thus the neutral density observed by the NGIMS can be increased during the dust storm event due to heating and dynamical process.

❑❑❑

# PUBLICATIONS

# Response of dust on thermal emission spectra observed by Planetary Fourier Spectrometer (PFS) on-board Mars Express (MEX)

**J. Masoom[1,2], S. A. Haider[1], Marco Giuranna[3]**

[1]Planetary Sciences Division, Physical research Laboratory, Ahmedabad, India

[2]Research Scholar, Faculty of Science, Pacific Academy of Higher Education of Research University, Udaipur, India

[3]Istituto di Astrofisica e Planetologia (IAPS), Istituto Nazionale di Astrofisica (INAF), Roma, Italy

## ABSTRACT

The thermal emission spectra have provided many useful insights about the Martian atmosphere and surface. The interpretation of the thermal emission spectra can give us information about atmospheric temperature, pressure, mineralogy and presence of atmospheric constituents including their isotopes. In the present work, we have analyzed the thermal emission data for dust storm season on Mars. The signature of dust in the thermal emission spectra for Martian Year (MY) 28 confirms presence (Ls=280° and 300°) and absence (Ls=240° and 320°) of the dust storm at latitude range 0°-10°S, 10°-20°S and 20°-30°S. We have compared our results with earlier mission data with thermal emission measurements made by Planetary Fourier Spectrometer (PFS) on-board Mars Express (MEX) between wave numbers 250-1400 cm$^{-1}$. We have observed features at wave numbers 600-750 cm$^{-1}$ and 900-1200 cm$^{-1}$ due to absorptions by $CO_2$ and dust respectively. We have obtained brightness temperatures from thermal emission spectra by inverting the Planck function. The maximum brightness temperature ~280 K is measured at Ls=240° when Mars received a large amount of solar radiation at perihelion. The minimum brightness temperature ~ 220 K is observed at Ls=320° in the absence of dust storm. In presence of dust storm thermal emission spectra and brightness temperatures are reduced by factors of ~ 3.0 and ~1.3 respectively between wave numbers 900-1200 cm$^{-1}$ in comparison to that observed in absence of dust storm.

**Accepted article:** Indian Journal of Radio & Space Physics, (2019).
ISSN: 0975-105X

# Modeling of Diffuse Aurora due to Precipitation of $H^+$-H and SEP Electrons in the Nighttime Atmosphere of Mars: Monte Carlo Simulation and MAVEN Observation

**S. A. Haider[1], J. Masoom[1,2]**

[1]Planetary Science Division, Physical Research Laboratory, Ahmedabad, India

[2]Research Scholar, Faculty of Science, Pacific Academy of Higher Education and Research University, Udaipur, India

## ABSTRACT

The nighttime limb intensity of diffuse auroral emission of $CO_2^+(B^2\Sigma_u^+ - X^2\pi_g)$ Ultraviolet Doublet (UVD) is observed in the northern hemisphere of Mars during 17-21 December 2014 from Imaging Ultraviolet Spectrograph instrument onboard Mars Atmosphere and Volatile Evolution. We have used hybrid model and four-dimensional yield spectrum approach based on Monte Carlo simulation to calculate the ionization rate, limb intensity, and ion and electron densities of diffuse aurora due to precipitation of solar energetic particle and proton-hydrogen ($H^+$-H) fluxes in the nighttime ionosphere of Mars. It is found that the production rates of atmospheric ions ($CO_2^+$, $N_2^+$, and $O^+$) are dominant in the upper ionosphere at about 100-150 km due to impact of H+-H. The solar energetic particle formed auroral ionosphere ($CO_2^+$, $NO^+$, and $O^+$) in the middle ionosphere between 50 and 100 km due to precipitation of monoenergetic electrons of energies 25 to 100 keV. The simulated limb intensities of $CO_2^+$UVD due to impact of $H^+$-H and auroral electrons are compared with Imaging Ultraviolet Spectrograph observations. Our model results are overestimating the observations, but 100 keV electrons deposited maximum energy around 75 km, closer to the observed altitude of the maximum emission. The densities of upper ionosphere ($O_2^+$, $NO^+$, and $CO_2^+$) due to impact of H+-H are smaller by one to two orders of magnitude than that produced by auroral electrons in the middle ionosphere.

**Published in:** Journal of Geophysical Research: Space Physics, 124, 9566-9576, (2019).

ISSN: 2169-9402

## Presentations in Conference/Symposium

### 1 Study of dust storm by modeling and analysis of thermal emission spectra of Mars

Masoom Jethwa, and S. A. Haider

**Date**: 9-12 February, 2016

**Organizer**: 19th National Space Science Symposium held at Space Physics Laboratory, Vikram Sarabhai Space Center, Thiruvananthapuram.

### 2 Radiative transfer modeling of Mars during Martian Year 28

Masoom Jethwa, and S. A. Haider

**Date**: 8-10 November, 2017

**Organizer**: Brain Storming Session on Vision and Explorations for Planetary Sciences in Decades 2020-2060, Physical Research Laboratory, Ahmedabad.

### 3 Theoretical modeling of the auroral activity at Mars

Masoom Jethwa, and S. A. Haider

**Date**: 29-31 January, 2019

**Organizer**: 20th National Space Science Symposium to be held at Savitribai Phule Pune University, Pune.

## List of Publications

Haider, S. A., Pabari, J. P., **Masoom, J**., and Shah, S. Y. (2019). Schumann resonance frequency and conductivity in the nighttime ionosphere of Mars: A source for lightning. Advances in Space Research, 63(7), 2260-2266.

Haider, S. A., Siddhi, Y. S., **Masoom, J**., and Bougher, S. (2019). Effect of Dust Storm and GCR Impact on the Production Rate of $O_3^+$ in MY 28 and MY 29: Modeling and SPICAM Observation. Journal of Geophysical Research: Space Physics, 124(3), 2271-2282.

Haider, S. A., Siddhi Y. S, **Masoom, J.**, Sheel, V., and Kuroda, T. (2020). Dust loading on ozone, winds and heating rates in the tropics of southern atmosphere of Mars: Seasonal variability, climatology and SPICAM observations. Journal of Geophysical Research: Space Physics (Under review).